Thesis advisor   Author

Alán Aspuru-Guzik   **Sangwoo Shim**

Quantum Dynamics in Biological Systems

Abstract

In the first part of this dissertation, recent efforts to understand quantum mechanical effects in biological systems are discussed. Especially, long-lived quantum coherences observed during the electronic energy transfer process in the Fenna-Matthews-Olson complex at physiological condition are studied extensively using theories of open quantum systems. In addition to the usual master equation based approaches, the effect of the protein structure is investigated in atomistic detail through the combined application of quantum chemistry and molecular dynamics simulations. To evaluate the thermalized reduced density matrix, a path-integral Monte Carlo method with a novel importance sampling approach is developed for excitons coupled to an arbitrary phonon bath at a finite temperature. In the second part of the thesis, simulations of molecular systems and applications to vibrational spectra are discussed. First, the quantum dynamics of a molecule is simulated by combining semiclassical initial value representation and density funcitonal theory with analytic derivatives. A computationally-tractable approximation to the sum-of-states formalism of Raman spectra is subsequently discussed.

Contents

Citations to Previously Published Work

Chapters 2, 3, 5 and 6 have, apart from minor changes, appeared as the following publications:

"Characterization and quantification of the role of coherence in ultrafast quantum biological experiments using quantum master equations, atomistic simulations, and quantum process tomography," Patrick Rebentrost*, Sangwoo Shim*, Joel Yuen-Zhou* and Alán Aspuru-Guzik, *Procedia Chem.* **3**, 332 (2010).
* : Equal contributions.

"Atomistic study of the long-lived quantum coherences in the Fenna-Matthews-Olson complex," Sangwoo Shim, Patrick Rebentrost, Stéphanie Valleau and Alán Aspuru-Guzik, *Biophys. J.* **102**, 649 (2012).

"First-principles semiclassical initial value representation molecular dynamics," Michele Ceotto, Sule Atahan, Sangwoo Shim, Gian Franco Tantardini and Alán Aspuru-Guzik, *Phys. Chem. Chem. Phys.* **11**, 3861 (2009).

"Simplified Sum-Over-States Approach for Predicting Resonance Raman Spectra. Application to Nucleic Acid Bases," Dmitrij Rappoport, Sangwoo Shim and Alán Aspuru-Guzik, *J. Phys. Chem. Lett.* **2**, 1254 (2011).

Acknowledgments

Working with my advisor Professor Alán Aspuru-Guzik during the last five years has been the most inspiring experience of my life, not only academically but personally as well. I owe my deepest gratitude to Alán for guiding me through the exciting, sometimes intimidating world of scientific research. His enthusiasm, intuition, and scientific diligence are something remarkable and if, by writing this thesis, I have made even a small contribution to science, it was only because I have tried to follow in his footsteps as a scientist. I thank Professors Heller and Shakhnovich for giving invaluable advice during my graduate years and also for serving on the committee for this dissertation. I am especially grateful to Professor Kaxiras for willingly consenting to serve as a replacement thesis committee member.

I was lucky enough to have met and worked with many talented scientists in Alán's group and as collaborators. Discussions with them and listening to their insights have contributed to my academic growth to an extent comparable to Alán's guidance. They have included Joel Yuen-Zhou, Roberto Olivares-Amaya, Dmitrij Rappoport, Patrick Rebentrost, Stéphanie Valleau, Alejandro Perdomo-Ortiz, James Whitfield, Ivan Kassal, Leslie Vogt, David Tempel, Kenta Hongo, Mark Watson, Semion Saikin, John Parkhill, Sule Atahan-Evrenk, Jenny Brookes, Man-Hong Yung, Sarah Mostame, Xavier Andrade, Alex Eisfeld, Johannes Hachmann, Jacob Krich, Takatoshi Fujita, Joonsuk Huh, Jarrod McClean, Jacob Sanders, Ryan Babbush, and Michele Ceotto. I want to convey my sincere thanks to all of them.

I thank my Master's advisor, Professor Chaok Seok at Seoul National University, for introducing me to Monte Carlo and molecular dynamics simulations. These techniques have been my specialty ever since. I thank Professor Sangyoub Lee at Seoul

National University for his advice and inspiration. He also taught me many subjects including my first quantum mechanics, which were incredibly helpful in building a strong foundation to pursue academic research.

I also thank my friends Changho Sohn, Jinwoo Chang, Hong Geun Lee, Changhyun Ko, Dann Huh, Joungkeun Lim, Youjin Lee, Sungwoo Park, Junyoep Park, Junyeop Lee, Jaehyuk Choi, Jinyoung Baek, Ji Oon Lee, Eun Gook Moon, Eunmi Chae, Sungkun Hong, Yejin Huh, Joonhyun Lee, Jae Hoon Lee, Sae Kyu Lee, Lia Min, Junwon Choi, Ji-hyun Seo, Sanghyup Kwak, Soyean Kim, SeungYeon Kang, Jung Ook Hong, Kisun Yoon, Won-Yong Shin, Hyunsung Park, Yun-Ah Jang, Jaeyoung Park, Young Il Cho, Jaehong Jung, Siyeon Song, Dong-In Lee, Hyeongryul Park, Dongwan Ha, Hyewon Yoon, Dainn Wie, Tae Wook Kim, Eun-Suk Lee, Kyung Ryul Park, Yoonha Kim, Jang Ik Cho, Nari Yoon, Hee-Sun Han, Semi Park, Yoonjin Lee, Joonhyuk Choi, Sangmin Lim, Dongeun Lee, Min Ju Sohn, Doory Kim, Jaeyoung Ahn, So Youn Shim, Yongho Park, Wooyoung Hong, and Jeong-Mo Choi for everything. This is only a small sample of the people who have helped and inspired me, and I owe a beer to whomever I have omitted from the list.

I thank my mom, Sooja Son and my dad, Yeongho Shim for their continued support and for wholeheartedly being my fans from the day I was born. I would also like to thank to my sister, Nary Shim, for being such a great sister to me. I especially thank my father-in-law, Jeil Song, and brother-in-law, Jisoo Song, for their love and advice. Last, but not least, I thank my beautiful wife, Jisun, and our soon-to-be-born daughter for always standing beside me.

To my family and friends

Chapter 1

Introduction

Although more than 80 years passed of Paul Dirac's announcement that "the underlying physical laws necessary for the mathematical theory of a large part of physics and the whole of chemistry are completely known" [1], tremendous amount of efforts are still being made to achieve computationally-scalable simulations for quantum dynamics and their associated chemical phenomena. The cost of solving the time-dependent Schrödinger equation increases very quickly as the size of the system grows and as the total length of the propagation time gets longer. Even for a modest sized system, exact quantum mechanical dynamics easily becomes untractable with currently available computational resources. Therefore, most of the useful approaches for treating biological systems inevitably involve approximations to some extent. For example, the structure and behavior of protein complexes found in biology are explained well in terms of classical statistical mechanics and molecular dynamics, which are approximations of quantum statistical mechanics and time evolution [2–6]. For a larger system, even classical mechanical calculations are very hard to carry out.

Therefore, many coarse-grained and multiscale simulation methods have been suggested and are still actively being developed [7–9]. Nevertheless, classical mechanics has been the method of choice for studying biological systems in molecular level.

The Fenna-Matthews-Olson complex is a trimeric bacteriochlorophyll protein in the light-harvesting system of green surfur bacteria [10, 11]. This complex transfers the energy of the photons collected at the photosynthetic antenna complex to the reaction center [12]. Eight bacteriochlorophyll (BChl) molecules each of which acting as a chromophore are embedded in its monomer. Because its high-resolution X-ray structure has been known for a long time, this subsystem has been studied extensively by theoreticians [13, 14] as well as experimentalists [15–18]. Early efforts were mostly focused on evaluating the Hamiltonian relevant to the spectroscopic measurement. BChl molecules were modelled as two-level systems interacting each other through electronic Förster's dipole-dipole coupling [19]. Each BChl molecule was also assumed to coupled to a harmonic oscillator bath to give the line broadening of the spectroscopic spectra. Within this assumption, the electronic Hamiltonian operator was evaluated by fitting to linear absorption spectra [13, 20], interpreting 2D electronic spectroscopy data [21], calculation based on force fields [14] and density functinal theory [22].

Recent 2D nonlinear spectroscopy experiments suggested the existence of long-lived quantum coherences lasting up to several hundreds of femtoseconds during the electronic energy transfer process in certain photosynthetic subsystems, especially within a Fenna-Matthews-Olson (FMO) complex of surfur bacterium, even under physiological conditions [23–25]. Moreover, the observed quantum coherences are

thought to contribute the energy transfer efficiency [26, 27]. Apparently, this energy transfer dynamics cannot be explained without quantum mechanics. Moreover, traditional master equation with Born-Markov approximation proven to be unable to reproduce this long-lived coherence [28]. Thus, more advanced theories of open quantum systems have been applied to explain the dynamics of excitons in FMO complex with some degree of success [29–33], and still being actively developed.

In the Part I of this dissertation, the efforts we made to understand those long lived quantum coherences in biological systems are presented; Chapter 2 presents a review on three approaches made in our group to characterize quantum effects in the FMO complex. Chapter 3 is about the atomistic simulation to include the effects from the realistic environment to the dynamics of excitons. Equilibrium properties of the reduced density matrix of excitons coupled to an arbitrary bath are explored in Chapter 4 using the path integral Monte Carlo method with importance sampling. Part II features two projects on calculations absorption and resonance Raman spectra based on approximate quantum dynamics of the molecular system, respectively. Chapter 5 introduces an approximate but very accurate real space wavefunction propagation in real time using time-averaged semiclassical initial value representation implemented on top of the *ab initio* molecular dynamics. A simplified and computationally tractable formulation of the resonance Raman scattering cross section using time dependent density functional theory and analytic derivatives is presented in chapter 6.

1.1   Review of Theoretical Approaches

For better understanding of the materials included this dissertation, introductions to basic concepts and relevant theories will be provided in the rest of the current chapter.

1.1.1   Basics of Open Quantum Systems

The density matrix of a closed system evolves according to the quantum Liouville equation. As elaborated in the previous section, explicit evaluation of a quantum mechanical time evolution becomes easily untractable, especially when there exist a large number of degrees of freedom. Fortunately, we are concerned with only a part of the total system in most cases. Consider an electronic energy transfer process in a biomolecular system; the entire system encompassing all electronic and vibrational degrees of freedom of the molecules and solvents should be, in principle, explicitly propagated to obtain the exact dynamics. But we are interested only in the electronic state of chromophores, which exists in a Hilbert space with only a few degrees of freedom. Therefore, if an equation of motion for such a part of the total system can be derived, all the information we need to obtain the solution for the problem can be identified. Theories for treating such a reduced quantum system interacting with a macroscopic environment is referred to theories of open quantum systems. The part of our interest is called *the system*, whereas the rest of the total system is referred as *the bath*. The partitioning is entirely determined by the decision of the physicist, although there may be an obvious choice for the system and the bath in many cases. Given a total density matrix, the system and the bath density matrices can be defined in a

very similar way to a marginal probability density in the probability theory. Given a probability density function of two random variables X and Y is given as $P_{X,Y}(x,y)$, the marginal density for X is given as,

$$P_X(x) = \int dy \ P_{X,Y}(x,y), \tag{1.1}$$

which is an effective probability density only for X. This density contains every information we need if we are only interested in the distribution of X even though the actual random process produces a random vector (X,Y). Now a reduced density matrix of the system can be defined as an effective, averaged density matrix over its bath by tracing out the bath degrees of freedom,

$$\rho_S(t) \equiv \text{Tr}_B \rho(t), \tag{1.2}$$

where $\rho(t)$ is the density matrix of the total system and Tr_B is the partial trace operator which traces out the bath degrees of freedom. In the following sections, two types of equations of motion for the reduced density matrix of the system will be introduced based on different sets of approximations.

1.1.2 Redfield Equation

We will discuss the general formulation of the Redfield equation first and then focus on the application on the electronic energy transfer dynamics. The Hamiltonian for the total system can be decomposed as three components:

$$\hat{H}_{total} = \hat{H}_S + \hat{H}_B + \hat{H}_{SB}, \tag{1.3}$$

where the system Hamiltonian $\hat{H}_S$ only acts on the Hilbert space of the system and the bath Hamiltonian $\hat{H}_B$ only act on the Hilbert space of the bath. Rest of the total

Hamiltonian causing the entanglement between the system and the bath is specified as the system-bath Hamiltonian $\hat{H}_{SB}$. By choosing the interaction picture relative to $\hat{H}_S + \hat{H}_B$ as the zeroth order Hamiltonian, the quantum mechanical equation of the motion for the total density matrix can be obtained:

$$\frac{d\tilde{\rho}(t)}{dt} = \frac{1}{i\hbar}\left[\tilde{H}_{SB}(t), \tilde{\rho}(t)\right],\tag{1.4}$$

where

$$\hat{U}_0(0,t) = e^{-\frac{i}{\hbar}\int_0^t \hat{H}_S(s)+\hat{H}_B(s)\ ds},$$

$$\tilde{\rho}(t) = \hat{U}_0^\dagger(0,t)\rho(t)\hat{U}_0(0,t),$$

$$\tilde{H}_{SB}(t) = \hat{U}_0^\dagger(0,t)\hat{H}_{SB}(t)\hat{U}_0(0,t).\tag{1.5}$$

Operators with a tilde are in the interaction picture. Closed form for $\bar{\rho}(t)$ can be obtained by integrating Eq. 1.4:

$$\tilde{\rho}(t) = \tilde{\rho}(0) + \frac{1}{i\hbar}\int_0^t ds\ \left[\tilde{H}_{SB}(s), \tilde{\rho}(s)\right].\tag{1.6}$$

Tracing over the bath degrees of freedom and plugging in Eq. 1.4 gives

$$\begin{aligned}\frac{d\tilde{\rho}_S(t)}{dt} &= \frac{1}{i\hbar}\mathrm{Tr}_B\left[\tilde{H}_{SB}(t), \tilde{\rho}(t)\right]\\ &= \frac{1}{i\hbar}\mathrm{Tr}_B\left[\tilde{H}_{SB}(t), \tilde{\rho}(0)\right] - \frac{1}{\hbar^2}\int_0^t ds\ \mathrm{Tr}_B\left[\tilde{H}_{SB}(t), \left[\tilde{H}_{SB}(s), \tilde{\rho}(s)\right]\right].\end{aligned}\tag{1.7}$$

Without the loss of generality, $\tilde{H}_{SB}(t)$ can be expanded as a linear combination of factorized operators:

$$\tilde{H}_{SB}(t) = \sum_k \tilde{A}_k(t) \otimes \tilde{B}_k(t) = \sum_k \tilde{A}_k^\dagger(t) \otimes \tilde{B}_k^\dagger(t).\tag{1.8}$$

Note that individual $\tilde{A}_k^\dagger(t)$ and $\tilde{B}_k^\dagger(t)$ might not be Hermitian even though $\tilde{H}_{SB}(t)$ is Hermitian. A series of assumptions needs to be introduced to proceed further. The

first assumption is called the Born approximation, which states that the total density matrix is factorizable at all times, and the bath state is in thermal equilibrium so it does not depend on time:

$$\tilde{\rho}(t) \approx \tilde{\rho}_S(t) \otimes \tilde{\rho}_B, \tag{1.9}$$

$$\tilde{\rho}_B = \rho_B = \frac{\exp(-\beta \hat{H}_B)}{\text{Tr}_B \exp(-\beta \hat{H}_B)}. \tag{1.10}$$

By plugging in Eq. 1.8 and Eq. 1.9 to Eq. 1.7,

$$
\begin{aligned}
\frac{d\tilde{\rho}_S(t)}{dt} &= \frac{1}{i\hbar} \sum_k \left\langle \tilde{B}_k(t) \right\rangle \left[\tilde{A}_k(t), \tilde{\rho}_S(0) \right] \\
&\quad - \frac{1}{\hbar^2} \sum_{k,l} \int_0^t ds \, \left\langle \tilde{B}_k^\dagger(t) \tilde{B}_l(s) \right\rangle \tilde{A}_k^\dagger(t) \tilde{A}_l(s) \tilde{\rho}_S(s) \\
&\quad + \frac{1}{\hbar^2} \sum_{k,l} \int_0^t ds \, \left\langle \tilde{B}_l(s) \tilde{B}_k^\dagger(t) \right\rangle \tilde{A}_k^\dagger(t) \tilde{\rho}_S(s) \tilde{A}_l(s) \\
&\quad + \frac{1}{\hbar^2} \sum_{k,l} \int_0^t ds \, \left\langle \tilde{B}_k^\dagger(t) \tilde{B}_l(s) \right\rangle \tilde{A}_l(s) \tilde{\rho}_S(s) \tilde{A}_k^\dagger(t) \\
&\quad - \frac{1}{\hbar^2} \sum_{k,l} \int_0^t ds \, + \left\langle \tilde{B}_l(s) \tilde{B}_k^\dagger(t) \right\rangle \tilde{\rho}_S(s) \tilde{A}_l(s) \tilde{A}_k^\dagger(t) \\
&= \frac{1}{i\hbar} \sum_k \left\langle \tilde{B}_k(t) \right\rangle \left[\tilde{A}_k(t), \tilde{\rho}_S(0) \right] \\
&\quad - \frac{1}{2\hbar^2} \sum_{k,l} \int_0^t ds \, \left\langle \left\{ \tilde{B}_k^\dagger(t), \tilde{B}_l(s) \right\} \right\rangle \left(\left[\tilde{A}_k^\dagger(t), \left[\tilde{A}_l(s), \tilde{\rho}_S(s) \right] \right] \right) \\
&\quad - \frac{1}{2\hbar^2} \sum_{k,l} \int_0^t ds \, \left\langle \left[\tilde{B}_k^\dagger(t), \tilde{B}_l(s) \right] \right\rangle \left(\left[\tilde{A}_k^\dagger(t), \left\{ \tilde{A}_l(s), \tilde{\rho}_S(s) \right\} \right] \right), \tag{1.11}
\end{aligned}
$$

where $\left\langle \tilde{O} \right\rangle = \text{Tr}_B \left[\tilde{O} \tilde{\rho}_B \right]$. Because the bath is assumed to be in thermal equilibrium, the bath correlation function is stationary and only depends on the difference of the two times:

$$c_{kl}(s) = \frac{1}{\hbar} \left\langle \tilde{B}_k^\dagger(s) \tilde{B}_l(0) \right\rangle = \frac{1}{\hbar} \left\langle \tilde{B}_k^\dagger(t) \tilde{B}_l(t-s) \right\rangle. \tag{1.12}$$

It is convenient to define the symmetrized correlation function $S_{kl}(t)$ and the response function $\chi_{kl}(t)$:

$$S_{kl}(t) = \frac{1}{\hbar} \left\langle \left\{ \tilde{B}_k^\dagger(t), \tilde{B}_l(0) \right\} \right\rangle = c_{kl}(t) + c_{kl}^*(t), \tag{1.13}$$

$$\chi_{kl}(t) = \frac{i}{\hbar} \left\langle \left[\tilde{B}_k^\dagger(t), \tilde{B}_l(0) \right] \right\rangle = i \left\{ c_{kl}(t) - c_{kl}^*(t) \right\}. \tag{1.14}$$

$S_{kl}(t)$ and $\chi_{kl}(t)$ are often referred to as the noise and dissipation kernels, respectively [34]. The Eq. 1.11 can be rewritten in terms of these two real functions:

$$\begin{aligned}
\frac{d\tilde{\rho}_S(t)}{dt} &= \frac{1}{i\hbar} \sum_k \left\langle \tilde{B}_k(t) \right\rangle \left[\tilde{A}_k(t), \tilde{\rho}_S(0) \right] \\
&\quad - \frac{1}{\hbar} \sum_{k,l} \int_0^t ds\, \frac{1}{2} S_{kl}(t-s) \left[\tilde{A}_k(t), \left[\tilde{A}_l(s), \tilde{\rho}_S(s) \right] \right] \\
&\quad + \frac{1}{\hbar} \sum_{k,l} \int_0^t ds\, \frac{i}{2} \chi_{kl}(t-s) \left[\tilde{A}_k(t), \left\{ \tilde{A}_l(s), \tilde{\rho}_S(s) \right\} \right].
\end{aligned} \tag{1.15}$$

By changing the integration variable to $t - s$,

$$\begin{aligned}
\frac{d\tilde{\rho}_S(t)}{dt} &= \frac{1}{i\hbar} \sum_k \left\langle \tilde{B}_k(t) \right\rangle \left[\tilde{A}_k(t), \tilde{\rho}_S(0) \right] \\
&\quad - \frac{1}{\hbar} \sum_{k,l} \int_0^t ds\, \frac{1}{2} S_{kl}(s) \left[\tilde{A}_k(t), \left[\tilde{A}_l(t-s), \tilde{\rho}_S(t-s) \right] \right] \\
&\quad + \frac{1}{\hbar} \sum_{k,l} \int_0^t ds\, \frac{i}{2} \chi_{kl}(s) \left[\tilde{A}_k(t), \left\{ \tilde{A}_l(t-s), \tilde{\rho}_S(t-s) \right\} \right].
\end{aligned} \tag{1.16}$$

Now we introduce the second assumption which states that the bath is stationary and its correlation function decays rapidly:

$$c_{kl}(s) \approx 0 \qquad \text{for} \quad s > \tau_c. \tag{1.17}$$

This assumption will let us integrate up to infinite time in the second term of Eq. 1.16. Moreover, if $\bar{\rho}_S(t)$ does not change much during the characteristic time τ_c, $\bar{\rho}_S(t-s)$

in the integrand can be approximated as $\bar{\rho}_S(t)$ and a Markovian equation of motion

is obtained:

$$
\begin{aligned}
\frac{d\tilde{\rho}_S(t)}{dt} \approx & \frac{1}{i\hbar} \sum_k \left\langle \tilde{B}_k(t) \right\rangle \left[\tilde{A}_k(t), \tilde{\rho}_S(0) \right] \\
& - \frac{1}{\hbar} \sum_{k,l} \int_0^\infty ds \, \frac{1}{2} S_{kl}(s) \left[\tilde{A}_k(t), \left[\tilde{A}_l(t-s), \tilde{\rho}_S(t) \right] \right] \\
& + \frac{1}{\hbar} \sum_{k,l} \int_0^\infty ds \, \frac{i}{2} \chi_{kl}(s) \left[\tilde{A}_k(t), \left\{ \tilde{A}_l(t-s), \tilde{\rho}_S(t) \right\} \right].
\end{aligned} \tag{1.18}
$$

Eq. 1.18 is referred as the Redfield equation. When a model of the bath correlation

function is given, this equation can be integrated to give a complete Markovian master

equation.

The electronic and phonon Hamiltonians of a typical Frenkel exciton can be spec-

ified as [29]:

$$
\hat{H}_{el} = \sum_n \varepsilon_n |n\rangle\langle n| + \sum_{m \neq n} E_{mn} |m\rangle\langle n|, \tag{1.19}
$$

$$
\hat{H}_{ph} = \sum_i \frac{\hat{p}_i^2}{2m_i} + \frac{1}{2} m_i \omega_i^2 \hat{q}_i^2 = \sum_i \hbar\omega_i \left(\hat{a}_i^\dagger \hat{a}_i + \frac{1}{2} \right), \tag{1.20}
$$

where the lowering and raising operators of the ith mode are

$$
\hat{a}_i = \sqrt{\frac{m_i\omega_i}{2\hbar}} \left(\hat{q}_i + \frac{i}{m_i\omega_i} \hat{p}_i \right), \tag{1.21}
$$

$$
\hat{a}_i^\dagger = \sqrt{\frac{m_i\omega_i}{2\hbar}} \left(\hat{q}_i - \frac{i}{m_i\omega_i} \hat{p}_i \right), \tag{1.22}
$$

with the commutation relation $\left[\hat{a}_i, \hat{a}_j^\dagger \right] = \delta_{ij}$. Using the displace harmonic oscillator

model, the electronic phonon interaction Hamiltonian can be specified in the following

way:

$$\hat{H}_{el-ph} = \sum_n |n\rangle\langle n| \otimes \sum_i \frac{1}{2} m_i \omega_i^2 \left[(\hat{q}_i - d_{ni})^2 - \hat{q}_i^2 \right]$$

$$= \sum_n \left(\sum_i \frac{1}{2} m_i \omega_i^2 d_{ni}^2 \right) |n\rangle\langle n| + \sum_n |n\rangle\langle n| \otimes \left(-\sum_i m_i \omega_i^2 d_{ni} \hat{q}_i \right)$$

$$= \sum_n \left(\sum_i \frac{1}{2} m_i \omega_i^2 d_{ni}^2 \right) |n\rangle\langle n| + \sum_n |n\rangle\langle n| \otimes \left(-\sum_i m_i \omega_i^2 d_{ni} (\hat{a}_i + \hat{a}_i^\dagger) \sqrt{\frac{\hbar}{2 m_i \omega_i}} \right)$$

$$= \sum_n \underbrace{\left(\sum_i \frac{1}{2} m_i \omega_i^2 d_{ni}^2 \right)}_{\lambda_n} |n\rangle\langle n| + \sum_n \underbrace{|n\rangle\langle n|}_{\hat{A}_n} \otimes \underbrace{\left(-\sum_i \sqrt{\frac{\hbar m_i \omega_i^3}{2}} d_{ni} (\hat{a}_i + \hat{a}_i^\dagger) \right)}_{\hat{B}_n}$$

$$= \underbrace{\sum_n \lambda_n |n\rangle\langle n|}_{\hat{H}_{reorg}} + \underbrace{\sum_n \hat{A}_n \otimes \hat{B}_n}_{\hat{H}_{SB}} . \tag{1.23}$$

where ω_i, $\hat{q}_i$, $\hat{p}_i$, $\hat{a}_i^\dagger$ and $\hat{a}_i$ are the angular frequency, position operator, momentum operator, raising and lowering operators for the ith normal mode coordinate, respectively. d_{ni} is the displacement of the ith oscillator for the nth exciton and only the Franck-Condon transition is assumed to occur during the dynamics. To apply the Redfield equation, the decomposition of the total system into the system and bath will be done in the following way:

$$\hat{H}_S = \hat{H}_{el} + \hat{H}_{reorg} = \sum_n (\varepsilon_n + \lambda_n)|n\rangle\langle n| + \sum_{m \neq n} E_{mn}|m\rangle\langle n|, \tag{1.24}$$

$$\hat{H}_B = \hat{H}_{ph} = \sum_i \hbar\omega_i \left(\hat{a}_i^\dagger \hat{a}_i + \frac{1}{2} \right), \tag{1.25}$$

$$\hat{H}_{SB} = \hat{H}_{el-ph} - \hat{H}_{reorg} = \sum_n \hat{A}_n \otimes \hat{B}_n. \tag{1.26}$$

Note that the first term of the RHS of Eq. 1.18 vanishes with this decomposition. Thus, evaluating the bath correlation would be enough to obtain the equation of

motion for the reduced density matrix of the system.

$$
\begin{aligned}
c_{mn}(t) &= \frac{1}{\hbar}\left\langle \tilde{B}_m^\dagger(t)\tilde{B}_n(0)\right\rangle \\
&= \sum_{i,j} \frac{\sqrt{m_i m_j \omega_i^3 \omega_j^3}}{2} d_{mi} d_{nj} \\
&\quad \times \mathrm{Tr}_B \frac{e^{\beta \hat{H}_B}}{Z(\beta)} e^{i\omega_i t\left(\hat{a}_i^\dagger \hat{a}_i + \frac{1}{2}\right)}(\hat{a}_i^\dagger + \hat{a}_i) e^{-i\omega_i t\left(\hat{a}_i^\dagger \hat{a}_i + \frac{1}{2}\right)}(\hat{a}_j^\dagger + \hat{a}_j).
\end{aligned}
\tag{1.27}
$$

From the commutation relation $[\hat{a}_i^\dagger, \hat{a}_i] = 1$,

$$
\hat{a}_i^\dagger e^{-i\omega_i t\left(\hat{a}^\dagger \hat{a}_i + \frac{1}{2}\right)} = e^{-i\omega_i t\left(\hat{a}^\dagger \hat{a}_i - \frac{1}{2}\right)}\hat{a}_i^\dagger,
\tag{1.28}
$$

$$
\hat{a}_i e^{-i\omega_i t\left(\hat{a}^\dagger \hat{a}_i + \frac{1}{2}\right)} = e^{-i\omega_i t\left(\hat{a}^\dagger \hat{a}_i + \frac{3}{2}\right)}\hat{a}_i
\tag{1.29}
$$

By plugging in Eq. 1.28 and 1.29 to Eq. 1.27, we obtain

$$
\begin{aligned}
c_{mn}(t) &= \sum_{i,j} \frac{\sqrt{m_i m_j \omega_i^3 \omega_j^3}}{2} d_{mi} d_{nj} \mathrm{Tr}_B \frac{e^{-\beta \hat{H}_B}}{Z(\beta)} \left(e^{i\omega_i t}\hat{a}_i^\dagger + e^{-i\omega_i t}\hat{a}_i\right)(\hat{a}_j^\dagger + \hat{a}_j) \\
&= \sum_i \frac{m_i \omega_i^3 d_{mi} d_{ni}}{2} \mathrm{Tr}_B \left\{ \frac{e^{-\beta \hat{H}_B}}{Z(\beta)} e^{i\omega_i t}\hat{a}_i^\dagger \hat{a}_i + \frac{e^{-\beta \hat{H}_B}}{Z(\beta)} e^{-i\omega_i t}\hat{a}_i \hat{a}_i^\dagger \right\} \\
&= \sum_i \frac{m_i \omega_i^3 d_{mi} d_{ni}}{2} \mathrm{Tr}_B \left\{ \frac{e^{-\beta \hat{H}_B}}{Z(\beta)} e^{i\omega_i t}\hat{a}_i^\dagger \hat{a}_i + \frac{e^{-\beta \hat{H}_B}}{Z(\beta)} e^{-i\omega_i t}(\hat{a}_i^\dagger \hat{a}_i + 1) \right\} \\
&= \sum_i \frac{m_i \omega_i^3 d_{mi} d_{ni}}{2} \left[n(\omega_i; \beta)e^{i\omega_i t} + \{n(\omega_i; \beta) + 1\}e^{-i\omega_i t} \right], \\
c_{mn}^*(t) &= \sum_i \frac{m_i \omega_i^3 d_{mi} d_{ni}}{2} \left[n(\omega_i; \beta)e^{-i\omega_i t} + \{n(\omega_i; \beta) + 1\}e^{i\omega_i t} \right],
\end{aligned}
\tag{1.30}
$$

where $Z(\beta) = \mathrm{Tr}_B e^{-\beta \hat{H}_B}$ is the partition function of the bath, and $n(\omega_i; \beta) = \frac{1}{e^{\beta \hbar \omega} - 1}$

is the Bose-Einstein distribution function at the inverse temperature β. Plugging in

to Eq. 1.13 and 1.14,

$$S_{kl}(t) = \sum_i \frac{m_i \omega_i^3 d_{mi} d_{ni}}{2} \{2n(\omega_i; \beta) + 1\} \left(e^{-i\omega_i t} + e^{i\omega_i t}\right)$$

$$= \sum_i \frac{m_i \omega_i^3 d_{mi} d_{ni}}{2} \{2n(\omega_i; \beta) + 1\} \{2\cos(\omega_i t)\}$$

$$= 2 \sum_i \frac{m_i \omega_i^3 d_{mi} d_{ni}}{2} \coth\left(\frac{\beta \hbar \omega_i}{2}\right) \cos(\omega_i t), \tag{1.31}$$

$$\chi_{kl}(t) = i \sum_i \frac{m_i \omega_i^3 d_{mi} d_{ni}}{2} \left(e^{-i\omega_i t} - e^{i\omega_i t}\right)$$

$$= i \sum_i \frac{m_i \omega_i^3 d_{mi} d_{ni}}{2} \{-2i \sin(\omega_i t)\}$$

$$= 2 \sum_i \frac{m_i \omega_i^3 d_{mi} d_{ni}}{2} \sin(\omega_i t). \tag{1.32}$$

For convenience, we will rewrite the Eq. 1.31 and 1.32 by defining the spectral density of the bath associated with the mth and nth excitons as

$$J_{mn}(\omega) = \sum_i \frac{m_i \omega^3 d_{mi} d_{ni}}{2} \delta(\omega - \omega_i). \tag{1.33}$$

For any macroscopic bath with many degrees of freedom, its spectral density is essentially a continuous function. The $S_{kl}(t)$ and $\chi_{kl}(t)$ can now be expressed in terms of the spectral density as integral equations with respect to ω. Because ω_i's are positive definite, the integration can be done only in the positive region.

$$S_{kl}(t) = 2 \int_0^\infty d\omega \ J_{mn}(\omega) \coth\left(\frac{\beta \hbar \omega}{2}\right) \cos(\omega t), \tag{1.34}$$

$$\chi_{kl}(t) = 2 \int_0^\infty d\omega \ J_{mn}(\omega) \sin(\omega t). \tag{1.35}$$

The Markovian master equation for a system coupled to a harmonic oscillator bath with linear coupling, like the displaced oscillator model, can be completely specified by spectral densities. One popular phenomological model for the spectral density is

an Ohmic spectral density with a Lorentz-Drude cutoff function:

$$J_{mn}(\omega) = \frac{2\lambda_{mn}}{\pi}\omega\frac{\Omega_{mn}}{\Omega_{mn}^2 + \omega^2}, \tag{1.36}$$

where λ_{mn} is the reorganization energy and Ω_{mn} is a high frequency cutoff constant. With this choice of spectral density, analytic expressions for the noise and dissipation kernels can be obtained:

$$S_{mn}(t) = \frac{4\lambda_{mn}}{\beta\hbar}\Omega_{mn}\left(\frac{e^{-\Omega_{mn}t}}{\Omega_{mn}} + \sum_{k=1}^{\infty}\frac{2\Omega_{mn}e^{-\Omega_{mn}t} - \nu_k e^{-\nu_k t}}{\Omega_{mn}^2 - \nu_k^2}\right), \tag{1.37}$$

$$\chi_{mn}(t) = 2\lambda_{mn}\Omega_{mn}e^{-\Omega_{mn}t}, \tag{1.38}$$

where $\nu_k = \frac{2\pi k}{\beta\hbar}$ are Matsubara frequencies. There exist alternative expressions known to be converge faster thatn the Matsubara series and they are often favored in actual implementations of the formalism[35–37]. For simplicity, only the high temperatures approximation of $S_{mn}(t) \approx \frac{4\lambda_{mn}}{\beta\hbar}e^{-\Omega_{mn}t}$ will be considered.

Under the assumptions of the Redfield equation, $\tilde{A}_k(t - s)$ can be approximated as a Taylor expansion up to the first order in s:

$$\tilde{A}_k(t - s) = \tilde{A}_k(t) - s\frac{d}{dt}\tilde{A}_k(t) = \tilde{A}_k(t) + \frac{s}{i\hbar}\left[\hat{H}_S, \tilde{A}_k(t)\right]. \tag{1.39}$$

Plugging in all above to Eq. 1.18 and integrating gives

$$\frac{d}{dt}\tilde{\rho}_S(t) \approx -\frac{1}{\hbar}\sum_{k,l}\int_0^\infty ds\,\frac{2\lambda_{kl}}{\beta\hbar}e^{-\Omega_{mn}s}\left[\tilde{A}_k(t),\left[\tilde{A}_l(t),\tilde{\rho}_S(t)\right]\right]$$

$$-\frac{1}{\hbar}\sum_{k,l}\int_0^\infty ds\,\frac{2\lambda_{kl}}{i\beta\hbar^2}se^{-\Omega_{mn}s}\left[\tilde{A}_k(t),\left[\left[\hat{H}_S,\tilde{A}_l(t)\right],\tilde{\rho}_S(t)\right]\right]$$

$$+\frac{1}{\hbar}\sum_{k,l}\int_0^\infty ds\,\frac{i\lambda_{mn}\Omega_{mn}}{\hbar}e^{-\Omega_{mn}s}\left[\tilde{A}_k(t),\left\{\tilde{A}_l(t),\tilde{\rho}_S(t)\right\}\right]$$

$$+\frac{1}{\hbar}\sum_{k,l}\int_0^\infty ds\,\frac{\lambda_{mn}\Omega_{mn}}{\hbar^2}se^{-\Omega_{mn}s}\left[\tilde{A}_k(t),\left\{\left[\hat{H}_S,\tilde{A}_l(t)\right],\tilde{\rho}_S(t)\right\}\right]$$

$$=-\frac{1}{\hbar}\sum_{k,l}\frac{2\lambda_{kl}}{\beta\hbar\Omega_{mn}}\left[\tilde{A}_k(t),\left[\tilde{A}_l(t),\tilde{\rho}_S(t)\right]\right]$$

$$+\frac{1}{\hbar}\sum_{k,l}\frac{2i\lambda_{kl}}{\beta\hbar^2\Omega_{mn}^2}\left[\tilde{A}_k(t),\left[\left[\hat{H}_S,\tilde{A}_l(t)\right],\tilde{\rho}_S(t)\right]\right]$$

$$+\frac{1}{\hbar}\sum_{k,l}\frac{i\lambda_{mn}}{\hbar}\left[\tilde{A}_k(t),\left\{\tilde{A}_l(t),\tilde{\rho}_S(t)\right\}\right]$$

$$+\frac{1}{\hbar}\sum_{k,l}\frac{\lambda_{mn}}{\hbar^2\Omega_{mn}}\left[\tilde{A}_k(t),\left\{\left[\hat{H}_S,\tilde{A}_l(t)\right],\tilde{\rho}_S(t)\right\}\right]. \tag{1.40}$$

If expressed in the Schrödinger picture, the generator of the quantum master equation does not depend on time:

$$\frac{d}{dt}\rho_S(t) = \frac{1}{i\hbar}\left[\hat{H}_S,\rho(t)\right] - \frac{1}{\hbar}\sum_{k,l}\frac{2\lambda_{kl}}{\beta\hbar\Omega_{mn}}\left[\hat{A}_k,\left[\hat{A}_l,\rho_S(t)\right]\right]$$

$$+\frac{1}{\hbar}\sum_{k,l}\frac{2i\lambda_{kl}}{\beta\hbar^2\Omega_{mn}^2}\left[\hat{A}_k,\left[\left[\hat{H}_S,\hat{A}_l\right],\rho_S(t)\right]\right]$$

$$+\frac{1}{\hbar}\sum_{k,l}\frac{i\lambda_{mn}}{\hbar}\left[\hat{A}_k,\left\{\hat{A}_l,\rho_S(t)\right\}\right]$$

$$+\frac{1}{\hbar}\sum_{k,l}\frac{\lambda_{mn}}{\hbar^2\Omega_{mn}}\left[\hat{A}_k,\left\{\left[\hat{H}_S,\hat{A}_l\right],\rho_S(t)\right\}\right]. \tag{1.41}$$

1.1.3   Reduced Hierarchical Equation of Motion

The Born approximation employed in the Redfield equation leads to the perturbation expansion to the second order. Due to this limitation, the Redfield equation is not applicable when the system-bath interaction is of comparable scale to the site-site coupling [28]. Also, non-Markovian effects cannot be captured because the bath correlation time is assumed to be short. For a harmonic oscillator bath with Ohmic spectral density and Lorentz-Drude cutoff, a non-perturbative and non-Markovian equation of motion can be derived by exploiting the following facts: (1) The noise and dissipation kernels are linear combinations of exponential functions of time and (2) the system-bath interaction Hamiltonian is linear in the position operators of bath oscillators. We now derive this non-Markovian master equation.

Starting from the previous decomposition for the Hamiltonian of Frenkel excitons in Eq. 1.24-1.26 and substituting to Eq. 1.4, we obtain

$$\frac{d}{dt}\tilde{\rho}(t) = \frac{1}{i\hbar}\left[\tilde{H}_{SB}, \tilde{\rho}(t)\right]$$
$$= \frac{1}{i\hbar}\sum_k \left\{\tilde{\mathcal{A}}_k(t)\otimes\tilde{\mathcal{B}}_k(t)\right\}\tilde{\rho}(t), \qquad (1.42)$$

where

$$\tilde{\mathcal{A}}_k(t)\sigma = \left[\tilde{A}_k(t),\sigma\right], \tilde{\mathcal{A}}_k^{\dagger}(t)\sigma = \left[\tilde{A}_k^{\dagger}(t),\sigma\right],$$
$$\tilde{\mathcal{B}}_k(t)\sigma = \left[\tilde{B}_k(t),\sigma\right], \tilde{\mathcal{B}}_k^{\dagger}(t)\sigma = \left[\tilde{B}_k^{\dagger}(t),\sigma\right]. \qquad (1.43)$$

The formal solution of the Eq.1.42 is,

$$\tilde{\rho}(t) = T_{\leftarrow}\exp\left(\frac{1}{i\hbar}\int_0^t ds \ \sum_k \tilde{\mathcal{A}}_k(s)\otimes\tilde{\mathcal{B}}_k(s)\right)\tilde{\rho}(0), \qquad (1.44)$$

15

where $T_\leftarrow$ is the chronological time ordering operator. By assuming that the initial state is factorizable, $\tilde{\rho}(0) = \tilde{\rho}_S(0) \otimes \tilde{\rho}_B$, where the bath is in equilibrium like Eq. 1.10, the reduced density matrix of the system can be written as,

$$\tilde{\rho}_S(t) = T_\leftarrow \left\langle \exp\left(\frac{1}{i\hbar}\int_0^t ds \, \sum_k \tilde{\mathcal{A}}_k(s) \otimes \tilde{\mathcal{B}}_k(s)\right)\right\rangle \tilde{\rho}(0). \qquad (1.45)$$

The bath operators $\tilde{B}_k(t)$ are linear in the bath position operators. By applying Kubo's generalized cumulant expansion [38], the equation above can be expressed as,

$$\tilde{\rho}_S(t) = T_\leftarrow \left\langle \exp\left(\frac{1}{i\hbar}\int_0^t ds \, \sum_k \tilde{\mathcal{A}}_k(s) \otimes \tilde{\mathcal{B}}_k(s)\right)\right\rangle \tilde{\rho}(0)$$

$$= T_\leftarrow \exp\left(-\frac{1}{\hbar^2}\sum_k \int_0^t dt_1 \int_0^{t_1} ds_1 \left\langle \left\{\tilde{\mathcal{A}}_k^\dagger(t_1) \otimes \tilde{\mathcal{B}}_k^\dagger(t_1)\right\}\left\{\tilde{\mathcal{A}}_k(s_1) \otimes \tilde{\mathcal{B}}_k(s_1)\right\}\right\rangle\right) \tilde{\rho}(0).$$

$$(1.46)$$

The integrand of Eq. 1.46 can be explicitly evaluated by adapting an Ohmic spectral density in Eq. 1.36:

$$-\frac{1}{\hbar^2}\left\langle \left\{\tilde{\mathcal{A}}_k^\dagger(t_1) \otimes \tilde{\mathcal{B}}_k^\dagger(t_1)\right\}\left\{\tilde{\mathcal{A}}_k(s_1) \otimes \tilde{\mathcal{B}}_k(s_1)\right\}\right\rangle = \tilde{\mathcal{F}}_k(t_1) e^{-\Omega_k(t_1-s_1)}\tilde{\mathcal{T}}_k(s_1), \qquad (1.47)$$

where $\tilde{\mathcal{F}}_k(t)$ and $\tilde{\mathcal{T}}_k(t)$ are superoperators defined as,

$$\tilde{\mathcal{F}}_k(t) = i\left[\tilde{A}_k^\dagger(t), \sigma\right],$$

$$\tilde{\mathcal{T}}_k(t) = \frac{2i\lambda_k}{\beta\hbar^2}\left[\tilde{A}_k(t), \sigma\right] + \frac{\lambda_k\Omega_k}{\hbar}\left\{\tilde{A}_k(t), \sigma\right\}. \qquad (1.48)$$

For algebraic convenience, we assumed that the bath operators coupled to different sites are uncorrelated. Rewriting Eq. 1.46 using these superoperators, the reduced density matrix can be obtained as,

$$\tilde{\rho}_S(t) = T_\leftarrow \exp\left(\sum_k \int_0^t dt_1 \tilde{\mathcal{F}}_k(t_1) \int_0^{t_1} ds_1 \, e^{-\Omega_k(t_1-s_1)}\tilde{\mathcal{T}}_k(s_1)\right) \tilde{\rho}_S(0)$$

$$= T_\leftarrow \left\{\prod_k \exp\left(\int_0^t dt_1 \tilde{\mathcal{F}}_k(t_1) \int_0^{t_1} ds_1 \, e^{-\Omega_k(t_1-s_1)}\tilde{\mathcal{T}}_k(s_1)\right)\right\} \tilde{\rho}_S(0), \qquad (1.49)$$

Differentiating both sides of Eq. 1.49,

$$\frac{d}{dt}\tilde{\rho}_S(t) = T_\leftarrow \sum_l \tilde{\mathcal{F}}_l(t) \left(\int_0^t ds \; e^{-\Omega_k(t_1-s_1)} \tilde{\mathcal{T}}_l(s) \right)$$

$$\times \left\{ \prod_k \exp\left(\int_0^t dt_1 \tilde{\mathcal{F}}_k(t_1) \int_0^{t_1} ds_1 \; e^{-\Omega_k(t_1-s_1)} \tilde{\mathcal{T}}_k(s_1) \right) \right\} \tilde{\rho}_S(0)$$

$$= \sum_l \tilde{\mathcal{F}}_l(t) T_\leftarrow \left(\int_0^t ds \; e^{-\Omega_k(t_1-s_1)} \tilde{\mathcal{T}}_l(s) \right)$$

$$\times \left\{ \prod_k \exp\left(\int_0^t dt_1 \tilde{\mathcal{F}}_k(t_1) \int_0^{t_1} ds_1 \; e^{-\Omega_k(t_1-s_1)} \tilde{\mathcal{T}}_k(s_1) \right) \right\} \tilde{\rho}_S(0)$$

$$= \sum_l \tilde{\mathcal{F}}_l(t) \tilde{\sigma}_{\{\cdots,n_{l-1}=0,n_l=1,n_{l+1}=0,\cdots\}}(t), \tag{1.50}$$

where auxiliary matrices $\tilde{\sigma}_{\{n_1,\cdots,n_N\}}$ are defined as,

$$\tilde{\sigma}_{\{n_1,\cdots,n_N\}}(t) = T_\leftarrow \prod_k \left(\int_0^t ds \; e^{-\Omega_k(t-s)} \tilde{\mathcal{T}}_k(s) \right)^{n_k}$$

$$\times \exp\left(\int_0^t dt_1 \tilde{\mathcal{F}}_k(t_1) \int_0^{t_1} ds_1 \; e^{-\Omega_k(t_1-s_1)} \tilde{\mathcal{T}}_k(s_1) \right) \tilde{\rho}_S(0), \tag{1.51}$$

and it becomes zero if any element in $\{n_k\}$ is negative. Note that $\tilde{\rho}_S(t) = \tilde{\sigma}_{\{0,\cdots,0\}}(t)$ and $\tilde{\sigma}_{\{n_1,\cdots,n_N\}}(0) = 0$. The equation of motion of $\tilde{\sigma}_{\{n_1,\cdots,n_N\}}(t)$ is,

$$\frac{d}{dt}\tilde{\sigma}_{\{n_1,\cdots,n_N\}}(t) = -\sum_l \Omega_l \tilde{\sigma}_{\{n_1,\cdots,n_N\}}$$

$$+ \sum_l n_l \tilde{\mathcal{T}}_l(t) \tilde{\sigma}_{\{n_1,\cdots,n_l-1,\cdots,n_N\}} + \sum_l \tilde{\mathcal{F}}_l(t) \tilde{\sigma}_{\{n_1,\cdots,n_l+1,\cdots,n_N\}}, \tag{1.52}$$

in the interaction picture. Moving to the Schrödinger picture, we obtain a set of hierarchical equations of motion.

$$\frac{d}{dt}\sigma_{\{n_1,\cdots,n_N\}}(t) = \frac{1}{i\hbar}\mathcal{L}_S \sigma_{\{n_1,\cdots,n_N\}} - \sum_l \Omega_l \sigma_{\{n_1,\cdots,n_N\}}$$

$$+ \sum_l n_l \mathcal{T}_l(t) \sigma_{\{n_1,\cdots,n_l-1,\cdots,n_N\}} + \sum_l \mathcal{F}_l(t) \sigma_{\{n_1,\cdots,n_l+1,\cdots,n_N\}}. \tag{1.53}$$

1.1.4 Haken-Strobl-Reineker Model

First developed by Haken, Strobl and Reineker [39–41], this phenomenological stochastic model describes the coherent and incoherent dynamics of Frenkel excitons at the same time. Instead of decompose the total complex to the system and bath, Haken-Strobl-Reineker (HSR) model mainly focuses on the system Hamiltonian, and the effect of the bath environment is included as time-dependent stochastic terms:

$$\hat{H}_{sys} = \sum_n \varepsilon_n |n\rangle\langle n| + \sum_{m \neq n} E_{mn} |m\rangle\langle n|,$$

$$\hat{H}_{env}(t) = \sum_{m,n} h_{mn}(t) |m\rangle\langle n|,$$

$$\hat{H}_{total}(t) = \hat{H}_{sys} + \hat{H}_{env}(t). \tag{1.54}$$

Realized stochastic density matrix $\breve{\rho}_S(t)$ can be defined per realization of the stochastic Hamiltonian according to the usual form of the quantum Liouville equation:

$$\begin{aligned}
\frac{d\breve{\rho}_S(t)}{dt} &= \frac{1}{i\hbar} \left[\hat{H}_{total}, \breve{\rho}_S(t) \right] \\
&= \frac{1}{i\hbar} \left[\hat{H}_{sys}, \breve{\rho}_S(t) \right] + \frac{1}{i\hbar} \left[\hat{H}_{env}(t), \breve{\rho}_S(t) \right]. \tag{1.55}
\end{aligned}$$

Then the reduced density matrix of the system can be obtained as the expectation of the density matrices over the realized trajectory:

$$\rho_S(t) = \mathbb{E}\left(\breve{\rho}_S(t) \right). \tag{1.56}$$

Note that $\breve{\rho}_S(t)$ is a stochastic process while $\rho_S(t)$ is deterministic. Equivalently, the equation of the motion for the reduced density matrix of the system can be obtained by taking expectation on both sides of Eq. 1.55:

$$\frac{d\rho_S(t)}{dt} = \frac{1}{i\hbar} \left[\hat{H}_{sys}, \rho_S(t) \right] + \frac{1}{i\hbar} \mathbb{E}\left(\left[\hat{H}_{env}(t), \breve{\rho}_S(t) \right] \right). \tag{1.57}$$

$h_{mn}(t)$ are assumed to have the correlation functions given by

$$\mathbb{E}\left\{h_{mn}(t)h_{nm}(t')\right\} = \frac{\hbar\gamma_{mn}}{\tau_c}e^{-\frac{|t-t'|}{\tau_c}}, \gamma_{mn} = \gamma_{nm},$$

$$\mathbb{E}\left\{h_{mn}(t)h_{mn}(t')\right\} = \frac{\hbar\bar{\gamma}_{mn}}{\tau_c}e^{-\frac{|t-t'|}{\tau_c}}, \bar{\gamma}_{mn} = \bar{\gamma}_{nm}^*, \tag{1.58}$$

where τ_c is the correlation time. The mean values can be set to zero by absorbing any leftover term into the system Hamiltonian. In the original parametrization, these stochastic terms were assumed to have delta function correlation in time. There exist a formulation with exponential correlation function for a two-exciton system [42], but the derivation presented here is generalized to cover any number of excitons. The constant $\hbar$ was introduced for γ_{mn} to have the unit of energy. Although an extension of the HSR model with nonzero intersite correlations exists [43], only the formulation with uncorrelated sites will be discussed in this chapter because of its simplicity and clarity.

To evaluate the second term of Eq. 1.57, we will rewrite the equation using an orthonormal basis set $\{\Omega_k\}$ spanning the density operator space with the following inner product [44]:

$$\langle\Omega_k|\Omega_l\rangle \equiv \text{Tr}(\Omega_k^\dagger\Omega_l) = \delta_{kl}. \tag{1.59}$$

With this orthonormal basis, the commutation relation between operators can be interpreted as a linear operator acting on the aforementioned vector space:

$$\begin{aligned}
\mathcal{H}\Omega_l &= \left[\hat{H}, \Omega_l\right] \\
&= \sum_k \text{Tr}\left(\Omega_k^\dagger\left[\hat{H}, \Omega_l\right]\right)\Omega_k \\
&= \sum_k \text{Tr}\left(\hat{H}\left[\Omega_l, \Omega_k^\dagger\right]\right)\Omega_k. \tag{1.60}
\end{aligned}$$

Then, Eq. 1.55 can be rewritten as

$$\frac{d}{dt}|\breve{\rho}_S(t)\rangle = \frac{1}{i\hbar}\mathcal{H}_{sys}|\breve{\rho}_S(t)\rangle + \frac{1}{i\hbar}\mathcal{H}_{env}|\breve{\rho}_S(t)\rangle, \tag{1.61}$$

where $|\breve{\rho}_S(t)\rangle = \sum_k \text{Tr}(\Omega_k^\dagger \breve{\rho}_S)\Omega_k$, $\mathcal{H}_{sys} = \sum_{k,l} \text{Tr}\left(\hat{H}_{sys}\left[\Omega_l, \Omega_k^\dagger\right]\right)|\Omega_k\rangle\langle\Omega_l|$ and $\mathcal{H}_{env} = \sum_{k,l} \text{Tr}\left(\hat{H}_{env}\left[\Omega_l, \Omega_k^\dagger\right]\right)|\Omega_k\rangle\langle\Omega_l|$.

Because the initial state is same for all instances of the trajectories, a closed form of a realization of the density matrix can be obtained by integrating Eq. 1.61:

$$|\breve{\rho}_S(t)\rangle = T_\leftarrow \exp\left(\frac{1}{i\hbar}\int_0^t ds\ \mathcal{H}_{sys}\right)T_\leftarrow \exp\left(\frac{1}{i\hbar}\int_0^t ds\ \mathcal{H}_{env}(s)\right)|\rho_S(0)\rangle, \tag{1.62}$$

where $T_\leftarrow$ is the chronological time-ordering operator. Taking expectation on both sides, the vector expression for the system density matrix can be obtained:

$$|\rho_S(t)\rangle = T_\leftarrow \exp\left(\frac{1}{i\hbar}\int_0^t ds\ \mathcal{H}_{sys}\right)\mathbb{E}\left\{T_\leftarrow \exp\left(\frac{1}{i\hbar}\int_0^t ds\ \mathcal{H}_{env}(s)\right)\right\}|\rho_S(0)\rangle. \tag{1.63}$$

Note that $\langle\Omega_k|\mathcal{H}_{env}|\Omega_l\rangle = \text{Tr}\left(\Omega_k^\dagger\left[\hat{H}_{env}, \Omega_l\right]\right)$ is also a stationary Gaussian random process with zero mean and correlation time τ_c because the term is linear in $h_{mn}(t)$'s:

$$\mathbb{E}\left\{\mathcal{H}_{env}(t_2)\mathcal{H}_{env}(t_1)\right\} = \frac{\hbar}{\tau_c}e^{-\frac{|t_2-t_1|}{\tau_c}}\mathcal{E} \tag{1.64}$$

$\mathcal{E}$ is a constant superoperator and has the unit of energy. The expectation of an operator appearing in Eq. 1.63 can be rewritten using only the second moments by Kubo's generalized cumulant expansion [38]:

$$\mathbb{E}\left\{T_\leftarrow \exp\left(\frac{1}{i\hbar}\int_0^t ds\ \mathcal{H}_{env}\right)\right\} = T_\leftarrow \exp\left(-\frac{1}{\hbar^2}\int_0^t dt_2 \int_0^{t_2} dt_1\ \mathbb{E}\left\{\mathcal{H}_{env}(t_2)\mathcal{H}_{env}(t_1)\right\}\right)$$

$$= T_\leftarrow \exp\left(-\frac{1}{\hbar}\int_0^t dt_2 \int_0^{t_2} dt_1\ \frac{1}{\tau_c}e^{-\frac{|t_2-t_1|}{\tau_c}}\mathcal{E}\right)$$

$$= T_\leftarrow \exp\left\{-\frac{1}{\hbar}\int_0^t dt_2\ \left(1 - e^{-\frac{t_2}{\tau_c}}\right)\mathcal{E}\right\}. \tag{1.65}$$

Plugging in this result to Eq. 1.63 gives

$$|\rho_S(t)\rangle = T_\leftarrow \exp\left(\frac{1}{i\hbar}\int_0^t ds\ \mathcal{H}_{sys}\right) T_\leftarrow \exp\left\{-\frac{1}{\hbar}\int_0^t dt_2\ \left(1 - e^{-\frac{t_2}{\tau_c}}\right)\mathcal{E}\right\}|\rho_S(0)\rangle.$$

(1.66)

By differentiating the equation above, we can come up with the generator for the vector representation of the density matrix.

$$\frac{d}{dt}|\rho_S(t)\rangle = \frac{1}{i\hbar}\left\{\mathcal{H}_{sys} - i\left(1 - e^{-\frac{t}{\tau_c}}\right)\mathcal{E}\right\}|\rho_S(t)\rangle.$$

(1.67)

For the practical use, we want to obtain the equation of motion for each element of the density matrix of the system. Those equations can be obtained by choosing $\Omega_k = |k_1\rangle\langle k_2|$. k is the collective index for (k_1, k_2) in this case and $|\Omega_k\rangle$ is equivalent to $|k_1, k_2\rangle$.

$$\frac{d}{dt}\langle k_1|\rho_S(t)|k_2\rangle = \langle k_1, k_2|\frac{d}{dt}|\rho_S(t)\rangle$$

$$= \frac{1}{i\hbar}\langle k_1, k_2|\mathcal{H}_{sys}|\rho_S(t)\rangle - \frac{1}{\hbar}\left(1 - e^{-\frac{t}{\tau_c}}\right)\langle k_1, k_2|\mathcal{E}|\rho_S(t)\rangle.$$

(1.68)

The explicit form of the $\mathbb{E}\left\{\mathcal{H}_{env}(t_1)\mathcal{H}_{env}(t_2)\right\}$ need to be found to evaluate the second term of Eq. 1.68.

$$\mathcal{H}_{env}(t_2)\mathcal{H}_{env}(t_1) = \sum_{k,l}\sum_j \mathrm{Tr}\left(\hat{H}_{env}(t_2)\left[\Omega_j, \Omega_k^\dagger\right]\right)\mathrm{Tr}\left(\hat{H}_{env}(t_1)\left[\Omega_l, \Omega_j^\dagger\right]\right)|\Omega_k\rangle\langle\Omega_l|,$$

(1.69)

where the prefactors of the superoperator $\mathcal{H}_{env}$ are

$$\mathrm{Tr}\left(\hat{H}_{env}(t)\left[\Omega_l, \Omega_k^\dagger\right]\right) = \mathrm{Tr}\left\{\sum_{m,n} h_{mn}(t)\left(|m\rangle\langle n|l_1\rangle\langle l_2|k_2\rangle\langle k_1| - |l_1\rangle\langle l_2|m\rangle\langle n|k_2\rangle\langle k_1|\right)\right\}$$

$$= \mathrm{Tr}\left\{\sum_m \delta_{k_2 l_2} h_{ml_1}(t)|m\rangle\langle k_1| - h_{l_2 k_2}(t)|l_1\rangle\langle k_1|\right\}$$

$$= \delta_{k_2 l_2} h_{k_1 l_1}(t) - \delta_{k_1 l_1} h_{l_2 k_2}(t).$$

(1.70)

By plugging in Eq. 1.70 to Eq. 1.69,

$$\sum_j \mathrm{Tr}\left(\hat{H}_{env}(t_2)\left[\Omega_j, \Omega_k^\dagger\right]\right)\mathrm{Tr}\left(\hat{H}_{env}(t_1)\left[\Omega_l, \Omega_j^\dagger\right]\right)$$

$$= \sum_{j_1,j_2}\left\{\delta_{k_2 j_2}h_{k_1 j_1}(t_2) - \delta_{k_1 j_1}h_{j_2 k_2}(t_1)\right\}\left\{\delta_{j_2 l_2}h_{j_1 l_1}(t_2) - \delta_{j_1 l_1}h_{l_2 j_2}(t_1)\right\}$$

$$= \sum_{j_1}\delta_{k_2 l_2}h_{k_1 j_1}(t_2)h_{j_1 l_1}(t_1) - h_{k_1 l_1}(t_2)h_{l_2 k_2}(t_1)$$

$$- h_{l_2 k_2}(t_2)h_{k_1 l_1}(t_1) + \sum_{j_2}\delta_{k_1 l_1}h_{j_2 k_2}(t_2)h_{l_2 j_2}(t_1)$$

$$= -h_{k_1 l_1}(t_2)h_{l_2 k_2}(t_1) - h_{l_2 k_2}(t_2)h_{k_1 l_1}(t_1)$$

$$+ \sum_j \delta_{k_2 l_2}h_{k_1 j}(t_2)h_{j l_1}(t_1) + \sum_j \delta_{k_1 l_1}h_{j k_2}(t_2)h_{l_2 j}(t_1). \tag{1.71}$$

To calculate the second term on the right hand side of Eq. 1.68, the following term should be evaluated first:

$$\langle k_1, k_2|\mathbb{E}\left\{\mathcal{H}_{env}(t_2)\mathcal{H}_{env}(t_1)\right\}|\rho_S(t)\rangle$$

$$= -\sum_{l_1,l_2}\mathbb{E}\left\{h_{k_1 l_1}(t_2)h_{l_2 k_2}(t_1)\right\}\langle l_1|\rho_S(t)|l_2\rangle - \sum_{l_1,l_2}\mathbb{E}\left\{h_{l_2 k_2}(t_2)h_{k_1 l_1}(t_1)\right\}\langle l_1|\rho_S(t)|l_2\rangle$$

$$+ \sum_{l_1,l_2}\sum_j \mathbb{E}\left\{\delta_{k_2 l_2}h_{k_1 j}(t_2)h_{j l_1}(t_1)\right\}\langle l_1|\rho_S(t)|l_2\rangle$$

$$+ \sum_{l_1,l_2}\sum_j \mathbb{E}\left\{\delta_{k_1 l_1}h_{j k_2}(t_2)h_{l_2 j}(t_1)\right\}\langle l_1|\rho_S(t)|l_2\rangle. \tag{1.72}$$

For the diagonal elements, or for $k_1 = k_2 = k$,

$$\langle k, k | \mathbb{E} \left\{ \mathcal{H}_{env}(t_2) \mathcal{H}_{env}(t_1) \right\} | \rho_S(t) \rangle$$

$$= - \sum_{l_1, l_2} \mathbb{E} \left\{ h_{kl_1}(t_2) h_{l_2k}(t_1) \right\} \langle l_1 | \rho_S(t) | l_2 \rangle - \sum_{l_1, l_2} \mathbb{E} \left\{ h_{l_2k}(t_2) h_{kl_1}(t_1) \right\} \langle l_1 | \rho_S(t) | l_2 \rangle$$

$$+ \sum_{l_1, l_2} \sum_{j} \mathbb{E} \left\{ \delta_{kl_2} h_{kj}(t_2) h_{jl_1}(t_1) \right\} \langle l_1 | \rho_S(t) | l_2 \rangle$$

$$+ \sum_{l_1, l_2} \sum_{j} \mathbb{E} \left\{ \delta_{kl_1} h_{jk}(t_2) h_{l_2j}(t_1) \right\} \langle l_1 | \rho_S(t) | l_2 \rangle$$

$$= - \sum_{j} \frac{\hbar \left(\gamma_{kj} + \gamma_{jk} \right)}{\tau_c} e^{-\frac{|t_2 - t_1|}{\tau_c}} \langle j | \rho_S(t) | j \rangle + \sum_{j} \frac{\hbar \left(\gamma_{kj} + \gamma_{jk} \right)}{\tau_c} e^{-\frac{|t_2 - t_1|}{\tau_c}} \langle k | \rho_S(t) | k \rangle.$$

$$(1.73)$$

Therefore,

$$\langle k, k | \mathcal{E} | \rho_S(t) \rangle = - \sum_{j} \left(\gamma_{kj} + \gamma_{jk} \right) \langle j | \rho_S(t) | j \rangle + \sum_{j} \left(\gamma_{kj} + \gamma_{jk} \right) \langle k | \rho_S(t) | k \rangle. \quad (1.74)$$

Plugging in Eq. 1.74 to Eq. 1.68,

$$\frac{d}{dt} \langle k | \rho_S(t) | k \rangle = \frac{1}{i\hbar} \langle k | \left[\hat{H}_{sys}, \rho_S(t) \right] | k \rangle + \left(1 - e^{-\frac{t}{\tau_c}} \right) \sum_{j} \frac{\gamma_{kj} + \gamma_{jk}}{\hbar} \langle j | \rho_S(t) | j \rangle$$

$$- \left(1 - e^{-\frac{t}{\tau_c}} \right) \sum_{j} \frac{\gamma_{kj} + \gamma_{jk}}{\hbar} \langle k | \rho_S(t) | k \rangle. \quad (1.75)$$

Similarly, for the off-diagonal elements, $k_1 \neq k_2$,

$$\langle k_1, k_2 | \mathbb{E}\left\{\mathcal{H}_{env}(t_2)\mathcal{H}_{env}(t_1)\right\} | \rho_S(t)\rangle$$

$$= -\sum_{l_1,l_2} \mathbb{E}\left\{h_{k_1 l_1}(t_2)h_{l_2 k_2}(t_1)\right\}\langle l_1|\rho_S(t)|l_2\rangle - \sum_{l_1,l_2} \mathbb{E}\left\{h_{l_2 k_2}(t_2)h_{k_1 l_1}(t_1)\right\}\langle l_1|\rho_S(t)|l_2\rangle$$

$$+ \sum_{l_1,l_2}\sum_{j} \mathbb{E}\left\{\delta_{k_2 l_2}h_{k_1 j}(t_2)h_{j l_1}(t_1)\right\}\langle l_1|\rho_S(t)|l_2\rangle$$

$$+ \sum_{l_1,l_2}\sum_{j} \mathbb{E}\left\{\delta_{k_1 l_1}h_{j k_2}(t_2)h_{l_2 j}(t_1)\right\}\langle l_1|\rho_S(t)|l_2\rangle$$

$$= -\frac{2\hbar\bar{\gamma}_{k_1 k_2}}{\tau_c}e^{-\frac{|t_2-t_1|}{\tau_c}}\langle k_2|\rho_S(t)|k_1\rangle$$

$$+ \sum_{j}\frac{\hbar\gamma_{k_1 j}}{\tau_c}e^{-\frac{|t_2-t_1|}{\tau_c}}\langle k_1|\rho_S(t)|k_2\rangle + \sum_{j}\frac{\hbar\gamma_{j k_2}}{\tau_c}e^{-\frac{|t_2-t_1|}{\tau_c}}\langle k_1|\rho_S(t)|k_2\rangle. \qquad (1.76)$$

Therefore,

$$\langle k_1, k_2 | \mathcal{E} | \rho_S(t)\rangle = -2\bar{\gamma}_{k_1 k_2}\langle k_2|\rho_S(t)|k_1\rangle + \sum_{j}\left(\gamma_{k_1 j} + \gamma_{j k_2}\right)\langle k_1|\rho_S(t)|k_2\rangle. \qquad (1.77)$$

Plugging in Eq. 1.77 to Eq. 1.68,

$$\frac{d}{dt}\langle k_1|\rho_S(t)|k_2\rangle = \frac{1}{i\hbar}\langle k_1|\left[\hat{H}_{sys}, \rho_S(t)\right]|k_2\rangle + \left(1 - e^{-\frac{t}{\tau_c}}\right)\frac{2\bar{\gamma}_{k_1 k_2}}{\hbar}\langle k_2|\rho_S(t)|k_1\rangle$$

$$- \left(1 - e^{-\frac{t}{\tau_c}}\right)\sum_{j}\frac{\gamma_{k_1 j} + \gamma_{j k_2}}{\hbar}\langle k_1|\rho_S(t)|k_2\rangle. \qquad (1.78)$$

Note that in the completely memoryless bath limit of $\tau_c \to 0$, the original Haken-Strobl-Reineker fomulation is restored.

Part I

Quantum Coherences in Light

Harvesting Systems

Chapter 2

Characterization and quantification of the role of coherence in ultrafast quantum biological experiments

2.1 Introduction

The initial step in photosynthesis is highly efficient excitonic transport of the energy captured from photons to a reaction center [45]. In most plants and photosynthetic organisms this process occurs in light-harvesting complexes which are interacting chlorophyll molecules embedded in a solvent and a protein environment [46]. Several recent experiments show that excitonic coherence can persist for several hundreds of femtoseconds even at physiological temperature [23–25, 47]. These experiments suggest the hypothesis that quantum coherence is biologically relevant for photosynthesis. The results have motivated a sizeable amount of recent theoretical

work regarding the reasons for the long-lived coherences and their role to the function.

The focus of many studies is on the theoretical models employed. In this context, it is essential to be as realistic an possible and employ the least amount of approximations. Most of the currently-employed methods involve a master equation for the reduced excitonic density operator where the vibrational degrees of freedom (phonons) of the protein and solvent are averaged out. Amongst these simple methods are the Haken-Strobl model and Redfield theory as employed in Refs. 27, 48 and 49 respectively. To interpolate between the usual weak and strong exciton-phonon coupling limits, Ishizaki and Fleming developed a hierarchical equation of motion (HEOM) theory which takes into account non-equilibrium molecular reorganization effects [29]. Jang et al. perform a second order time-convolutionless expansion after a small polaron transformation to include strong coupling effects [50]. Another set of studies focuses on the role of quantum coherence and the phonon environmentin terms of transport efficiency or entanglement. It was shown that the transport efficiency is enhanced by the interaction or interplay of the quantum evolution with the phononic environment [27, 48, 49, 51]. Entanglement between molecules is found to persist for long times [52–54].

The ongoing effort can be summarized with two equally important questions: What are the microscopic reasons for the persistence of quantum coherence and what is the relevance of the quantum effect to the biological functionality of the organism under study? In this work, we summarize the recent efforts from our group to approach the problem from several angles. Firstly, we investigate the role of coherences in the exciton transfer process of the Fenna-Matthews-Olson (FMO) complex.

We quantify the amount and the contribution of coherence to the efficient energy transfer process. Secondly, we present our quantum mechanics/molecular mechanics (QM/MM) approach to obtain information about the system at the atomistic level, such as detailed bath dynamics and spectral densities. Finally, we propose a spectroscopic tool that allows for obtaining directly the information of the quantum process via our recent theoretical proposal for the quantum process tomography technique to the ultrafast regime.

2.2   The Role of Quantum Coherence

In this section, we discuss the question about the relevance of quantum effects to the biological function. A negative answer to this question would mean that a particular effect, while being quantum, is not leading to any improvement in the functionality of a biological system, and therefore would be a byproduct of the spatial and temporal scales and physical properties of the problem. For example, in energy transfer (ET) quantum coherence could arise from the closely packed arrangement of the chromophores in a protein scaffold but it could, in principle, represent a byproduct of that arrangement and not a relevant feature. Another example, it may be true that the human eye can detect a single photon, but it is not clear if this quantum effect is relevant to the biological function, which usually operates at much larger photon fluxes. If, on the other hand, the above yes-no question of the relevance is answered positively for a particular effect in a biological system, it would present a major step towards establishing the relevance or importance of a quantum biological phenomenon. A natural follow-up questions is: How important *quantitatively* is a

particular quantum effect?

Both of these questions should preferably be studied by experimental means. An experiment would have to be designed in a way that tests for the biological relevance of quantum coherence. Possible experiments could involve quantum measurements on mutated samples. In the FMO complex that acts as a molecular ET wire the efficiency of the transport event is most likely a good quantifier for biological function. One would need a way to experimentally quantify this efficiency and extract the relevance of quantum coherence to the efficiency. This can be hard in practice. Yet, as we will discuss in this work, quantum process tomography is able to obtain detailed information about quantum coherence and the phonon environment and might thus lead to progress in this area.

In the case when experimental access to an observable that involves the biological relevance is hard or impossible, a theoretical treatment can provide insight. It is illustrative to analyze a model of the particular biological process in terms of a quantifier for the success of the process. An example is the aforementioned efficiency of energy transport. In bird vision, the quantum yield of a chemical reaction is a relevant measure [55]. Once a detailed model and a success criterion is established, one needs to quantify the contribution of quantum coherence to the success criterion. For this step, one can proceed in two distinct pathways. The first pathway is a comparison to a classical reference point; the success criterion is computed for the actual system/model and a classical reference model that does not include quantum correlations. The difference of these two values is attributed to quantum mechanics and can be considered the quantum mechanical contribution to the success of the process. For

example, the energy transfer dynamics of a sophisticated quantum mechanical model such as [29] could be compared to a semi-classical Förster treatment that leads to a hopping description. In general, this comparison strategy has the drawback that one has to invoke a classical, and in some cases very artificial, model.

Our work has been mainly concentrated on a second theoretical pathway in answering the relevance question, which overcomes this issue. It is based on just the quantum mechanical model and the success quantifier. No other, for example classical, model is invoked. The actual model will contain dynamical processes that are quantum coherent and others that are incoherent. The non-trivial task is to deconstruct how the various processes contribute to the performance criterion. This can be done by decomposing the performance criterion into a sum of contributions, each associated with a particular process. The terms in this sum related to quantum mechanical processes will then give a theoretical answer to the overall relevance of the particular process and will quantify this relevance. This line of thought was developed and discussed in Ref. 26 for energy transfer in the FMO complex and provided insight into both questions "Is a quantum effect relevant?" and "If yes, how much?", at least from a theoretical standpoint within the approximations of the model under consideration. In this section, we extend this idea to include the effect of the initial conditions and compare the results to a total integrated coherence, or concurrence, measure. We utilize secular Redfield theory and the hierarchy equation of motion approach.

The Hamiltonian describing a single exciton is given by:

$$H_e = \sum_m (\epsilon_m + \lambda)|m\rangle\langle m| + \sum_{m<n} J_{mn} \left(|m\rangle\langle n| + |n\rangle\langle m|\right). \qquad (2.1)$$

where the site energies ϵ_m, and couplings J_{mn} are usually obtained from detailed quantum chemistry studies and/or fitting of experimental spectra. The reorganization energy λ, which we assume to be the same for each site, is the energy difference of the non-equilibrium phonon state after Franck-Condon excitation and the excited-state equilibrium phonon state. The set of states $|m\rangle$ is called the site basis and the set of states $|\alpha\rangle$ with $H_e|\alpha\rangle = E_\alpha|\alpha\rangle$ is called the exciton basis. We now briefly introduce the secular Redfield master equation in the weak exciton-phonon (or system-bath) coupling limit and the non-perturbative hierarchy equation of motion approach. In both approaches, the dynamics of a single exciton is governed by a master equation, which is schematically given by:

$$\frac{\partial}{\partial t}\rho(t) = \mathcal{M}\rho(t) = \left(\mathcal{M}_\mathrm{H} + \mathcal{M}_\mathrm{decoherence} + \mathcal{M}_\mathrm{trap} + \mathcal{M}_\mathrm{loss}\right)\rho(t). \qquad (2.2)$$

The master equation consists of the superoperator $\mathcal{M}$, which is divided into several components. First, coherent evolution with the excitonic Hamiltonian H_e is described by the superoperator $\mathcal{M}_\mathrm{H} = -i[H_e, \cdot]$. In addition, decoherence due to the interaction with the phonon bath is incorporated by $\mathcal{M}_\mathrm{decoherence}$. $\mathcal{M}_\mathrm{decoherence}$ depends on the spectral density, which models the coupling strengths of the phonon modes to the system. Finally, one has the processes for trapping to a reaction center $\mathcal{M}_\mathrm{trap}$ and exciton loss $\mathcal{M}_\mathrm{loss}$ due to spontaneous emission. Associated with these processes are the trapping rate κ and the loss rate Γ. Details about the trapping and exciton loss processes can be found in [26, 56].

The secular Redfield theory is valid in the regime of weak system-bath coupling. The superoperator $\mathcal{M}_\mathrm{decoherence}$ is of Lindblad form with Lindblad operators for relaxation in the exciton basis and for dephasing of excitonic superpositions. The

relaxation rates depend on the spectral density evaluated at the particular excitonic transition frequencies, satisfy detailed balance, and depend on temperature through the Bose-Einstein distribution. The dephasing rates are linear in temperature. We use the same Ohmic spectral density as in [29], i.e. $J(\omega) = 2\lambda\gamma\omega/\pi(\omega^2 + \gamma^2)$, where $1/\gamma$ is the bath correlation time. For $1/\gamma = 50$ fs, this spectral density shows only modest differences to the spectral density used in [26]. Further details about the Lindblad model can be found in [26].

The hierarchy equation of motion approach [29] consistently interpolates between weak and strong system bath coupling. The assumption that the fluctuations are Gaussian makes the second-order cumulant expansion exact. The resulting equation of motion can be expressed as an infinite hierarchy of system, i.e. $\rho(t)$, and connected auxiliary density operators $\{\sigma_i\}$, arranged in tiers. For numerical simulation, "far-away" tiers in the hierarchy are truncated in a sensible manner. The hierarchy equation of motion can also be written as in Eq. (2.2) when we make the replacement $\rho(t) \rightarrow (\rho(t), \sigma_1, \sigma_2, \cdots)$ and use the hierarchical structure discussed in [29] for the decoherence superoperator $\mathcal{M}_{\text{decoherence}}$. For simulations of the Fenna-Matthews-Olson complex, we use the scaled hierarchy approach developed in [57]. It was shown recently that four tiers of auxiliary density operators are enough for accurate room temperature simulations [58], which enables the rapid computation of efficiency and total coherences. The trapping and exciton loss processes are naturally extended to the auxiliary systems.

In our previous work [26], we developed a method to quantify the role of quantum coherence to the transfer efficiency. The energy transfer efficiency (ETE) is given by

the integrated probability of leaving the system from the sites that are connected to the trap instead to being lost to the environment. That is, $\eta = \int_0^\infty dt \mathrm{Tr}\{\mathcal{M}_{\mathrm{trap}}\rho(t)\}$. It was shown that the ETE can be partitioned into $\eta = \eta_{\mathrm{H}} + \eta_{\mathrm{decoherence}}$, where the efficiency due to the coherent dynamics with the excitonic Hamiltonian is given by:

$$\eta_{\mathrm{H}} = \mathrm{Tr}\{\mathcal{M}_{\mathrm{trap}}(\mathcal{M}_{\mathrm{trap}} + \mathcal{M}_{\mathrm{loss}})^{-1}\mathcal{M}_{\mathrm{H}}\mathcal{M}^{-1}\rho(0)\}. \tag{2.3}$$

The ETE contribution $\eta_{\mathrm{decoherence}}$ involves $\mathcal{M}_{\mathrm{decoherence}}$, i.e.,

$$\eta_{\mathrm{decoherence}} = \mathrm{Tr}\{\mathcal{M}_{\mathrm{trap}}(\mathcal{M}_{\mathrm{trap}} + \mathcal{M}_{\mathrm{loss}})^{-1}\mathcal{M}_{\mathrm{decoherence}}\mathcal{M}^{-1}\rho(0)\}.$$

In this work, we extend our ETE contribution method to quantify the role of the initial state to the ETE. We obtain a separation of the coherent contribution, $\eta_{\mathrm{H}} = \eta_{\mathrm{init}} + \eta_{\mathrm{dyn}}$, where the efficiency η_{init} can be ascribed to the initial state. The η_{dyn} is defined by $\eta_{\mathrm{dyn}} = \eta_{\mathrm{H}} - \eta_{\mathrm{init}}$ and can be interpreted as dynamical part of the coherence contribution arising during the time evolution. For the computation of η_{init}, we note that one can always express the ensemble described by the system density matrix as $\rho(t) = p_{\mathrm{init}}(t)|\psi_{\mathrm{init}}(t)\rangle\langle\psi_{\mathrm{init}}(t)| + \sum_k p_k(t)\rho_k(t)$. Here, $p_{\mathrm{init}}(t)$ is the probability of the quantum system being in the (Hamiltonian time-evolved) initial state $|\psi_{\mathrm{init}}(t)\rangle$, where $p_{\mathrm{init}}(0) = 1$. The $p_k(t)$ are the probabilities of being in some other ensemble state $\rho_k(t)$, where $p_{\mathrm{init}}(t) + \sum_k p_k(t) = 1$. The probability $p_{\mathrm{init}}(t)$ is reduced by the interaction with the environment and readily computed for Markovian Lindblad dynamics by considering the damped no-jump evolution due to the decoherence superoperator $\mathcal{M}_{\mathrm{decoherence}}$ [56, 59, 60]. Therefore, we can compute the efficiency pertaining to the initial state by $\eta_{\mathrm{init}} = \int_0^\infty dt \mathrm{Tr}\{\mathcal{M}_{\mathrm{trap}}p_{\mathrm{init}}(t)|\psi_{\mathrm{init}}(t)\rangle\langle\psi_{\mathrm{init}}(t)|\}$. Together with Equation (2.3), this obtains the desired separation $\eta_{\mathrm{H}} = \eta_{\mathrm{init}} + \eta_{\mathrm{dyn}}$.

Additionally, we employ another measure for the role of coherence by straightfor-

wardly integrating over time all the coherence elements of the density matrix. That

is:

$$C(\lambda) = \sum_{m \neq n} \int_0^\infty dt \; |\langle m| \rho(t) |n\rangle|. \tag{2.4}$$

We normalize with respect to the case of coherent evolution at $\lambda = 0.0/$cm, i.e.

$\tilde{C}(\lambda) = C(\lambda)/C(0)$. Based on the discussion in [52], the quantity $\tilde{C}$ can be considered

as the (normalized) integrated entanglement (concurrence) that is present before the

exciton is trapped in the reaction center or lost to the environment. We note that the

total coherence measure $\tilde{C}$ is similar in spirit to a measure of the first kind discussed

above. This is because the normalization essentially performs a comparison of the

actual model at a certain λ with an artificial model at $\lambda = 0$. (For the numerical

evalutation, the integral in Eq. (2.4) is computed until $\text{Tr}\{\rho(t)\} \leq 10^{-3}$.)

Figure 2.1: (Left panel) Efficiency η (solid black) and contributions of initial state η_{init} (dash-dotted gray) and coherent evolution $\eta_{\text{init}} + \eta_{\text{dyn}}$ (dashed red) for a dimer that is based on the strongly coupled sites 1 and 2 of the Fenna-Matthews-Olson complex using the secular Redfield model. The initial state is at site 1 and the target is site 2. At a physiological value of around $\lambda = 35/$cm, one finds $\eta_{\text{init}} = 0.0$ and $\eta_{\text{dyn}} = 0.43$. (Center panel) Efficiency and integrated coherence $\tilde{C}$ for the dimer with the secular Redfield approach. At $\lambda = 35/$cm there is $\tilde{C} = 0.37$. (Right panel) Same quantities as in the center panel for the dimer using the hierarchy equation of motion approach with 15 tiers of auxiliary systems. At $\lambda = 35/$cm, one finds $\tilde{C} = 0.44$. The parameters are $1/\kappa = 1$ ps, $1/\Gamma = 1$ ns, and $1/\gamma = 50$ fs for all panels.
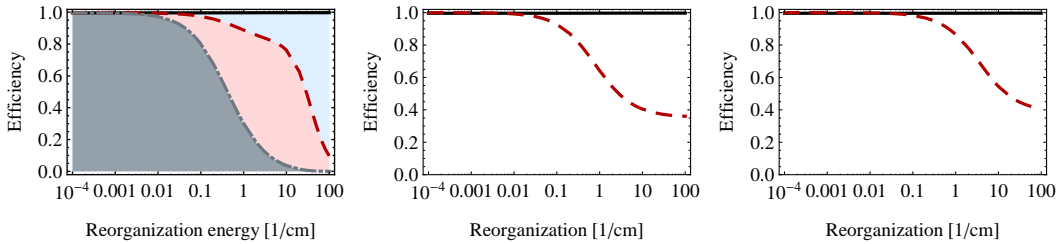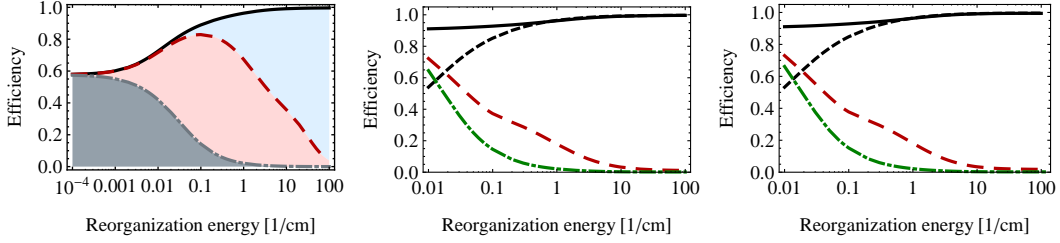
Figure 2.2: (Left panel) Efficiency η (solid black) and contributions of initial state η_{init} (dash-dotted gray) and coherent evolution $\eta_{\text{init}} + \eta_{\text{dyn}}$ (dashed red) for the Fenna-Matthews-Olson complex using the secular Redfield model. The initial state is a classical mixture of site 1 and 6 and the target site for trapping is site 3. The actual system has a reorganization energy of around $\lambda = 35/\text{cm}$, where $\eta_{\text{init}} = 0.0$ and $\eta_{\text{dyn}} = 0.17$. (Center panel) Efficiency for initial site 1 (solid black) and initial site 6 (dashed black) and integrated coherence $\tilde{C}$ for initial site 1 (dashed red) and initial site 6 (dash-dotted green) for the Fenna-Matthews-Olson complex with the secular Redfield approach. At $\lambda = 35/\text{cm}$ there is $\tilde{C} = 0.0151$ (inital site 1) and $\tilde{C} = 0.0017$ (initial site 6). (Right panel) Same quantities as in the center panel for the FMO complex using the scaled hierarchy equation of motion approach with four tiers of auxiliary systems. At $\lambda = 35/\text{cm}$, one finds $\tilde{C} = 0.020$ (inital site 1) and $\tilde{C} = 0.0022$ (initial site 6). The parameters are $1/\kappa = 1$ ps, $1/\Gamma = 1$ ns, and $1/\gamma = 50$ fs for all plots.

In Fig. 2.1, we present the two measures of coherence for a dimer system. For the dimer, we take the sites 1 and 2 of the FMO complex with $\epsilon_1 = 0/\text{cm}$, $\epsilon_2 = 120/\text{cm}$, and $J = -87.7/\text{cm}$, see [14], and room temperature. This system will also be the focus of the following sections on the atomistic detail simulations and quantum process tomography. Here, for studying the role of quantum coherence, we assume that the task is defined by the exciton initially being at the lower energy site 1 and the target site being site 2. In the left panel of Fig. 2.1 we show the efficiency η, the contribution η_H from Eq. (2.3), and η_init for the secular Redfield model. In the present small system, environment-assisted transport is relatively unimportant, with the efficiency as a function of the reorganziation energy being close to unity everywhere. The underlying contributions show a transition from a regime dominated by coherent evolution to a regime dominated by incoherent Lindblad jumps. At $\lambda = 35/\text{cm}$, we find $\eta_\text{init} = 0\%$ and $\eta_\text{H} = 43\%$. In Fig. 2.1 (center panel), we find that the total coherence measure $\tilde{C}$ for the dimer is around 0.37 for $\lambda = 35/\text{cm}$. In Fig. 2.1 (right panel), the total coherence is plotted for the dimer in the hierarchy equation of motion approach. We use 15 tiers of auxiliary systems. At $\lambda = 35/\text{cm}$, we find $\tilde{C} = 0.44$; because of the sluggish, non-equilibrium bath there is more coherence than in the secular Redfield model.

In Fig. 2.2 (left panel), we present the coherent, decoherent, and initial state contribution to the ETE for the Fenna-Matthews-Olson complex as a function of the reorganization energy for the secular Redfield model at room temperature. We use the Hamiltonian given in [14] and the contribution measures given in Equation (2.3) and by η_init. The initial state is a classical mixture of site 1 and 6. For small

reorganization energy, the efficiency is around $\eta = 60\%$ and for larger reorganization energies we observe environment-assisted quantum transport (ENAQT) [27], with the efficiency rising up to almost $\eta = 100\%$ for the physiological value of $\lambda = 35/\text{cm}$. The contributions measures η_{dyn} and η_{init} reveal the underlying dynamics. The quantum dynamical contribution η_{dyn} is around 17% at $\lambda = 35/\text{cm}$ [1]. In our model, this part is due to an interplay of the Hamiltonian dynamics and the trapping/loss dynamics, which both have their preferred basis being the site basis. The main part of the efficiency at $\lambda = 35/\text{cm}$ is due to incoherent Lindblad jumps, having a value of $\eta_{\text{decoherence}} = 83\%$. The initial state contribution is relevant only at small values of the reorganization energy.

In Fig. 2.2 (center and right panel), we compare the efficiency and the coherence measure $\tilde{C}$ for the secular Redfield and the hierarchy equation of motion approach [29] for the Fenna-Matthews-Olson complex. The initial state is either localized at site 1 or at site 6. Four tiers of auxiliary systems were used in the computation, which already lead to a good agreement with [29] for the dynamics at $\lambda = 35\text{cm}^{-1}$, $1/\gamma = 50$ fs, and room temperature. In Fig. 2.2 (right panel), ENAQT is observed with increasing reorganization energy also in the hierarchy approach, with the efficiency rising up to almost $\eta = 100\%$ at $\lambda = 35/\text{cm}$. In Fig. 2.2 (center and right panel), it is observed that the normalized total coherences of the density matrix decrease with increasing reorganization energy. For the secular Redfield case, we obtain $\tilde{C}(\lambda = 35\text{cm}^{-1}) = 0.0151$ for the initial site 1 and $\tilde{C}(\lambda = 35\text{cm}^{-1}) = 0.0017$ for the initial site 6. For the hierarchy case, we obtain more coherence, i.e. $\tilde{C}(\lambda = 35\text{cm}^{-1}) = 0.020$ for the initial

---

[1]In Ref. 26, we found the value $\eta_{\text{H}} = 10\%$ for a different Hamiltonian and a different spectral density.

site 1 and $\tilde{C}(\lambda = 35\text{cm}^{-1}) = 0.0022$ for the initial site 6. In both models, coherence is more important for the rugged energy landscape of the pathway from site 1 than for the funnel-type energy landscape of the pathway from site 6.

Master equation approaches, such as the ones discussed in this section suffer from various drawbacks. Redfield theory is only applicable in the limit of weak system bath coupling and does not take into account non-equilibrium molecular reorganization effects. The hierarchy equation of motion approach assumes Gaussian fluctuations and Ohmic Drude-Lorentz spectral densities. The detailed atomistic structure of the protein and the chlorophylls is not taken into account in these approaches. The results thus provide a general indication of the behavior of the actual system but not a conclusive and detailed theoretical proof. In the next section, we will present a first step toward such a detailed study with our combined molecular dynamics/quantum chemistry method. The atomistic structure is included and realistic spectral densities can be obtained. We also present a straightforward method to simulate exciton dynamics beyond master equations. We thus address the second question of the microscopic origins of the long-lived quantum coherence.

2.3   Molecular Dynamics Simulations

Among many other biologically functional components, protein complexes are essential components of the photosynthetic system. Proteins remain as one of the main topics of biophysical research due to their diverse and unidentified structure-function relationship. Many biological units are highly optimized and efficient, so that even a point mutation of a single amino acid in conserved region often results in the

loss of the functionality [61–63]. Have the photosynthetic system adopted quantum mechanics to improve its efficiency in its course of evolution? To answer this question, careful characterization of the protein environment to the atomistic detail is necessary to identify the microscopic origin of the long-lived quantum coherence. As explained in the previous section, the contribution of the quantum coherence to the energy transfer efficiency in biological systems have been successfully carried out, yet a more detailed description of the bath in atomic detail would be desirable to investigate the structure-function relationship of the protein complex and to test validity of the assumptions used in popular models of the photosynthetic system.

The site energy of a chromophore is a complex function of the configuration of the chromophore molecule, and the relative orientation of the molecule to that of the embedding protein and that of other chromophore molecules. Factors affecting site energies have intractably large degrees of freedom, so it is reasonable to treat those degrees of freedom as the bath of an open quantum system. The state of the system is assumed to be restricted to the single exciton manifold. To construct a system-bath relationship with atomistic detail of the bath, we start from the total Hamiltonian operator, and decomposed the operator in such a way that the system-bath Hamiltonian is not assumed to be any specific functional form:

$$H_{total} = \sum_m \epsilon_m(\boldsymbol{R}_{ch}, \boldsymbol{R}_{prot})|m\rangle\langle m| + \sum_{m,n} \{J_{mn}(\boldsymbol{R}_{ch}, \boldsymbol{R}_{prot})|m\rangle\langle n| + c.c.\}$$

$$+ T_{ch} + T_{prot} + V_{ch}(\boldsymbol{\sigma}, \boldsymbol{R}_{ch}, \boldsymbol{R}_{prot}) + V_{prot}(\boldsymbol{R}_{ch}, \boldsymbol{R}_{prot}). \tag{2.5}$$

ϵ_m represents the site energy of mth site, J_{mn} is the coupling constant between mth and nth sites. $\boldsymbol{\sigma}$ denotes the excitonic state of chromophores, $\boldsymbol{R}_{ch}$ corresponds to the

nuclear coordinates of chromophore molecules, and $\boldsymbol{R}_{prot}$ are the nuclear coordinates of the remaining protein and enclosing water molecules. T and V are the corresponding kinetic and potential energy operators for the chromophores and proteins respectively under Born-Oppenheimer approximation. The potential energy term for chromophores depends on the exciton state of the systen, because dynamics of a molecule will be governed by different Born-Oppenheimer surface when its excitonic state changes. However, as a first approximation, we assumed that the change of Born-Oppenheimer surfaces does not affect the bath dynamics significantly. With this assumption, we can ignore the dependence of the excitonic state in the V_{ch} term and the system-bath Hamiltonian only contains the one way influence from the bath to the system:

$$
\begin{aligned}
H_{total} \approx &\sum_m \epsilon_m(\boldsymbol{R}_{ch}, \boldsymbol{R}_{prot})|m\rangle\langle m| + \sum_{m,n} J_{mn}(\boldsymbol{R}_{ch}, \boldsymbol{R}_{prot})|m\rangle\langle n| \\
&+ \sum_m \epsilon_m(\boldsymbol{R}_{ch}, \boldsymbol{R}_{prot})|m\rangle\langle m| + T_{ch} + T_{prot} + V_{ch}(\boldsymbol{R}_{ch}, \boldsymbol{R}_{prot}) + V_{prot}(\boldsymbol{R}_{ch}, \boldsymbol{R}_{prot}) \\
= &\underbrace{\sum_m \bar{\epsilon}_m|m\rangle\langle m| + \sum_{m,n} \bar{J}_{mn}|m\rangle\langle n|}_{H_S} \\
&+ \underbrace{\sum_m \left\{\epsilon_m(\boldsymbol{R}_{ch}, \boldsymbol{R}_{prot}) - \bar{\epsilon}_m\right\}|m\rangle\langle m| + \sum_{m,n} \left\{J_{mn}(\boldsymbol{R}_{ch}, \boldsymbol{R}_{prot}) - \bar{J}_{mn}\right\}|m\rangle\langle n|}_{H_{SB}} \\
&+ \underbrace{T_{ch} + T_{prot} + V_{ch}(\boldsymbol{R}_{ch}, \boldsymbol{R}_{prot}) + V_{prot}(\boldsymbol{R}_{ch}, \boldsymbol{R}_{prot})}_{H_B}.
\end{aligned}
\tag{2.6}
$$

Based on this decomposition of the total Hamiltonian, we set up a model of the FMO complex in atomistic detail with the AMBER force field [64, 65] and approximate the propagation of the entire complex by classical mechanics. Molecular dynamics simulations were conducted at 77K and 300K with an isothermal-isobaric (NPT)

ensemble. The parameters for the system and the system-bath Hamiltonian were calculated using quantum chemistry methods along the trajectory from the molecular dynamics simulation. ϵ_m was calculated using the Q-Chem quantum chemistry package [66]. The electronic excitations were modeled using the time-dependent density functional theory using the Tamm-Dancoff approximation. The density functional employed was BLYP and the basis set employed was 3-21G*. External charges from the force field were included in the calculation as the electrostatic external potential. The coupling terms, J_{mn}, were obtained from the Hamiltonian presented in Ref. 14 and considered to be constant in time. $\bar{\epsilon}_m$ was chosen as time averaged site energy for the mth site to minimize the magnitude of the system-bath Hamiltonian. In this work, only site 1 and site 2 were considered for the exciton dynamics. However, the methodology can be applied for the exciton dynamic of all seven chromophores.

To obtain a closed-form equation for the reduced density matrix, we applied mean-field approximation [67]; because no feedback from the system to the bath was assumed, the state of the bath is not affected by the state of the system. Therefore, the total density matrix, $W(t)$, can be factorized into the reduced density matrix $\rho(t)$, and $B(t)$ which is defined only in the Hilbert space of the bath. With additional assumption that the bath is in thermal equilibrium, we can obtain the closed equation for the reduced density matrix.

$$
\begin{aligned}
\frac{\partial}{\partial t}\rho(t) &= -\frac{i}{\hbar}\left[H_S, \rho(t)\right] - \frac{i}{\hbar}\mathrm{Tr}\left\{\left[H_{SB}, W(t)\right]\right\} \\
&\approx -\frac{i}{\hbar}\left[H_S, \rho(t)\right] - \frac{i}{\hbar}\left[\mathrm{Tr}\left\{H_{SB}B(t)\right\}, \rho(t)\right] \\
&\approx -\frac{i}{\hbar}\left[H_S, \rho(t)\right] - \frac{i}{\hbar}\left[\mathrm{Tr}\left\{H_{SB}B_{eq}(t)\right\}, \rho(t)\right].
\end{aligned}
\tag{2.7}
$$

Thermal equilibrium of the bath was ensured by the thermostat of the molecular
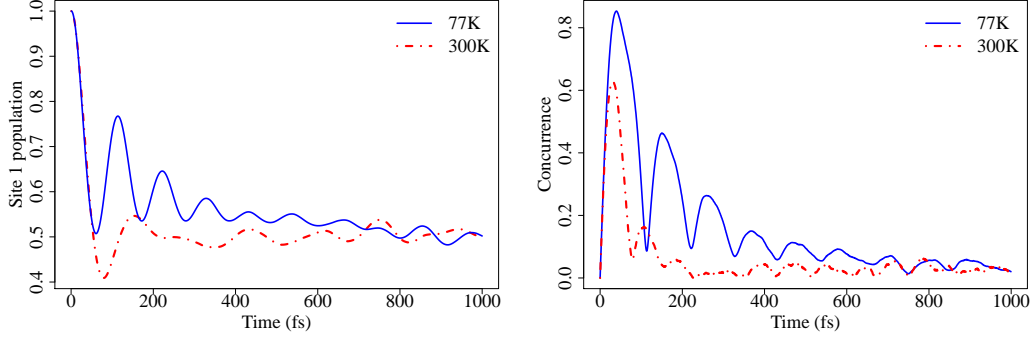
Figure 2.3: (Left panel) Time evolution of the exciton population at the site 1 (ρ_{11}) based on the strongly coupled site 1 and 2 of the FMO complex at 77K and 300K. The initial pure state $\rho = |1\rangle\langle 1|$ was propagated using Monte Carlo integration of unitary evolutions, where the time-dependent site energies are obtained from a combined molecular dyanmics/quantum chemistry approach. The asymptotic distribution does not follow a Boltzmann distribution because relaxation of the system to the bath is not considered. (Right panel) The concurrence between site 1 and 2 at 77K and 300K. Quantum coherence lives longer at a lower temperature.

dynamics simulation. Thus, the reduced density matrix was obtained by Monte Carlo integration of 4000 independent instances of unitary quantum evolution with respect to the thermally equilibrated bath. Each instance was propagated by integrating the Schrödinger equation with the simple exponential integrator.

Fig. 2.3 shows the change of the population of the site 1, ρ_{11}, and the concurrence between site 1 and 2. The population is evenly distributed between the two sites because relaxation was not considered. The concurrence, $2|\rho_{12}|$, is an indicator of pairwise entanglement for the system [52]. Note that the coherence builds up during the first ~ 100 fs , and then decreases subsequently due to the decoherence from the bath.

Fig. 2.4 shows the spectral density of the first chromophore. Although the spectral density of the bath from molecular dynamics simulation shows characteristic frequen-
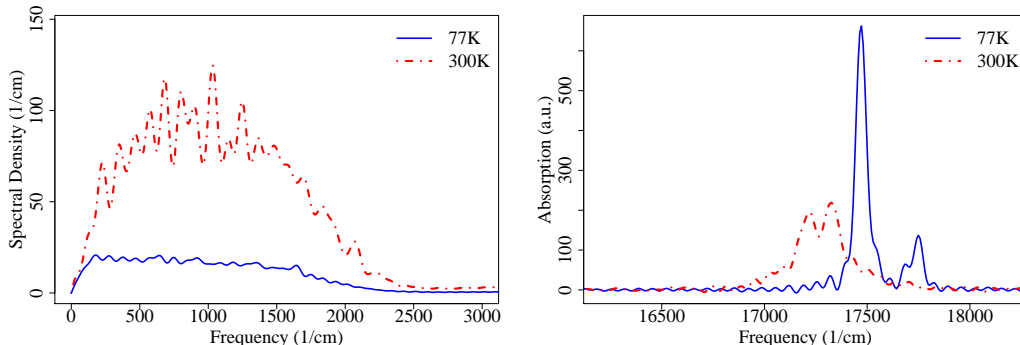
Figure 2.4: (Left panel) Spectral density from the autocorrelation function of the site 1 of the FMO complex from the molecular dynamics simulation at 77K and 300K. While the spectral density reflects the characteristic vibrational modes of the protein and the chromophore molecule, high-frequency modes are overpopulated due to the limitation of the Newtonian mechanics. (Right panel) Absorption spectrum of site 1 and 2 at 77K and 300K.

cies related to the actual protein environment and the bacteriochloropyll molecule, high-frequency modes are overpopulated due to the limitation of the classical mechanics. There are efforts to incorporate quantum effects into the classical molecular dynamics simulation in a slightly different context [68–70], and we are investigating the possibilities of applying these corrections.

Another simplification employed was the omission of the feedback from exciton states. When the exciton state of a bacteriochlorophyll is changed, the Born-Oppenheimer surface which governs the dynamics of the chromophore molecule should be also changed. The current scheme only propagates the protein complex on the electronically ground-state surface. Incorporating the feedback could lead to the different characteristics of the protein bath. There exist several schemes for mixed quantum-classical dynamics [71–73] which potentially resolve the problem at the additional computational cost of simultaneously propagating excitons and protein bath.

Calculations are underway to carry out the full seven-site simulation of the FMO complex at different temperatures to compare with experimental temperature-dependent results [25].

In the following final section, we will describe our quantum process tomography scheme, which is a spectroscopic technique associated with a computational procedure for direct extraction of the parameters related to the quantum evolution of the system, in terms of *quantum process maps*.

2.4   Quantum Process Tomography

So far, we have delved into several theoretical models to characterize quantum coherence in the entire FMO complex and in a dimer subsystem of it. Experimentally, however, a clear characterization of this coherence is still elusive. Signatures of long lived quantum superpositions between excitonic states in multichromophoric systems are potentially monitored through four wave-mixing techniques [23, 74, 75]. However, a transparent description of the evolving quantum state of the probed system is not necessarily obtained from a single realization of such experiments. In these, a series of three weak incoming ultrashort pulses sent from a noncollinear setup induce a macroscopic third order polarization in the sample. The latter manifests in a time dependent spatial grating which emits a macroscopic polarization that interferes with a fourth pulse, called the local oscillator. From an operational standpoint, this last pulse selects the spatial Fourier component of the polarization which corresponds to its wavevector (heterodyne detection), hence earning the name of four wave-mixing for this technique (FWM) [75]. Extracting specific Fourier components of the induced

polarization allows for the selection of a particular set of processes in the density matrix of the probed system, as each wavevector is associated with a carrier frequency of the pulse. These processes can be intuitively understood by keeping track of the dual Feynman diagrams that account for the perturbations that the pulses induce on the bra or ket sides of the density matrix of the probed system. Whereas the analysis of these experiments is naturally carried out in the density matrix formalism, an important question is whether the density matrix itself can be imaged via these experiments, a problem known as quantum state tomography (QST) [76]. If this were possible, quantum process tomography (QPT) could also be carried out, therefore providing a complete characterization of excited state dynamics [77]. In a previous study, we showed that a series of two-color heterodyned rephasing photon-echo (PE) experiments repeated in different polarization configurations yields the necessary information to carry out QST and QPT of the single-exciton manifold of a coupled heterodimer [78]. In the present article, we adapt our previous theory to extract this information from two-dimensional spectra, similar to those employed in current experiments. An comprehensive study of this possibility has been presented in [79]. Here, we shall highlight some key features of the method.

We begin by reviewing some basic aspects of QPT. Under very general assumptions, the evolution of an open quantum system can be described by a linear transformation [80]:

$$\rho_{ab}(T) = \sum_{cd} \chi_{abcd}(T)\rho_{cd}(0), \tag{2.8}$$

where $\rho_{ab}(T)$ is the element ab of the reduced density matrix ρ of the system at time T. Equation (2.8) is remarkable in that $\chi(T)$ is independent of the initial

state. Knowledge of $\chi(T)$ implies a complete characterization of the dynamics of the reduced system and, in fact, QPT can be operationally defined as the procedure to obtain $\chi(T)$. Conceptually, it is straightforward to recognize that, due to linearity, $\chi(T)$ can be inverted by preparing a complete set of inputs, evolving them for time T, and detecting the outputs along a complete basis. In the context of nonlinear optical spectroscopy, this is exactly the strategy we shall follow, with a few caveats due to experimental constraints.

To place the discussion in context, we shall be again concerned with the subsystem composed of the excitonic dimer between sites 1 and 2 of the FMO complex. For simplicity, we ignore the rest of the sites in this theoretical study. We only need to be concerned with four eigenstates of this model system: The ground state $|g\rangle$, the delocalized single-excitons $|\alpha\rangle$ and $|\beta\rangle$, and the biexciton $|f\rangle$, which in the photosynthetic system can be safely assumed to be the direct sum of the single-excitons without significant interactions between them. Therefore, the biexciton energy level is just $\omega_f = \omega_\alpha + \omega_\beta$. We label the delocalized excitons so that $|\alpha\rangle$ is the higher energy eigenstate compared to $|\beta\rangle$. Denoting the transition energies between the i-th and the j-th states by $\omega_{ij} = \omega_i - \omega_j$, it follows that $\omega_{\alpha g} = \omega_{f\beta}$ and $\omega_{\beta g} = \omega_{f\alpha}$ [81]. The excitonic system is not isolated, and in fact, it interacts with a phonon and photon bath which induces relaxation and dephasing processes in it.

The experimental technique we consider is photon-echo (PE) spectroscopy, which is a particular subset of FWM techniques where the wavevector of the fourth pulse corresponds to the phase-matching condition $\boldsymbol{k}_{PE} = -\boldsymbol{k_1} + \boldsymbol{k_2} + \boldsymbol{k_3}$, with $\boldsymbol{k}_i$ being the wavevector corresponding to the i-th pulse. Here, the labeling of the pulses cor-

responds to the order in which the fields interact with the sample. Typically, the ultrashort pulses employed to study these excitonic systems possess an optical carrier frequency, therefore allowing transitions which are resonant with the frequency components $\pm\omega_{\beta g}$ and $\pm\omega_{\alpha g}$. In PE experiments, the first pulse centered at t_1 creates an optical coherence beating at a frequency $\omega_{g\alpha}$ or $\omega_{g\beta}$. At $t_2 = t_1 + \tau$, the second pulse creates a coherence or a population in the single exciton manifold. At $t_3 = t_2 + T$, the third pulse generates another optical coherence, but this time, beating at the frequencies opposite to the ones in the first interval, that is, at frequencies $\omega_{\alpha g}$ or $\omega_{\beta g}$, causing a rephasing echo of the signal. The heterodyne detection of the nonlinear polarization signal $P_{PE}(\tau, T, t)$ occurs at time $t_4 = t_3 + t$. Borrowing from NMR jargon, the intervals (t_1, t_2), (t_2, t_3), and (t_3, t_4) are traditionally refered to as *coherence*, *waiting*, and *echo* times, and their durations are τ, T, and t, respectively. This nomenclature should not be taken literally. For example, in most cases, coherences do not only evolve in the coherence time, but in the waiting and echo times. Similarly, the waiting time is often referred to as population time, which hosts dynamics of both populations and coherences. For a historical perspective on this vocabulary, we refer the reader to any comprehensive NMR treatise such as [82].

The experiment is systematically repeated for many durations for each interval. In order to 'watch' single-exciton dynamics, it is convenient to isolate the changes on the signal due to the waiting time T. This exercise is accomplished by performing a double Fourier transform of the signal along the τ and t axes, which yields a 2D spectra that evolves in T [83–85]:

$$S(\omega_\tau, T, \omega_T) = \int_0^\infty d\tau \int_0^\infty dt P_{PE}(\tau, T, t) e^{-i\omega_\tau \tau + i\omega_T T} \tag{2.9}$$

In order to map a PE experiment to a QPT, we identify the coherence interval as the preparation step and the echo interval as the detection step. This assumption implies that the optical coherence intervals have well characterized dynamics. This hypothesis is reasonable due to a separation of timescales where optical coherences will presumably decay exponentially due to pure dephasing and not due to intricate phonon-induced processes. Therefore, the 2D spectrum consists of four Lorentzian peaks centered about $(\omega_\tau, \omega_t) = (\omega_{\alpha g}, \omega_{\alpha g}), (\omega_{\alpha g}, \omega_{\beta g}), (\omega_{\beta g}, \omega_{\alpha g}), (\omega_{\beta g}, \omega_{\beta g})$. In this discussion, we shall ignore inhomogeneous broadening, noting that it can always be accounted for as a convolution of the signal with the distribution of inhomogeneity. The width of these Lorentzians can be directly related to the dephasing rates of the optical coherences. Loosely speaking, a particular value on the ω_τ axis of the spectrum indicates a specific type of state preparation, whereas the ω_t axis is related to a particular detection. More precisely, a peak in the 2D spectrum displays the correlations between the frequency beats from the coherence and echo intervals. A crucial realization is that the amplitude of these peaks can be written as a linear combination of elements of the time evolving excitonic density matrix stemming from

different initial states, that is, of elements of $\chi(T)$ itself [79]:

$$
\begin{aligned}
\tilde{S}(\omega_{\alpha g}, T, \omega_{\alpha g}) &= -C^\alpha_{\omega_1} C^\alpha_{\omega_2} (\boldsymbol{\mu}_{\alpha g} \cdot \boldsymbol{e}_1)(\boldsymbol{\mu}_{\alpha g} \cdot \boldsymbol{e}_2) \\
&\times \{ C^\alpha_{\omega_3} [(\boldsymbol{\mu}_{\alpha g} \cdot \boldsymbol{e}_3)(\boldsymbol{\mu}_{\alpha g} \cdot \boldsymbol{e}_4)(\chi_{gg\alpha\alpha}(T) - 1 - \chi_{\alpha\alpha\alpha\alpha}(T)) \\
&+ (\boldsymbol{\mu}_{f\beta} \cdot \boldsymbol{e}_3)(\boldsymbol{\mu}_{f\beta} \cdot \boldsymbol{e}_4)\chi_{\beta\beta\alpha\alpha}(T)] \\
&+ C^\beta_{\omega_3} [(\boldsymbol{\mu}_{f\alpha} \cdot \boldsymbol{e}_3)(\boldsymbol{\mu}_{f\beta} \cdot \boldsymbol{e}_4) - (\boldsymbol{\mu}_{\beta g} \cdot \boldsymbol{e}_3)(\boldsymbol{\mu}_{\alpha g} \cdot \boldsymbol{e}_4))\chi_{\alpha\beta\alpha\alpha}(T)]\} \\
&- C^\alpha_{\omega_1} C^\beta_{\omega_2} (\boldsymbol{\mu}_{\alpha g} \cdot \boldsymbol{e}_1)(\boldsymbol{\mu}_{\beta g} \cdot \boldsymbol{e}_2) \\
&\times \{ C^\alpha_{\omega_3} [(\boldsymbol{\mu}_{\alpha g} \cdot \boldsymbol{e}_3)(\boldsymbol{\mu}_{\alpha g} \cdot \boldsymbol{e}_4)(\chi_{gg\beta\alpha}(T) - \chi_{\alpha\alpha\beta\alpha}(T)) \\
&+ (\boldsymbol{\mu}_{f\beta} \cdot \boldsymbol{e}_3)(\boldsymbol{\mu}_{f\beta} \cdot \boldsymbol{e}_4)\chi_{\beta\beta\beta\alpha}(T)] \\
&+ C^\beta_{\omega_3} [((\boldsymbol{\mu}_{f\alpha} \cdot \boldsymbol{e}_3)(\boldsymbol{\mu}_{f\beta} \cdot \boldsymbol{e}_4) - (\boldsymbol{\mu}_{\beta g} \cdot \boldsymbol{e}_3)(\boldsymbol{\mu}_{\alpha g} \cdot \boldsymbol{e}_4))\chi_{\alpha\beta\beta\alpha}(T)]\},
\end{aligned}
$$

$$ (2.10) $$

$$
\begin{aligned}
\tilde{S}(\omega_{\alpha g}, T, \omega_{\beta g}) &= -C^\alpha_{\omega_1} C^\alpha_{\omega_2} (\boldsymbol{\mu}_{\alpha g} \cdot \boldsymbol{e}_1)(\boldsymbol{\mu}_{\alpha g} \cdot \boldsymbol{e}_2) \\
&\times \{ C^\beta_{\omega_3} [(\boldsymbol{\mu}_{\beta g} \cdot \boldsymbol{e}_3)(\boldsymbol{\mu}_{\beta g} \cdot \boldsymbol{e}_4)(\chi_{gg\alpha\alpha}(T) - 1 - \chi_{\beta\beta\alpha\alpha}(T)) \\
&+ (\boldsymbol{\mu}_{f\alpha} \cdot \boldsymbol{e}_3)(\boldsymbol{\mu}_{f\alpha} \cdot \boldsymbol{e}_4)\chi_{\alpha\alpha\alpha\alpha}(T)] \\
&+ C^\alpha_{\omega_3} [((\boldsymbol{\mu}_{f\beta} \cdot \boldsymbol{e}_3)(\boldsymbol{\mu}_{f\alpha} \cdot \boldsymbol{e}_4) - (\boldsymbol{\mu}_{\alpha g} \cdot \boldsymbol{e}_3)(\boldsymbol{\mu}_{\beta g} \cdot \boldsymbol{e}_4))\chi_{\beta\alpha\alpha\alpha}(T)]\} \\
&- C^\alpha_{\omega_1} C^\beta_{\omega_2} (\boldsymbol{\mu}_{\alpha g} \cdot \boldsymbol{e}_1)(\boldsymbol{\mu}_{\beta g} \cdot \boldsymbol{e}_2) \\
&\times \{ C^\beta_{\omega_3} [(\boldsymbol{\mu}_{\beta g} \cdot \boldsymbol{e}_3)(\boldsymbol{\mu}_{\beta g} \cdot \boldsymbol{e}_4)(\chi_{gg\beta\alpha}(T) - \chi_{\beta\beta\beta\alpha}(T)) \\
&+ (\boldsymbol{\mu}_{f\alpha} \cdot \boldsymbol{e}_3)(\boldsymbol{\mu}_{f\alpha} \cdot \boldsymbol{e}_4)\chi_{\alpha\alpha\beta\alpha}(T)] \\
&+ C^\alpha_{\omega_3} [((\boldsymbol{\mu}_{f\beta} \cdot \boldsymbol{e}_3)(\boldsymbol{\mu}_{f\alpha} \cdot \boldsymbol{e}_4) - (\boldsymbol{\mu}_{\alpha g} \cdot \boldsymbol{e}_3)(\boldsymbol{\mu}_{\beta g} \cdot \boldsymbol{e}_4))\chi_{\beta\alpha\beta\alpha}(T)]\},
\end{aligned}
$$

$$ (2.11) $$

49

$$\tilde{S}(\omega_{\beta g}, T, \omega_{\alpha g}) = -C_{\omega_1}^{\beta} C_{\omega_2}^{\beta} (\boldsymbol{\mu}_{\beta g} \cdot \boldsymbol{e}_1)(\boldsymbol{\mu}_{\beta g} \cdot \boldsymbol{e}_2)$$

$$\times \{ C_{\omega_3}^{\alpha} [(\boldsymbol{\mu}_{\alpha g} \cdot \boldsymbol{e}_3)(\boldsymbol{\mu}_{\alpha g} \cdot \boldsymbol{e}_4)(\chi_{gg\beta\beta}(T) - 1 - \chi_{\alpha\alpha\beta\beta}(T))$$

$$+ (\boldsymbol{\mu}_{f\beta} \cdot \boldsymbol{e}_3)(\boldsymbol{\mu}_{f\beta} \cdot \boldsymbol{e}_4)\chi_{\beta\beta\beta\beta}(T)]$$

$$+ C_{\omega_3}^{\beta} [(\boldsymbol{\mu}_{f\alpha} \cdot \boldsymbol{e}_3)(\boldsymbol{\mu}_{f\beta} \cdot \boldsymbol{e}_4) - (\boldsymbol{\mu}_{\beta g} \cdot \boldsymbol{e}_3)(\boldsymbol{\mu}_{\alpha g} \cdot \boldsymbol{e}_4))\chi_{\alpha\beta\beta\beta}(T)]\}$$

$$- C_{\omega_1}^{\beta} C_{\omega_2}^{\alpha} (\boldsymbol{\mu}_{\beta g} \cdot \boldsymbol{e}_1)(\boldsymbol{\mu}_{\alpha g} \cdot \boldsymbol{e}_2)$$

$$\times \{ C_{\omega_3}^{\alpha} [(\boldsymbol{\mu}_{\alpha g} \cdot \boldsymbol{e}_3)(\boldsymbol{\mu}_{\alpha g} \cdot \boldsymbol{e}_4)(\chi_{gg\alpha\beta}(T) - \chi_{\alpha\alpha\alpha\beta}(T))$$

$$+ (\boldsymbol{\mu}_{f\beta} \cdot \boldsymbol{e}_3)(\boldsymbol{\mu}_{f\beta} \cdot \boldsymbol{e}_4)\chi_{\beta\beta\alpha\beta}(T)]$$

$$+ C_{\omega_3}^{\beta} [((\boldsymbol{\mu}_{f\alpha} \cdot \boldsymbol{e}_3)(\boldsymbol{\mu}_{f\beta} \cdot \boldsymbol{e}_4) - (\boldsymbol{\mu}_{\beta g} \cdot \boldsymbol{e}_3)(\boldsymbol{\mu}_{\alpha g} \cdot \boldsymbol{e}_4))\chi_{\alpha\beta\alpha\beta}(T)]\},$$

$$(2.12)$$

$$\tilde{S}(\omega_{\beta g}, T, \omega_{\beta g}) = -C_{\omega_1}^{\beta} C_{\omega_2}^{\beta} (\boldsymbol{\mu}_{\beta g} \cdot \boldsymbol{e}_1)(\boldsymbol{\mu}_{\beta g} \cdot \boldsymbol{e}_2)$$

$$\times \{ C_{\omega_3}^{\beta} [(\boldsymbol{\mu}_{\beta g} \cdot \boldsymbol{e}_3)(\boldsymbol{\mu}_{\beta g} \cdot \boldsymbol{e}_4)(\chi_{gg\beta\beta}(T) - 1 - \chi_{\beta\beta\beta\beta}(T))$$

$$+ (\boldsymbol{\mu}_{f\alpha} \cdot \boldsymbol{e}_3)(\boldsymbol{\mu}_{f\alpha} \cdot \boldsymbol{e}_4)\chi_{\alpha\alpha\beta\beta}(T)]$$

$$+ C_{\omega_3}^{\alpha} [((\boldsymbol{\mu}_{f\beta} \cdot \boldsymbol{e}_3)(\boldsymbol{\mu}_{f\alpha} \cdot \boldsymbol{e}_4) - (\boldsymbol{\mu}_{\alpha g} \cdot \boldsymbol{e}_3)(\boldsymbol{\mu}_{\beta g} \cdot \boldsymbol{e}_4))\chi_{\beta\alpha\beta\beta}(T)]\}$$

$$- C_{\omega_1}^{\beta} C_{\omega_2}^{\alpha} (\boldsymbol{\mu}_{\beta g} \cdot \boldsymbol{e}_1)(\boldsymbol{\mu}_{\alpha g} \cdot \boldsymbol{e}_2)$$

$$\times \{ C_{\omega_3}^{\beta} [(\boldsymbol{\mu}_{\beta g} \cdot \boldsymbol{e}_3)(\boldsymbol{\mu}_{\beta g} \cdot \boldsymbol{e}_4)(\chi_{gg\alpha\beta}(T) - \chi_{\beta\beta\alpha\beta}(T))$$

$$+ (\boldsymbol{\mu}_{f\alpha} \cdot \boldsymbol{e}_3)(\boldsymbol{\mu}_{f\alpha} \cdot \boldsymbol{e}_4)\chi_{\alpha\alpha\alpha\beta}(T)]$$

$$+ C_{\omega_3}^{\alpha} [((\boldsymbol{\mu}_{f\beta} \cdot \boldsymbol{e}_3)(\boldsymbol{\mu}_{f\alpha} \cdot \boldsymbol{e}_4) - (\boldsymbol{\mu}_{\alpha g} \cdot \boldsymbol{e}_3)(\boldsymbol{\mu}_{\beta g} \cdot \boldsymbol{e}_4))\chi_{\beta\alpha\alpha\beta}(T)]\}.$$

$$(2.13)$$

Here, the expressions have been obtained using the rotating-wave approximation, as

well as the assumption of no overlap between pulses. $\boldsymbol{\mu}_{pq} = \boldsymbol{\mu}_{qp}$ is the transition dipole moment between states $p, q \in \{g, \alpha, \beta, f\}$. We have rescaled the spectra amplitudes to eliminate the details of the lineshape by multiplying them by the dephasing rates of the optical coherences in the coherence and echo intervals,

$$\tilde{S}(\omega_{pg}, T, \omega_{qg}) = \Gamma_{gp}\Gamma_{qg}S(\omega_{pg}, T, \omega_{qg}). \tag{2.14}$$

The coefficient $C^p_{\omega_i}$ is the amplitude of the i-th pulse at the frequency ω_{pg},

$$C^p_{\omega_i} = -\frac{\Lambda}{i}\sqrt{2\pi\sigma^2}e^{-\sigma^2(\omega_{pg}-\omega_i)^2/2}, \tag{2.15}$$

with Λ being the strength of the pulse and σ the width of the Gaussian pulse in time domain. Also, $\boldsymbol{e}_i$ is the polarization of the i-th pulse. Both $C^p_{\omega_i}$ and $\boldsymbol{e}_i$ are experimentally tunable parameters for the pulses.

Whereas Equations (14) and (15) presented in [78] correspond to a single value of τ and t, Equations (2.10), (2.11), (2.12), and (2.13) stem from Fourier transform of data collected at many τ and t times (see Ref. 79). Therefore, in principle, a 2D spectrum provides a more robust source of information from which to invert $\chi(T)$ than in the suggested 1D experiment. The displayed equations, albeit lengthy, are easy to interpret. For instance, consider the term which is proportional to $\chi_{\alpha\beta\alpha\alpha}(T)$ in Equation (2.10), which stems from the Feynman diagram depicted in Fig. 2.5. As expected, it consists of a waiting time where the initially prepared population $|\alpha\rangle\langle\alpha|$ is transferred to the coherence $|\alpha\rangle\langle\beta|$. This waiting time is escorted by a coherence $|g\rangle\langle\alpha|$ oscillating as $e^{(-i\omega_{g\alpha}-\Gamma_{g\alpha})\tau}$ which evolves during the coherence time and another set of coherences $|f\rangle\langle\beta|$ and $|\alpha\rangle\langle g|$ which evolve during the echo time as $e^{(-i\omega_{f\beta}-\Gamma_{f\beta})t} = e^{(-i\omega_{\alpha g}-\Gamma_{\alpha g})t}$. These two intervals correspond to the diagonal peak
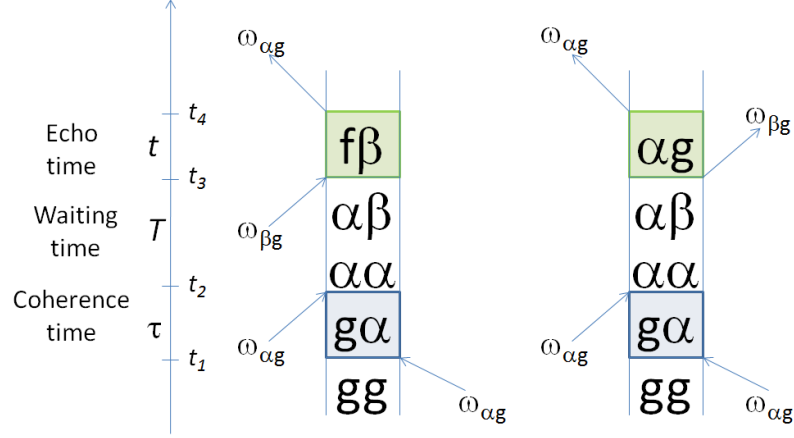
Figure 2.5: Dual Feynman diagrams that account for the population to coherence transfer terms $\chi_{\alpha\beta\alpha\alpha}(T)$ in quantum process tomography.

located at $(\omega_{\alpha g}, \omega_{\alpha g})$. Other processes that exhibit oscillations at those two respective frequencies appear as additional terms in the equation corresponding to that particular peak.

In Ref. 78, we showed that there are sixteen real valued parameters of $\chi(T)$ which need to be determined at every value of T in order to carry out QPT of the single exciton manifold of a heterodimer. For an illustration, we shall describe how to obtain the elements $\chi_{ij\alpha\alpha}(T)$. These quantities are shown in Fig. 2.6 and have been computed using the Ishizaki-Fleming model, with a bath correlation time of 150 fs [29]. They display rich and nontrivial phonon-induced behavior, such as the spontaneous generation of coherence from a population in an eigenstate of the excitonic Hamiltonian, and therefore, is a very good example of how QPT provides access to this nontrivial information via the repetition of a series of 2D PE experiments. For this particular set of $\chi(T)$ elements, we shall exploit the waveform of the pulses but not their polarizations, and for simplicity we will assume the polarization configuration

Figure 2.6: Transfer of population in eigenstate $|\alpha\rangle\langle\alpha|$ to other populations and coherences in the eigenbasis of the single exciton Hamiltonian. The hierarchy equation of motion approach is used for a dimer system based on the parameters of the site 1 a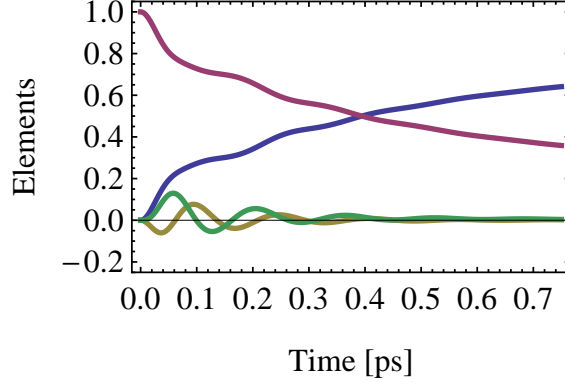nd site 2 subsystem of the Fenna-Matthews-Olson complex. Population in $|\alpha\rangle\langle\alpha|$ decreases $(\chi_{\alpha\alpha\alpha\alpha}(T)$, purple) and is transferred to $|\beta\rangle\langle\beta|$ $(\chi_{\beta\beta\alpha\alpha}(T)$, blue). Emergence of coherence from the initial population occurs in this model $(\Re\{\chi_{\alpha\beta\alpha\alpha}(T)\}$, yellow and $\Im\{\chi_{\alpha\beta\alpha\alpha}(T)\}$, green).

xxxx for each of the pulses including the heterodyning.

Consider the possibility of using pulses with carrier frequencies centered about $\omega_{\alpha g}$ and $\omega_{\beta g}$ respectively, and such that their bandwidth is narrow enough that the pulse centered about $\omega_{\alpha g}$ has negligible component at $\omega_{\beta g}$ and vice versa. Then, we can carry out an experiment such that $\frac{|C_{\omega_1}^\alpha|}{|C_{\omega_1}^\beta|}, \frac{|C_{\omega_2}^\alpha|}{|C_{\omega_2}^\beta|}, \frac{|C_{\omega_3}^\beta|}{|C_{\omega_3}^\alpha|} \gg 1$ (experiment 1) for all i and notice that the diagonal peak at $(\omega_{\alpha g}, \omega_{\alpha g})$ reduces to,

$$\langle \tilde{S}(\omega_\alpha, T, \omega_\alpha)\rangle_{xxxx} = -C_{\omega_1}^\alpha C_{\omega_2}^\alpha C_{\omega_3}^\beta$$

$$\times \langle (\boldsymbol{\mu}_{\alpha g} \cdot \boldsymbol{e}_1)(\boldsymbol{\mu}_{\alpha g} \cdot \boldsymbol{e}_2)[(\boldsymbol{\mu}_{f\alpha} \cdot \boldsymbol{e}_3)(\boldsymbol{\mu}_{f\beta} \cdot \boldsymbol{e}_4) - (\boldsymbol{\mu}_{\beta g} \cdot \boldsymbol{e}_3)(\boldsymbol{\mu}_{\alpha g} \cdot \boldsymbol{e}_4))]\rangle_{xxxx}\chi_{\alpha\beta\alpha\alpha}(T),$$

$$(2.16)$$

which implies that its evolution with respect to T directly monitors the transfer of the population prepared at $|\alpha\rangle\langle\alpha|$ to the coherence at $|\alpha\rangle\langle\beta|$. Here, $\langle\cdot\rangle_{xxxx}$ denotes an isotropic average of the experiments performed with the *xxxx* polarization configura-

tion. $\chi_{\alpha\beta\alpha\alpha}(T)$ can be directly obtained if information of the dipole moments is known in advance. As can be checked easily, $\chi_{\alpha\beta\alpha\alpha}(T) = (\chi_{\beta\alpha\alpha\alpha}(T))^*$ can, in principle, be also obtained directly from an experiment where $\frac{|C_{\omega_i}^{\alpha}|}{|C_{\omega_i}^{\beta}|} \gg 1$ for all i (experiment 2) and monitoring $\langle \tilde{S}(\omega_\alpha, T, \omega_\beta) \rangle_{xxxx}$. Redundant measurements can be used as ways of effectively constraining the QPT.

Similarly, the transfer from $|\alpha\rangle\langle\alpha|$ to other populations can be extracted by monitoring $\langle \tilde{S}(\omega_\alpha, T, \omega_\alpha) \rangle_{xxxx}$ in experiment 2 and $\langle \tilde{S}(\omega_\alpha, T, \omega_\beta) \rangle_{xxxx}$ in experiment 1. These two linearly independent conditions are enough to extract $\chi_{gg\alpha\alpha}(T)$, $\chi_{\alpha\alpha\alpha\alpha}(T)$, and $\chi_{\beta\beta\alpha\alpha}(T)$, since there is a third independent condition based on trace preservation which reads $\chi_{gg\alpha\alpha}(T) + \chi_{\alpha\alpha\alpha\alpha}(T) + \chi_{\beta\beta\alpha\alpha}(T) = 1$.

It is now important to verify whether the suggested experiments are feasible. In order to ensure conditions of the form $\frac{|C_{\omega_i}^{\alpha}|}{|C_{\omega_i}^{\beta}|} \gg 1$, we need $\sigma \sim \frac{3}{\omega_{\alpha g} - \omega_{\beta g}} \sim 75$ fs, that is, the pulse needs to be long enough to guarantee the narrow band condition. This requirement is very reasonable, as it is not too long to obscure the decoherence processes that we want to witness. In the case where the length of the pulse were of similar length as the dynamical events that one is interested in, it is not necessary to use very narrowband pulses either. The only essential requirement is a toolbox of two different waveforms for the pulses, for instance, a set of pulses centered about $\omega_{\alpha g}$ and $\omega_{\beta g}$ respectively, but having $\sigma \sim 30$ fs, for instance. By carrying out 8 experiments alternating the two waveforms in each of the three pulses, each of the terms in Equations (2.10), (2.11), (2.12), and (2.13) which are proportional to $C_{\omega_1}^{i} C_{\omega_2}^{j} C_{\omega_3}^{k}$ for $i, j, k \in \{\alpha, \beta\}$ may be inverted to yield the block diagonal set of equations discussed above.

In summary, we have presented three different tools for unraveling the role of quantum coherence in biological systems: a) techniques for obtaining the contribution of quantum coherences to biological processes; b) a microscopic simulation approach to explore the dynamics of these systems by direct simulation; and finally c) a new theoretical proposal for an experimental procedure that provides detailed information about the quantum procesess associated with energy transfer in the ultrafast regime. We believe that ultimately, a combination of these three techniques and tools from other groups will be collectively required to make definitive conclusions about the role of quantum coherence in photosynthetic complexes.

Chapter 3

Atomistic study of the long-lived quantum coherences in the Fenna-Matthews-Olson complex

3.1 Introduction

Recent experiments suggest the existence of long-lived quantum coherence during the electronic energy transfer process in photosynthetic light-harvesting complexes under physiological conditions [23–25]. This has stimulated many researchers to seek for the physical origin of such a phenomenon. The role and implication of quantum coherence during the energy transfer have been explored in terms of the theory of open quantum systems [27–29, 48, 50, 51, 60, 86–91], and also in the context of quantum information and entanglement [52–54, 92]. However, the characteristics of the protein environment, and especially its thermal vibrations or phonons, have not

been fully investigated from the molecular viewpoint. A more detailed description of the bath in atomic detail is desirable; to investigate the structure-function relationship of the protein complex and to go beyond the assumptions used in popular models of photosynthetic systems.

Protein complexes constitute one of the most essential components in every biological organism. They remain one of the major targets of biophysical research due to their tremendously diverse and, in some cases, still unidentified structure-function relationship. Many biological units have been optimized through evolution and the presence of certain amino acids rather than others is fundamental for functionality [61–63]. In photosynthesis, one of the most well-characterized pigment-protein complexes is the Fenna-Matthews-Olson (FMO) complex which is a light-harvesting complex found in green sulphur bacteria. It functions as an intermediate conductor for exciton transport located between the antenna complex where light is initially absorbed and the reaction center. Since the resolution of its crystal structure over 30 years ago [12], the FMO trimer, composed of 3 units each comprising 8 bacteriochlorophylls has been extensively studied both experimentally [15–18] and theoretically [13, 14]. For instance regarding the structure-function relationship, it has been shown [93] that amino acid residues cause considerable shifts in the site energies of bacteriochlorophyll *a* (BChl) molecules of the FMO complex and in turn causes changes to the energy transfer properties.

Have photosynthetic systems adopted interesting quantum effects to improve their efficiency in the course of evolution, as suggested by the experiments? In this article, we provide a first step to answer this question by characterizing the protein

environment of the FMO photosynthetic system to identify the microscopic origin of the long-lived quantum coherence. We investigate the quantum energy transfer of a molecular excitation (exciton) by incorporating an all-atom molecular dynamics (MD) simulation. The molecular energies are computed with time-dependent density functional theory (TDDFT) along the MD trajectory. The evolution of the excitonic density matrix is obtained as a statistical ensemble of unitary evolutions by a time-dependent Schrödinger equation. Thus, this work is in contrast to many studies based on quantum master equations in that it includes atomistic detail of the protein environment into the dynamical description of the exciton. We also introduce a novel approach to add quantum corrections to the dynamics. Furthermore, a quantitative comparison to the hierarchical equation of motion and the Haken-Strobl-Reineker method is presented. As the main result, the time evolution of coherences and populations shows characteristic beatings on the time scale of the experiments. Surprisingly, we observe that the cross-correlation of site energies does not play a significant role in the energy transfer dynamics.

The paper is structured as follows: In the first part we present the methods employed and in the second part the results followed by conclusions. In particular, the partitioning of the system and bath Hamiltonian in classical and quantum degrees of freedom and details of the MD simulations and calculation of site energies are discussed in Section 3.2.1. The exciton dynamics of the system under the bath fluctuations is then presented in Section 3.2.2. In Section 3.2.3 we introduce a quantum correction to the previous exciton dynamics. Using the discussed methods we evaluated site energies and their distribution at 77 and 300K in Section 3.3.1 and we also

computed the linear absorption spectrum of the FMO complex in Section 3.3.3. The site basis dephasing rates are discussed in Section 3.3.2. From the exciton dynamics of the system we obtained populations and coherences and compared to the QJC-MD approach in Section 3.3.4. We then compare the MD and quantum corrected MD methods to the hierarchical equation of motion (HEOM) and Haken-Strobl-Reineker (HSR) methods in Section 3.3.5. In Section 3.3.6 we determined the spectral density for each site from the energy time bath-correlator and studied the effect of auto and cross-correlations on the exciton dynamics by introducing a comparison to first-order autoregressive processes. We conclude in Section 3.4 by summarizing our results.

3.2   Methods

3.2.1   Molecular Dynamics Simulations

A computer simulation of the quantum evolution of the entire FMO complex is certainly unfeasible with the currently available computational resources. However, we are only interested in the electronic energy transfer dynamics among BChl molecules embedded in the protein support. This suggests a decomposition of the total system Hamiltonian operator into three parts: the relevant system, the bath of vibrational modes, and the system-bath interaction Hamiltonians. The system Hamiltonian operates on the excitonic system alone which is defined by a set of two-level systems. Each two-level system represents the ground and first excited electronic state of a BChl molecule. In addition, the quantum mechanical state of the exciton is assumed to be restricted to the single-exciton manifold because the exciton density is low.

On the other hand, factors affecting the system site energies have intractably large degrees of freedom, so it is reasonable to treat all those degrees of freedom as the bath of an open quantum system.

More formally, to describe the system-bath interplay by including atomistic detail of the bath, we start from the total Hamiltonian operator and decompose it in a general way such that no assumptions on the functional form of the system-bath Hamiltonian are necessary [67]:

$$
\begin{aligned}
\hat{H}_{total} &= \sum_m \int d\boldsymbol{R} \; \epsilon_m(\boldsymbol{R})|m\rangle\langle m| \otimes |\boldsymbol{R}\rangle\langle\boldsymbol{R}| \\
&+ \sum_{m,n} \int d\boldsymbol{R} \; \{J_{mn}(\boldsymbol{R})|m\rangle\langle n| \otimes |\boldsymbol{R}\rangle\langle\boldsymbol{R}| + c.c.\} \\
&+ |\boldsymbol{1}\rangle\langle\boldsymbol{1}| \otimes \hat{T}_{\boldsymbol{R}} + \sum_m \int d\boldsymbol{R} \; V_m(\boldsymbol{R})|m\rangle\langle m| \otimes |\boldsymbol{R}\rangle\langle\boldsymbol{R}|.
\end{aligned} \tag{3.1}
$$

Here, $\boldsymbol{R}$ corresponds to the nuclear coordinates of the FMO complex including both BChl molecules, protein, and enclosing water molecules. The set of states $|m\rangle \otimes |\boldsymbol{R}\rangle$ denote the presences of the exciton at site m given that the FMO complex is in the configuration $\boldsymbol{R}$, $\epsilon_m(\boldsymbol{R})$ represents the site energy of the mth site and $J_{mn}(\boldsymbol{R})$ is the coupling constant between the mth and nth sites. Note that the site energies and coupling terms can be modulated by $\boldsymbol{R}$. $|\boldsymbol{1}\rangle\langle\boldsymbol{1}|$ is the identity operator in the excitonic subspace, $\hat{T}_{\boldsymbol{R}}$ is the kinetic operator for the nuclear coordinates of the FMO complex, and $V_m(\boldsymbol{R})$ is the potential energy surface for the complex when the exciton at site m under Born-Oppenheimer approximation. Given multiple Born-Oppenheimer surfaces, one would need to carry out a coupled nonadiabatic propagation. However, as a first approximation, we assume that the change of Born-Oppenheimer surfaces does not affect the bath dynamics significantly. This approximation becomes better

at small reorganization energies. Indeed, BChl molecules have significantly smaller
reorganization energies than other chromophores [94]. With this assumption, we can
ignore the dependence on the excitonic state in the V term, thus the system-bath
Hamiltonian only contains the one-way influence from the bath to the system. We
also adopted Condon approximation so that the J terms do not depend on $\boldsymbol{R}$:

$$
\begin{aligned}
H_S &= \sum_m \int d\boldsymbol{R}\ \bar{\epsilon}_m |m\rangle\langle m| \otimes |\boldsymbol{R}\rangle\langle\boldsymbol{R}| + \sum_{m,n} \int d\boldsymbol{R}\ \{J_{mn}(\boldsymbol{R})|m\rangle\langle n| \otimes |\boldsymbol{R}\rangle\langle\boldsymbol{R}| + c.c.\}\,, \\
&\approx \sum_m \int d\boldsymbol{R}\ \bar{\epsilon}_m |m\rangle\langle m| \otimes |\boldsymbol{R}\rangle\langle\boldsymbol{R}| + \sum_{m,n} \int d\boldsymbol{R}\ \{\bar{J}_{mn}|m\rangle\langle n| \otimes |\boldsymbol{R}\rangle\langle\boldsymbol{R}| + c.c.\}\,, \\
H_B &= |\mathbf{1}\rangle\langle\mathbf{1}| \otimes \hat{T}_{\boldsymbol{R}} + \sum_m \int d\boldsymbol{R}\ V_m(\boldsymbol{R})|m\rangle\langle m| \otimes |\boldsymbol{R}\rangle\langle\boldsymbol{R}|, \\
&\approx |\mathbf{1}\rangle\langle\mathbf{1}| \otimes \hat{T}_{\boldsymbol{R}} + \int d\boldsymbol{R}\ V_{ground}(\boldsymbol{R})|\mathbf{1}\rangle\langle\mathbf{1}| \otimes |\boldsymbol{R}\rangle\langle\boldsymbol{R}|, \\
H_{SB} &= \sum_m \int d\boldsymbol{R}\ \{\epsilon_m(\boldsymbol{R}) - \bar{\epsilon}_m\} |m\rangle\langle m| \otimes |\boldsymbol{R}\rangle\langle\boldsymbol{R}|, \\
\end{aligned}
$$

$$
H_{total} = H_S + H_B + H_{SB}. \tag{3.2}
$$

Based on this decomposition of the total Hamiltonian, we set up a model of the FMO
complex with the AMBER 99 force field [64, 65] and approximate the dynamics of
the protein complex bath by classical mechanics. The initial configuration of the
MD simulation was taken from the x-ray crystal structure of the FMO complex of
Prosthecochloris aestuarii (PDB ID: 3EOJ.). Shake constraints were used for all
bonds containing hydrogen and the cutoff distance for the long range interaction
was chosen to be 12 Å. After a 2ns long equilibration run, the production run was
obtained for a total time of 40ps with a 2fs timestep. For the calculation of the
optical gap, snapshots were taken every 4fs. Two separate simulations at 77K and
300K were carried out with an isothermal-isobaric (NPT) ensemble to investigate the

temperature dependence of the bath environment. Then, parameters for the system and the system-bath Hamiltonian were calculated using quantum chemistry methods along the trajectory obtained from the MD simulations.

We chose not to include the newly resolved eighth BChl molecule [93] in our simulations because up to now, the large majority of the scientific community has focused on the seven site system which is therefore a better benchmark to compare our calculations to previous work. It is important to note however that this eighth site may have an important role on the dynamics. In particular, as suggested in [95, 96] this eighth site is considered to be the primary entering point for the exciton in the FMO complex and its position dictates a preferential exciton transport pathway rather than two independent ones. Also when starting with an exciton on this eighth site, the oscillations in the coherences are largely suppressed.

The time-dependent site energy ϵ_m was evaluated as the excitation energy of the Q_y transition of the corresponding BChl molecule. We employed the time-dependent density functional theory (TDDFT) with BLYP functional within the Tamm-Dancoff approximation (TDA) using the Q-Chem quantum chemistry package [66]. The basis set was chosen to be 3-21G after considering a trade-off between accuracy and computational cost. The Q_y transition was identified as the excitation with the highest oscillator strength among the first 10 singlet excited states. Then, the transition dipole of the selected state was verified to be parallel to the y molecular axis. Every atom which did not belong to the TDDFT target molecule was incorporated as a classical point charge to generate the external electric field for the QM/MM calculation. Given that the separation between BChl molecules and the protein matrix is

quite clear, employing this simple QM/MM method with classical external charges to calculate the site energies is a good approximation. The external charges were taken from the partial charges of the AMBER force field [64, 65]. The coupling terms, J_{mn}, can also be obtained from quantum chemical approaches like transition density cube or fragment-excitation difference methods [97, 98]. However, in this case we employed the MEAD values of the couplings of the Hamiltonian presented in the literature [14] and considered them to be constant in time. $\bar{\epsilon}_m$ was straightforwardly chosen as the time averaged site energy for the mth site.

3.2.2   Exciton Dynamics

In this section, we describe the method for the dynamics of the excitonic reduced density matrix within our molecular dynamic simulation framework. It is based on a simplified version of the quantum-classical hybrid method (Ehrenfest) described in [67]. The additional assumption on Hamiltonian (3.2) is that the bath coordinate $\boldsymbol{R}$ is a classical variable, denoted by a superscript "cl". As discussed above, the time-dependence of these variables arises from the Newtonian MD simulations. The additional force on the nuclei due to the electron-phonon coupling [67] is neglected. Hence, the Schrödinger equation for the excitonic system is given by:

$$i\hbar\frac{\partial}{\partial t}|\psi(t)\rangle \approx \left\{H_S + H_{SB}(\boldsymbol{R}^{cl}(t))\right\}|\psi(t)\rangle. \tag{3.3}$$

The system-environment coupling leads to an effective time-dependent Hamiltonian $H_{eff}(t) = H_S + H_{SB}(\boldsymbol{R}^{cl}(t))$. This equation suggests a way to propagate the reduced density matrix as an average of unitary evolutions given by Eq. (3.3). First, short MD trajectories (in our case 1 ps long) are uniformly sampled from the full MD trajectory

(40 ps). Then, for each short MD trajectory, the excitonic system can be propagated under unitary evolution with a simple time-discretized exponential integrator. The density matrix is the classical average of these unitary evolutions:

$$\rho_S(t) = \frac{1}{M} \sum_{i=1}^{M} |\psi_i(t)\rangle\langle\psi_i(t)|, \tag{3.4}$$

where M is the number of sample short trajectories. Each trajectory is subject to different time-dependent fluctuations from the bath, which manifests itself as decoherence when averaged to the statistical ensemble. Compared to many methods based on the stochastic unraveling of the master equation, e.g. [59, 99], our formalism directly utilizes the fluctuations generated by the MD simulation. Therefore, the detailed interaction between system and bath is captured. The temperature of the bath is set by the thermostat of the MD simulation, thus no further explicit temperature dependence is required in the overall dynamics. The dynamics obtained by this numerical integration of the Schrödinger equation will also be compared to the HEOM approach. The HEOM is briefly described in the Supporting Material along with a discussion on the differences respect to the MD-method.

3.2.3   Quantum Jump Correction to MD Method (QJC-MD)

The MD/TDDFT simulation above leads to crucial insights into the exciton dynamics. However, it does not capture quantum properties of the vibrational environment such as zero-point fluctuations. At zero temperature all the atoms in the MD simulation are completely frozen. Moreover, similarly to an infinite-temperature model, at long times of the quantum dynamical simulation the exciton is evenly distributed among all molecules, as we will see below. In order to obtain a more

realistic description, we modify the stochastic simulation by introducing quantum jumps derived from the zero-point (zp) fluctuations of the modes in the vibrational environment. We refer to this corrected version of the MD propagation as QJC-MD.

Introducing harmonic bath modes explicitly we reformulate the system-bath Hamiltonian as:

$$H_{SB} = \sum_m |m\rangle\langle m| \sum_\xi g_\xi^m R_\xi. \tag{3.5}$$

Here, each g_ξ^m represents the coupling strength of a site m to a particular mode ξ and R_ξ is the dimensionless position operator for that mode. We now formulate our correction by separating the bath operators into two parts, $R_\xi = R_\xi^{zp} + R_\xi^{MD}$, the first part is due to zero-point fluctuations and the second comes from our MD simulations. As above, the MD part is replaced by the classical time-dependent variables, $R_\xi^{MD} \rightarrow R_\xi^{cl}(t)$. The zero-point operator is expressed by creation and annihilation operators, $R_\xi^{zp} = b_\xi^{zp} + b_\xi^{zp,\dagger}$, which satisfy the usual commutation relations $[b_\xi^{zp}, b_{\xi'}^{zp,\dagger}] = \delta_{\xi\xi'}$. By construction, for the zp-fluctuations one has $\langle b_\xi^{zp,\dagger} b_\xi^{zp}\rangle = 0$.

The zp-fluctuations can only induce excitonic transitions from higher to lower exciton states in the instantaneous eigenbasis of the Hamiltonian, thus leading to relaxation of the excitonic system. The evolution of the populations P_M of the instantaneous eigenstates $|M\rangle(t)$ due to the zero-point correction is expressed by a Pauli master equation as:

$$\left(\dot{P}_M\right)_{zpc} = -\sum_N \gamma(\omega_{MN})P_M + \sum_N \gamma(\omega_{NM})P_N, \tag{3.6}$$

and for the coherences as:

$$\left(\dot{C}_{MN}\right)_{zpc} = -\frac{1}{2}\gamma(|\omega_{MN}|)C_{MN}. \tag{3.7}$$

The associated rate can be derived from a secular Markovian Redfield theory [34] to be $\gamma(\omega_{MN}) = 2\pi J(\omega_{MN}) \sum_m |c_m(M)|^2 |c_m(N)|^2$, where the spectral density $J(\omega)$ is only non-zero for positive transition frequencies $\omega_{MN} = E_M - E_N$ and taken to be as in [87]. The coefficients $c_m(M)$ translate from site to energy basis. The time evolution given by Equations (3.6) and (3.7) is included in the dynamics simulation by introducing quantum jumps as in the Monte-Carlo wavefunction (MCWF) method [99]. We thus arrive at a hybrid classically averaged $H(t)$ simulation with additional quantum transitions induced by the vacuum fluctuations of the vibrational modes.

3.3 Results and Discussion

3.3.1 Site Energy Distributions

Using the coupled QM/MD simulations, site energies were obtained for each BChl molecule. These energies and their fluctuations are reported in Figure 3.1. We note that the magnitude of the fluctuations are of the order of hundreds of cm^{-1}. Although the order of the site energies does not perfectly match previously reported results [14, 20], the overall trend does not deviate much, especially considering that our result is purely based on *ab initio* calculations without fitting to the experimental result. The Q_y transition energies calculated by TDDFT are known to be systematically blue-shifted with respect to the experiment [100]. However, the scale of the fluctuations remains reasonable. Therefore, the comparison in Fig. 3.1 was made after shifting the overall mean energy to zero for each method.

The excitation energy using TDDFT does not always converge when the config-
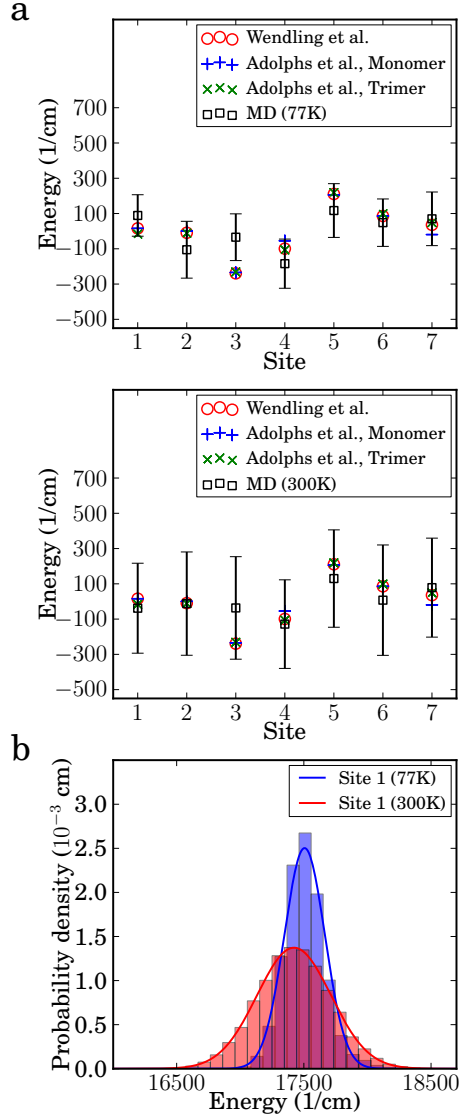
Figure 3.1: Panel **a**: Comparison of the calculated site energies for each BChl molecule to the previous works by Wendling et al. and Adolphs et al. [14, 20]. Our calculation, labeled as MD, was obtained using QM/MM calculations with the TDDFT/TDA method at 77K and 300K. Vertical bars represent the standard deviation for each site. Panel **b**: Marginal distribution of site 1 energy at 77K and 300K. Histograms represent the original data, and solid lines correspond to the estimated Gaussian distribution.

uration of the molecule deviates significantly from its ground state structure. The number of points which failed to converge was on average less than 4% for configurations at 300K, and less than 2% at 77K. We interpolated the original time series to obtain smaller time steps and recover the missing points. Interpolation could lead to severe distortion of the marginal distribution when the number of available points is too small. However, in our case, the distributions virtually remained the same with and without interpolation.

3.3.2 Dephasing Rates

In the Markovian approximation and assuming an exponentially decaying autocorrelation function, the dephasing rate γ_ϕ is proportional to the variance of the site energy σ_ϵ^2 [34]:

$$\gamma_\phi = \frac{2}{\hbar}\sigma_\epsilon^2\tau, \tag{3.8}$$

where τ is a time decay parameter which we estimated through a comparison to first order autoregressive processes, as described in Section 3.3.6. The dependence on the variance is clearly justified: states associated with large site energy fluctuations tend to undergo faster dephasing. Figure 3.2, panel a), presents the approximate site basis dephasing rates for each site with $\tau \approx 5$fs. The averaged value of the slopes is 0.485 cm^{-1} K^{-1}, which is in good agreement with the experimentally measured value of 0.52 cm^{-1} K^{-1} obtained from a closely related species *Chlorobium tepidum* in the exciton basis [25]. From this plot we note the presence of a positive correlation between temperature and dephasing rate. This correlation is plausible: as temperature increases so does the energy disorder, hence the coherences should decay faster. In

68

fact, in the Markovian approximation, dephasing rates increase linearly with temperature [34, 101]. Calculations at other temperatures are underway to verify this and to obtain more information on the precise temperature dependence of the dephasing rates.

3.3.3 Simulated Spectra

The absorption, linear dichroism (LD), and circular dichroism (CD) spectra can be obtained from the Fourier transform of the corresponding response functions. The spectra can be evaluated for the seven BChl molecules using the following expressions [102, 103]:

$$
I_{Abs}(\omega) \propto \mathrm{Re} \int_0^\infty dt\ e^{i\omega t} \sum_{m,n=1}^{7} \langle \vec{d}_m \cdot \vec{d}_n \rangle \{ \langle U_{mn}(t,0) \rangle - \langle U_{mn}^*(t,0) \rangle \},
$$

$$
I_{LD}(\omega) \propto \mathrm{Re} \int_0^\infty dt\ e^{i\omega t} \sum_{m,n=1}^{7} \langle 3(\vec{d}_m \cdot \hat{r})(\vec{d}_n \cdot \hat{r}) - \vec{d}_m \cdot \vec{d}_n \rangle \{ \langle U_{mn}(t,0) \rangle - \langle U_{mn}^*(t,0) \rangle \},
$$

$$
I_{CD}(\omega) \propto \mathrm{Re} \int_0^\infty dt\ e^{i\omega t} \sum_{m,n=1}^{7} \langle \bar{\epsilon}_m(\vec{R}_m - \vec{R}_n) \cdot (\vec{d}_m \times \vec{d}_n) \rangle \{ \langle U_{mn}(t,0) \rangle - \langle U_{mn}^*(t,0) \rangle \},
$$

$$
(3.9)
$$

where m and n are indices for the BChl molecules in the complex, $\vec{d}_m$ is the transition dipole moment of the mth site, $U_{mn}(t,0)$ is the (m,n) element of the propagator in the site basis, $\hat{r}$ is the unit vector in the direction of the rotational symmetry axis, $\vec{R}_m$ is the coordinate vector of the site m, and $\langle \cdots \rangle$ indicates an ensemble average. The ensemble average was evaluated by sampling and averaging over 4000 trajectories. We applied a low-pass filter to smooth out the noise originated from truncating the integration and due to the finite number of trajectories. Figure 3.2 panel b) and
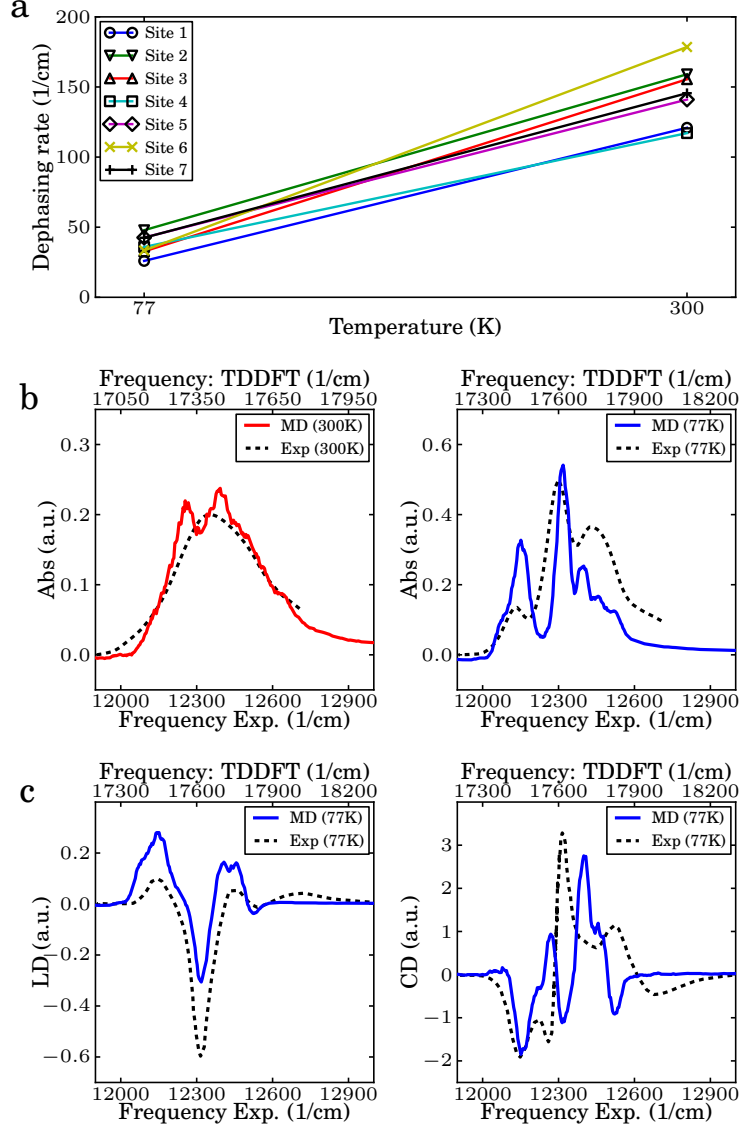
Figure 3.2: Panel **a** shows the calculated dephasing rate for each site at 77K and 300K. Panel **b** shows the simulated linear absorption spectra of the FMO complex at 77K and 300K. They were shifted to be compared to the experimental spectra as obtained by Engel through personal communication. Panel **c** shows the simulated linear dichroism (LD) and circular dichroism (CD) spectra at 77K. Experimental spectra were obtained from Wendling et al.[20] Although TDDFT-calculated spectra shows systematically overestimated site energies, the width and overall shape of the spectra is in good agreement.

c) show direct comparison of the calculated and experimental spectra at 77K and 300K. As discussed in Section 3.3.1, TDDFT tends to systematically overestimate the excitation energy of the Q_y transition [104] yet the fluctuation widths of the site energies are reasonable. In fact, the width and overall shape of the calculated spectrum is in good agreement with the experimental spectrum at each temperature. Calculated LD and CD spectra also reproduce well the experimental measurements, considering that no calibration to experiments was carried out. Since both LD and CD spectra are sensitive to the molecular structure it appears that our microscopic model correctly captures these details.

3.3.4 Population Dynamics and Long-lived Quantum Coherence

The MD method is based on minimal assumptions and directly evaluates the dynamics of the reduced density matrix from the total density matrix as described in Section 3.2. The reduced density matrix was obtained after averaging over 4000 trajectories. Figure 3.3 shows the population and coherence dynamics of each of the seven sites according to the dephasing induced by the nuclear motion of the FMO complex. In particular, the populations and the absolute value of the pairwise coherences, as defined in [52] ($2 \cdot |\rho_{12}(t)|$ and $2 \cdot |\rho_{56}(t)|$) are plotted at both 77 and 300K starting with an initial state in site 1 (first three panels) and then in site 6 (last three panels). Until very recently [95, 96] site 1 and 6 have been thought as the entry point of an exciton in the FMO complex, therefore most of the previous literature chose the initial reduced density matrix to be either pure states $|1\rangle\langle 1|$ or

71

$|6\rangle\langle6|$ [29, 51, 105]. However, our method could be applied to any mixed initial state without modification. We note that coherent beatings last for about 400fs at 77K and 200fs at 300K. These timescales are in agreement with those reported for FMO [25, 29] and with what was found in Section 3.3.2. Although quite accurate in the short time limit, the MD method populations do not reach thermal equilibrium at long times. This was verified by propagating the dynamics to twice the time shown in Figure 3.3. This final classical equal distribution is similar to the HSR model result. The three central panels of Figure 3.3 show the same populations and coherences obtained from the QJC-MD method. As discussed in Section 3.2, this method includes a zero point correction through relaxation transitions and predicts a more realistic thermal distribution at 77K. At 300K the quantum correction is less important in the dynamics because the Hamiltonian fluctuations dominate over the zero temperature quantum fluctuations.

3.3.5 Comparison between MD, QJC-MD, HEOM, and HSR Methods

Figure 3.4 shows a direct comparison of the population dynamics of site 1 calculated using the HEOM method discussed by Ishizaki and Fleming [29, 58], our MD and quantum corrected methods at 77K and 300K, and the HSR model [39, 40] with dephasing rates obtained from Eq. (3.8). We observe that the short-time dynamics and dephasing characteristics are surprisingly similar, considering that the methods originate from very different assumptions. Atomistic detail can allow for differentiation of the system-environment coupling for different chromophores. For example, at
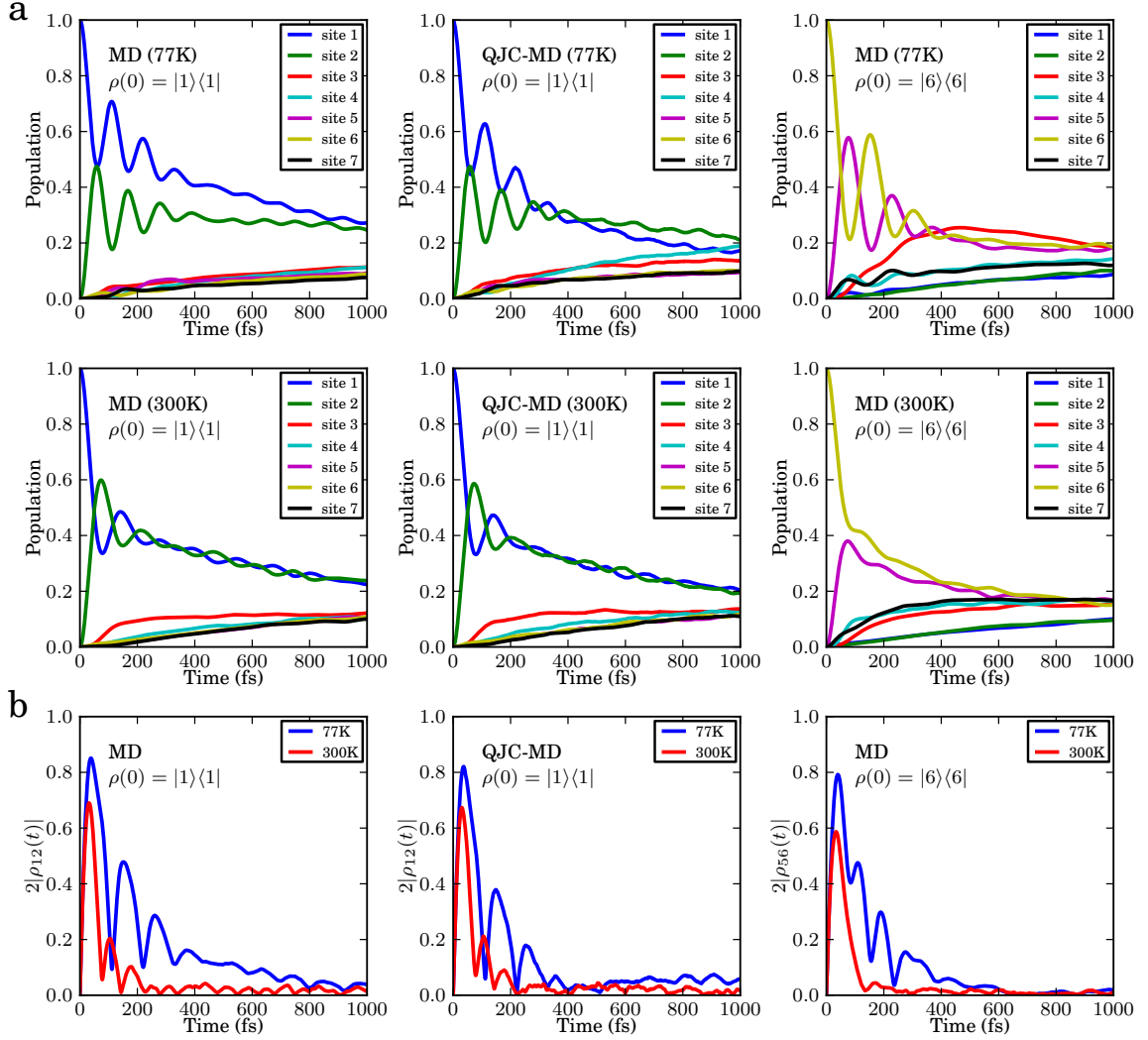
Figure 3.3: Panel **a**: Time evolution of the exciton population of each chromophore in the FMO complex at 77K and 300K. Panel **b**: Change of the pairwise coherence, or concurrence in time. Initial pure states, $\rho_S(0) = |1\rangle\langle 1|$ for the top and center panels were propagated using the two formulations developed in this article, MD and QJC-MD, to utilize the atomistic model of the protein complex bath from the MD/TDDFT calculation. Panel **c** The initial state was set to $|6\rangle\langle 6|$ and propagated using the MD method.

both temperatures (right panels), the MD populations of site 6 undergo faster decoherence than the corresponding HEOM results. We attribute this to the difference in energy gap fluctuations of site energy between site 1 and 6 obtained from the MD simulation as can be seen in 3.1. On one hand, in the HEOM method, site energy fluctuations are considered to be identical across all sites, on the other, in our method the fluctuations of each site are obtained from the MD simulation in which each site is associated with a different chromophore-protein coupling. Nevertheless, the fact that we obtain qualitatively similar results to the HEOM approach (at least when starting in $\rho(0) = |1\rangle \langle 1|$) without considering non equilibrium reorganization processes suggests that such processes might not be dominant in the FMO. The quantum correction results (QJC-MD), for every temperature and initial state, are in between the HEOM and MD results. This is due to the induced relaxation from zero-point fluctuations of the bath environment, which are not included in the MD method but included in the QJC-MD and HEOM methods.

The HSR results take into account the site-dependence of the dephasing rates based on Eq. (3.8). The method is briefly described in the supplementary material. Due to the Markovian assumption, this model shows slightly less coherence than the HEOM method and similarly to the MD method it converges to an equal classical mixture of all sites in the long time limit.

3.3.6   Correlation Functions and Spectral Density

The bath autocorrelation function and its spectral density contain information on interactions between the excitonic system and the bath. The bath correlation
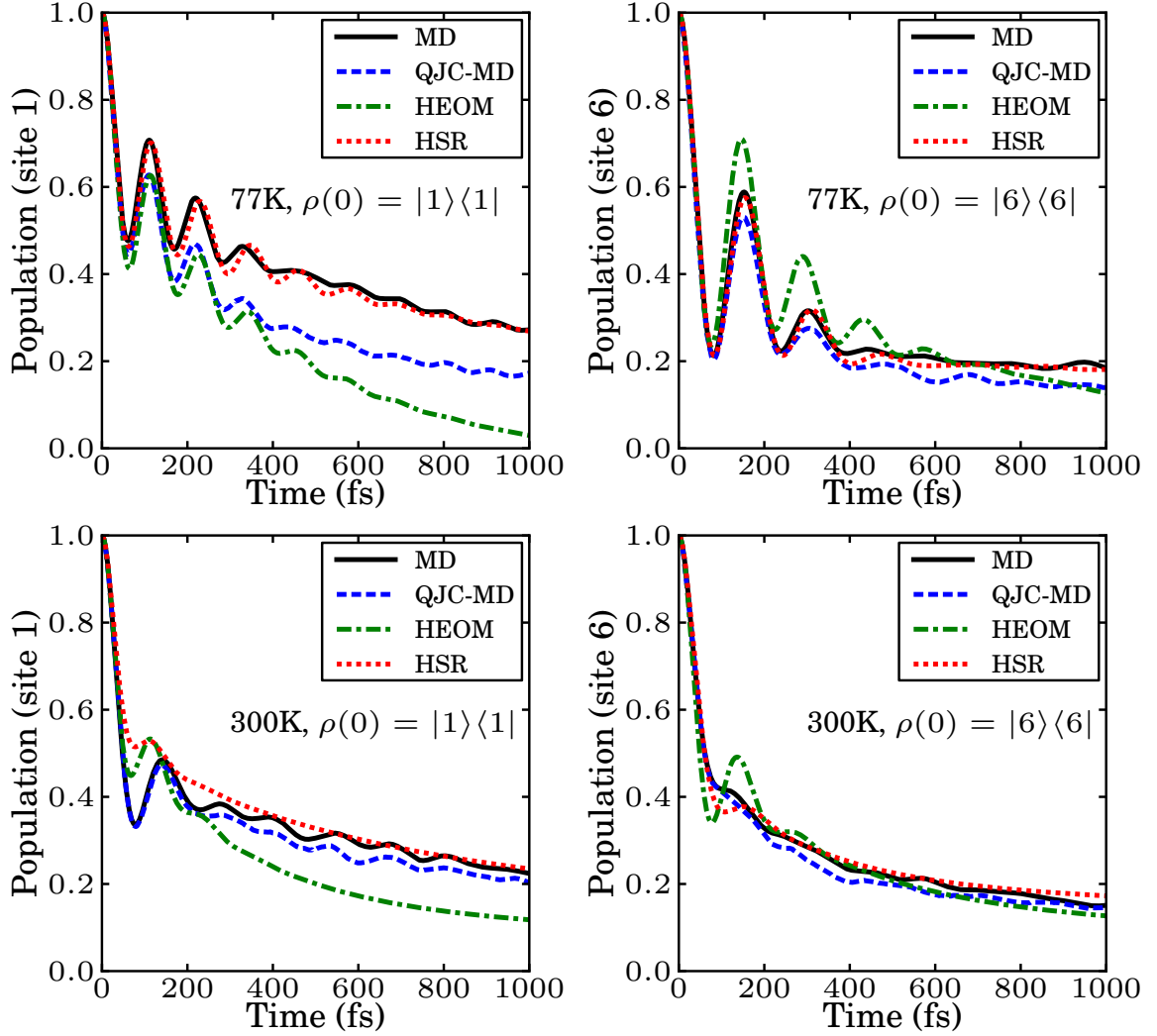
Figure 3.4: Comparison of the population dynamics obtained by using the MD method, the corrected MD, the hierarchy equation of motion approach and the Haken-Strobl-Reineker model at 77K and 300K. Panels on the right correspond to the initial state in site 1 and those on the left to an initial state in site 6. All methods show similar short-time dynamics and dephasing, while the long time dynamics is different and the different increases as relaxation is incorporated in the various methods.

function is defined as $C(t) = \langle \delta\epsilon(t)\delta\epsilon(0) \rangle$ with $\delta\epsilon = \epsilon(t) - \bar{\epsilon}$. For the MD simulation, $C(t)$ is shown in Fig. 3.5 a) for the two temperatures.

To study the effect of the decay rate of the autocorrelation function on the population dynamics, we modeled site energies using first-order autoregressive (AR(1)) processes [106]. The marginal distribution of each process was tuned to have the same mean and variance as for the MD simulation. The autocorrelation function of the AR(1) process is an exponentially decaying function:

$$C(t) \propto \exp(-t/\tau). \tag{3.10}$$

We generated three AR(1) processes with different time constants τ and propagated the reduced density matrix using the Hamiltonian corresponding to each process. As can be seen in Fig. 3.5, panel a), the autocorrelation function of the AR(1) process with $\tau \approx 5\text{fs}$ has a similar initial decay rate to that of the MD simulation at both temperatures. Therefore, as shown in the last three horizontal panels, its spectral density is in good agreement with the MD simulation result in the low frequency region, i.e up to 600cm^{-1}. Modes in this region are known to be the most important in the dynamics and in determining the the decoherence rate. Also, as panels b) and c) show, that same AR(1) process with $\tau \approx 5\text{fs}$ exhibits similar population beatings and concurrences to those of the MD simulation. The relation of this 5fs time scale to others reported in [21, 29] is presently unclear. We suspect that the discrepancy between the two results should decrease when one propagates the MD in the excited state. Work in this direction is in progress in our group.

The spectral density can be evaluated as the reweighted cosine transform of the
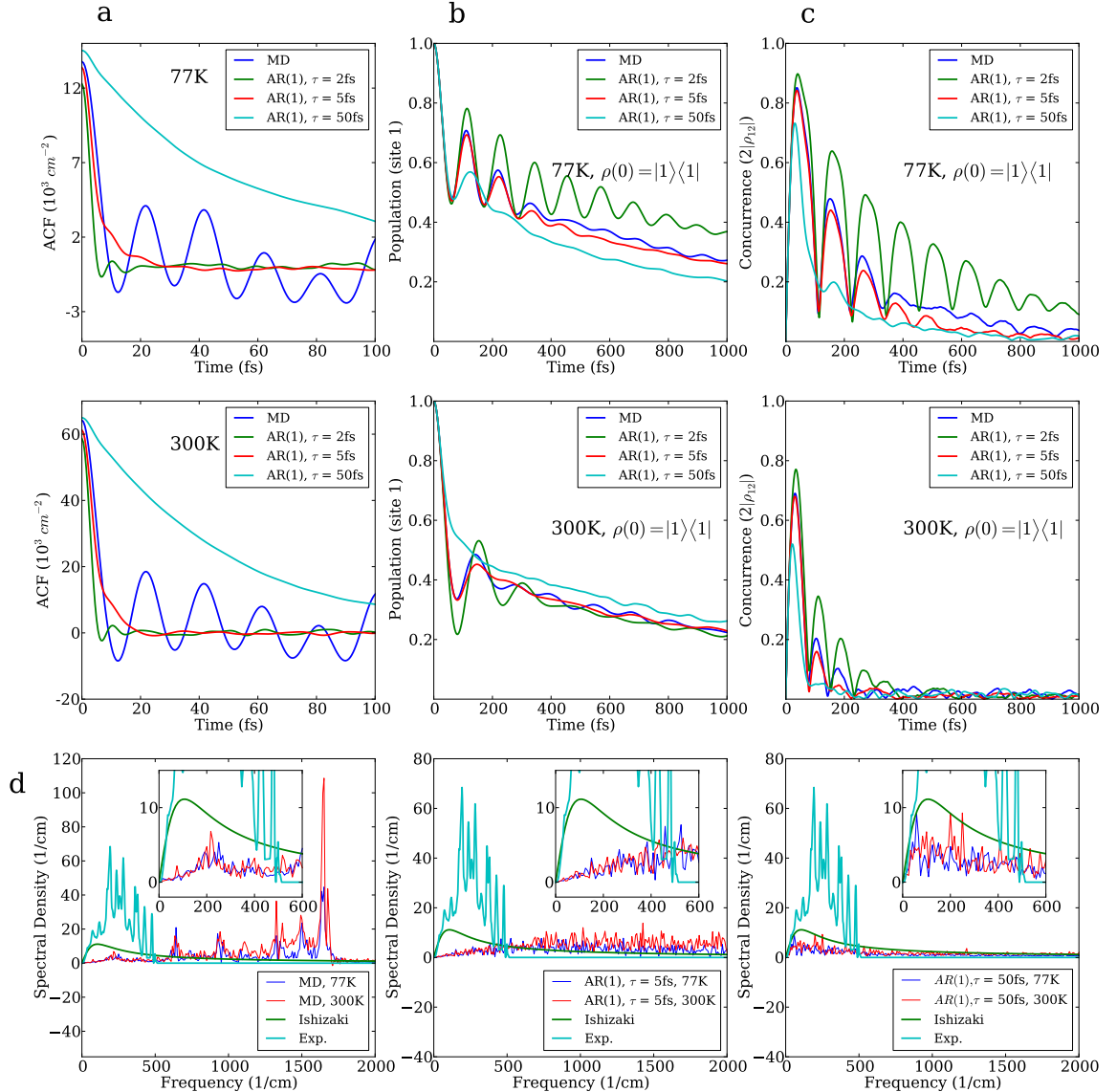
Figure 3.5: Panel **a**: Site 1 autocorrelation functions using MD and AR(1) processes generated with time constant equal to 2fs, 5fs, and 50fs at 77K and 300K. Panel **b**: Site 1 population dynamics of MD and AR(1) processes with the different time constants at 77K and 300K. Panel **c**: The change of pairwise coherence between site 1 and 2 of MD and AR(1) processes with the different time constants at 77K and 300K. Panel **d**: Spectral density of site 1 of the FMO complex from the MD simulation at 77K and 300K. They clearly show the characteristic vibrational modes of the FMO complex. High-frequency modes are overpopulated due to the ultraviolet catastrophe observed in classical mechanics. The Ohmic spectral density used by Ishizaki and Fleming in [29] was presented for comparison. The spectral densities of site 1 from AR(1) processes are also presented.

corresponding bath autocorrelation function $C(t)$ [103, 104],

$$J(\omega) = \frac{2}{\pi\hbar}\tanh(\beta\hbar\omega/2)\int_0^\infty C(t)\cos(\omega t)\ dt. \qquad (3.11)$$

With the present data the spectral density exhibits characteristic phonon modes from the dynamics of the FMO complex, see Fig. 3.5 d) first panel. However, high-frequency modes tend to be overpopulated due to the limitation of using classical mechanics. Most of these modes are the local modes of the pigments, which can be seen from the pigment-only calculation in [65]. There are efforts to incorporate quantum effects into the classical MD simulation in the context of vibrational coherence [68–70]. We are investigating the possibilities of incorporating corrections based on a similar approach. Moreover, we also obtain a discrepancy of the spectral density in the low frequency region. On one hand, the origin could lie in the harmonic approximation of the bath modes leading to the tanh prefactor in Eq. (3.11) or in the force field used in this work. On the other, the form of the standard spectral density is from [17] which measures fluorescence line-narrowing on a much longer timescale, around ns, than considered in our simulations (around ps). Assuming correctness of our result, this implies that for the simulation of fast exciton dynamics in photosynthetic light-harvesting complexes a different spectral density than the widely used one has to be employed.

Site energy cross-correlations between chromophores due to the protein environment have been postulated to contribute to the long-lived coherence in photosynthetic systems [24]. Many studies have explored this issue, e.g. recently [14, 51, 60, 107–109]. We tested this argument by de-correlating the site energies. For each unitary evolution, the site energies of different molecules at the same time were taken from
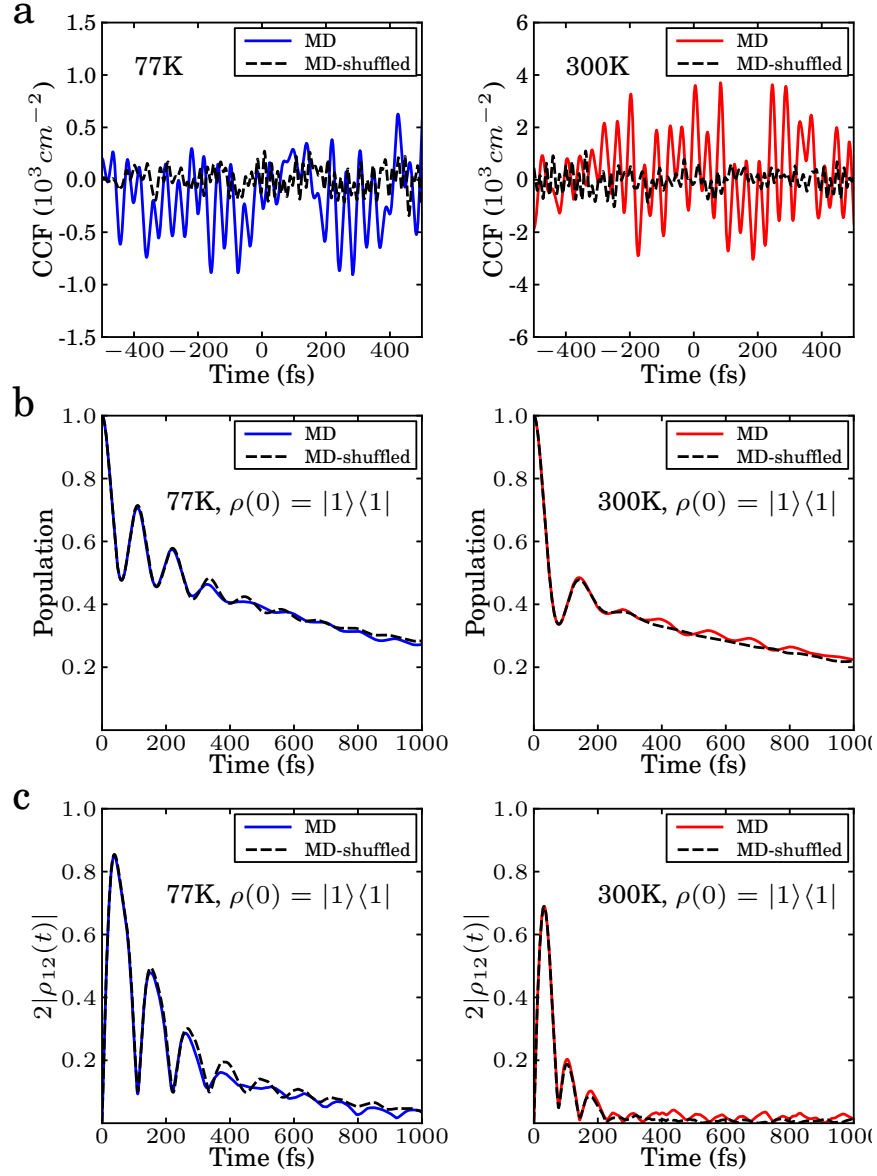
Figure 3.6: Panel **a**: Cross-correlation function of the original MD trajectory and a randomly shuffled trajectory between sites 1 and 2 at 77K and 300K. Panel **b**: Site 1 population dynamics of the original dynamics and the shuffled dynamics at 77K and 300K. **c**, The pairwise coherence between sites 1 and 2. Original and shuffled dynamics are virtually identical at both temperatures.

different parts of the MD trajectory. In this way, we could significantly reduce potential cross correlation between sites while maintaining the autocorrelation function of each site. As can be seen in Fig. 3.6, no noticeable difference between the original and shuffled dynamics is observed.

3.4   Conclusion

The theoretical and computational studies presented in this article show that the long-lived quantum coherence in the energy transfer process of the FMO complex of *Prosthecochloris aestuarii* can be simulated with the atomistic model of the protein-chromophore complex. Unlike traditional master equation approaches, we propagate in a quantum/classical framework both the system and the environment state to establish the connection between the atomistic details of the protein complex and the exciton transfer dynamics. Our method combines MD simulations and QM/MM with TDDFT/TDA to produce the time evolution of the excitonic reduced density matrix as an ensemble average of unitary trajectories.

The conventional assumption of unstructured and uncorrelated site energy fluctuations is not necessary for our method. No *ad hoc* parameters were introduced in our formalism. The temperature and decoherence time were extracted from the site energy fluctuation by the MD simulation of the protein complex. The simulated dynamics clearly shows the characteristic quantum wave-like population change and the long-lived quantum coherence during the energy transfer process in the biological environment. On this note it is worth mentioning that one has to be careful in the choice of force-field and in the method used to calculated site energies. In fact as

presented in Olbrich et al. [110] a completely different energy transfer dynamics was obtained by using the semiempirical ZINDO-S/CIS to determine site energies.

Moreover, we determined the correlations of the site energy fluctuations for each site and between sites through the direct simulation of the protein complex. The spectral density shows the influence of the characteristic vibrational frequencies of the FMO complex. This spectral density can be used as an input for quantum master equations or other many-body approaches to study the effect of the structured bath. The calculated linear absorption spectrum we obtained is comparable to the experimental result, which supports the validity of our method. The characteristic beating of exciton population and pairwise quantum coherence exhibit excellent agreement with the results obtained by the HEOM method. It is also worth noting the remarkable agreement of the dephasing timescales of the MD simulations, the HEOM approach, and experiment.

Recently, characterization of the bath in the LH2 [103, 104] and FMO [109] photosynthetic complexes were reported using MD simulation and quantum chemistry at room temperature. Those studies mostly focused on energy and spatial correlations across the sites, the linear absorption spectrum, and spectral density. The detailed study in [109] also suggests that spatial correlations are not relevant in the FMO dynamics.

This work opens the road to understanding whether biological systems employed quantum mechanics to enhance their functionality during evolution. We are planning to investigate the effects of various factors on the photosynthetic energy transfer process. These include: mutation of the protein residues, different chromophore

molecules, and temperature dependence. Further research in this direction could elucidate on the design principle of the biological photosynthesis process by nature, and could be beneficial for the discovery of more efficient photovoltaic materials and in biomimetics research.

Chapter 4

Path integral Monte Carlo with importance sampling for excitons interacting with arbitrary phonon bath environment

4.1 Introduction

Recent 2D non-linear spectroscopy experiments suggested the existence of long-lived quantum coherence during the electronic energy transfer process within the Fenna-Matthews-Olson complex of green sulfur bacteria, marine algae and plants even under physiological conditions [23, 25, 47, 111–113]. These results attracted a large amount of attention from theoretical physicists and chemists. The energy transfer process usually has been modeled as the dynamics of excitons coupled to a

phonon bath in thermal equilibrium within the single exciton manifold. This approximation leads to the famous spin-Boson Hamiltonian. The solution of this type of Hamiltonian has been studied extensively. For example, by assuming a certain relative magnitude between the reorganization energy and coupling terms, one can obtain quantum master equations valid in specific regimes[19, 67, 114]. Another approximation, the Haken-Strobl-Reineker model works in both the coherent and incoherent regimes, but incorrectly converges to the high temperature limit in the long time even at the low temperature [39, 40]. More recently, numerically exact approaches which interpolate both limits have been investigated and applied to many systems of interest. Two of the most popular methods are the hierarchical equation of motion [29, 87, 115] and the quasiadiabatic path integral method [116, 117]. These methods are being actively developed, improved, and applied to many systems of interests [58].

Although having been successful in many applications, many of the models described above have assumed the phonon bath to be a set of independent harmonic oscillators and encode all the complexity of the bath environment in the spectral density, which is essentially a frequency dependent distribution of exciton-phonon coupling. However, for studying the anharmonic effects of a very sophisticated bath environment, like the protein complexes of photosynthesis, being able to directly include the atomistic details of the bath structure into the exciton dynamics has a distinct advantage. In other words, approaches that can evaluate the influence functional first suggested by Feynman and Vernon [118] have more straightforward descriptions and are applicable to arbitrary systems. Evaluation of the exact influence functional for arbitrary environment requires the simulation of the full quantum dynamics, which is

still not practical with currently available computational resources. There have been several attempts to incorporate atomistic details of the large scale bath by combining the exciton dynamics and molecular dynamics simulations [32, 104, 119]. However, these theories are still in their early stages and the propagation scheme used does not satisfy some fundamental properties, like the detailed balance condition at finite temperature. In pursuit of more accurate theory, it is crucial to know the correct asymptotic behavior in the limit of infinite time. In this context, we decided to explore the numerically exact reduced density matrix in a finite temperature using path integral Monte Carlo [120–123] method. Recently, Moix *et al* applied path integral Monte Carlo for the equilibrium reduced density matrix of the FMO complex within the framework of open quantum systems [124].

4.2   Theory

4.2.1   Path Integral Formulation of the Reduced Thermal Density Matrix

We want to evaluate the reduced density matrix of an excitonic system coupled to phonons on arbitrary Born-Oppenheimer surfaces at a finite temperature. For photosynthetic energy transfer, we usually restrict the excitons to be within the single exciton manifold because at normal light intensity, in average, one photon is present at a given time in the complexes of interest. However, the formulation itself is not limited to the single exciton manifold. The Hamiltonian operator for such a system

can be written as

$$\hat{H} = \underbrace{\sum_m \int d\boldsymbol{R} \; [V_m(\boldsymbol{R}) - V_g(\boldsymbol{R})] \, |m\rangle\langle m| \otimes |\boldsymbol{R}\rangle\langle\boldsymbol{R}| + \sum_{m\neq n} \int d\boldsymbol{R} \; J_{mn}(\boldsymbol{R}) |m\rangle\langle n| \otimes |\boldsymbol{R}\rangle\langle\boldsymbol{R}|}_{\hat{H}_{\text{exc}}=\hat{H}_S+\hat{H}_{SB}}$$

$$+ \underbrace{|\boldsymbol{1}\rangle\langle\boldsymbol{1}| \otimes \left[\hat{T} + \int d\boldsymbol{R} \; V_g(\boldsymbol{R})|\boldsymbol{R}\rangle\langle\boldsymbol{R}|\right]}_{\hat{H}_B}. \tag{4.1}$$

The Hamiltonian was written in terms of the diabatic basis $|m, \boldsymbol{R}\rangle \equiv |m\rangle \otimes |\boldsymbol{R}\rangle$, where m is the index for the exciton state and R is the phonon coordinate. $V_g(\boldsymbol{R})$ is the potential energy surface (PES) of the phonons in the electronic ground state and $V_m(\boldsymbol{R})$ is the PES of the phonons in the mth exciton state. $\hat{T}$ is the kinetic operator of the phonons defined as $\hat{T} = -\frac{\hbar^2}{2}\mathcal{M}^{-1}\nabla^2$, where $\mathcal{M}$ is the mass tensor of the phonons. This expression is generally applicable to any molecular system with multiple potential energy surfaces. The reduced thermal density matrix ρ_S is defined as the partial trace of the full thermal density matrix with respect to the bath degrees of freedom:

$$\rho_S = \frac{1}{Z(\beta)}\text{Tr}_{\text{B}} \exp\left(-\beta\hat{H}\right)$$

$$= \frac{1}{Z(\beta)} \int d\boldsymbol{R}_0 \; \langle\boldsymbol{R}_0| \exp\left(-\beta\hat{H}\right) |\boldsymbol{R}_0\rangle, \tag{4.2}$$

where $Z(\beta)$ is the partition function of the total system. We proceed by relying on the following identity:

$$\langle \boldsymbol{R}_0 | \exp(-\beta \hat{H}) | \boldsymbol{R}_0 \rangle = \langle \boldsymbol{R}_0 | \left\{ \exp\left(-\frac{\beta \hat{H}}{M}\right) \right\}^M | \boldsymbol{R}_0 \rangle$$

$$= \int d\boldsymbol{R}_1 \int d\boldsymbol{R}_2 \cdots \int d\boldsymbol{R}_{M-1}$$

$$\times \langle \boldsymbol{R}_0 | \exp\left(-\frac{\beta \hat{H}}{M}\right) | \boldsymbol{R}_{M-1} \rangle \langle \boldsymbol{R}_{M-1} | \exp\left(-\frac{\beta \hat{H}}{M}\right) | \boldsymbol{R}_{M-2} \rangle$$

$$\times \cdots \times \langle \boldsymbol{R}_2 | \exp\left(-\frac{\beta \hat{H}}{M}\right) | \boldsymbol{R}_1 \rangle \langle \boldsymbol{R}_1 | \exp\left(-\frac{\beta \hat{H}}{M}\right) | \boldsymbol{R}_0 \rangle. \quad (4.3)$$

For any positive integer M, the expression above is exact. When the Trotter decomposition is applied, an imaginary timestep $\tau \equiv \frac{\beta \hbar}{M}$ is usually defined for convenience. Then, the thermal density matrix can be interpreted as an imaginary time evolution. In the limit of an infinitesimal imaginary timestep, the Trotter decomposition converges to the exact result,

$$\langle \boldsymbol{R}_1 | \exp\left(-\frac{\beta \hat{H}}{M}\right) | \boldsymbol{R}_0 \rangle = \langle \boldsymbol{R}_1 | \exp\left(-\tau \hat{H}/\hbar\right) | \boldsymbol{R}_0 \rangle$$

$$= \langle \boldsymbol{R}_1 | e^{-\tau \hat{H}_{\text{exc}}/2\hbar} e^{-\tau \hat{H}_B/\hbar} e^{-\tau \hat{H}_{\text{exc}}/2\hbar} | \boldsymbol{R}_0 \rangle + O(\tau^3)$$

$$= \int d\boldsymbol{R}_2 \int d\boldsymbol{R}_3 \ \langle \boldsymbol{R}_1 | e^{-\tau \hat{H}_{\text{exc}}/2\hbar} | \boldsymbol{R}_3 \rangle$$

$$\times \langle \boldsymbol{R}_3 | e^{-\tau \hat{H}_B/\hbar} | \boldsymbol{R}_2 \rangle \langle \boldsymbol{R}_2 | e^{-\tau \hat{H}_{\text{exc}}/2\hbar} | \boldsymbol{R}_0 \rangle + O(\tau^3). \quad (4.4)$$

Subsequently, we will recast the system part of $\hat{H}_{\text{exc}}$ as a single matrix to simplify

the notation,

$$\hat{H}_{\text{exc}} = \sum_{m,n} \int d\boldsymbol{R} \; E_{mn}(\boldsymbol{R})|m\rangle\langle n| \otimes |\boldsymbol{R}\rangle\langle\boldsymbol{R}|,$$

$$E_{mm}(\boldsymbol{R}) = \begin{cases} V_m(\boldsymbol{R}) - V_g(\boldsymbol{R}) & for \quad m = n, \\[2mm] J_{mn}(\boldsymbol{R}) & for \quad m \neq n. \end{cases} \tag{4.5}$$

With the single exciton manifold assumption, E_{mm} corresponds to the optical gap of the m-th site. Now, the three terms in the integrand of the Eq. 4.4 can be written without Dirac notation,

$$\langle\boldsymbol{R}_1|e^{-\tau\hat{H}_{\text{exc}}/2\hbar}|\boldsymbol{R}_3\rangle = \delta(\boldsymbol{R}_1 - \boldsymbol{R}_3)e^{-\tau E(\boldsymbol{R}_3)/2\hbar},$$

$$\langle\boldsymbol{R}_3|e^{-\tau\hat{H}_B/\hbar}|\boldsymbol{R}_2\rangle = (4\pi\tau|\lambda|)^{-1/2}e^{-\tau V_g(\boldsymbol{R}_3)/2\hbar}e^{-(\boldsymbol{R}_3-\boldsymbol{R}_2)^T\lambda^{-1}(\boldsymbol{R}_3-\boldsymbol{R}_2)/4\tau}e^{-\tau V_g(\boldsymbol{R}_2)/2\hbar}$$

$$+ O(\tau^3),$$

$$\langle\boldsymbol{R}_2|e^{-\tau\hat{H}_{\text{exc}}/2\hbar}|\boldsymbol{R}_0\rangle = \delta(\boldsymbol{R}_2 - \boldsymbol{R}_0)e^{-\tau E(\boldsymbol{R}_0)/2\hbar}, \tag{4.6}$$

where $\lambda \equiv \frac{\hbar\mathcal{M}^{-1}}{2}$. By the Eq. 4.4 and Eq. 4.6,

$$\langle\boldsymbol{R}_1|\exp\left(-\frac{\beta\hat{H}}{M}\right)|\boldsymbol{R}_0\rangle = (4\pi\tau|\lambda|)^{-1/2}e^{-\tau V_g(\boldsymbol{R}_1)/2\hbar}e^{-(\boldsymbol{R}_1-\boldsymbol{R}_0)^T\lambda^{-1}(\boldsymbol{R}_1-\boldsymbol{R}_0)/4\tau}e^{-\tau V_g(\boldsymbol{R}_0)/2\hbar}$$

$$\times e^{-\tau E(\boldsymbol{R}_1)/2\hbar}e^{-\tau E(\boldsymbol{R}_0)/2\hbar} + O(\tau^3). \tag{4.7}$$

Note that Eq. 4.7 is a matrix with the same dimension as the reduced density matrix

of the system. Substituting Eq. 4.7 to Eq. 4.2, we obtain

$$
\rho_S = \frac{1}{Z(\beta)} \int d\boldsymbol{R}_0 \int d\boldsymbol{R}_1 \cdots \int d\boldsymbol{R}_{M-1}
$$

$$
\times\, e^{-\tau E(\boldsymbol{R}_0)/2\hbar} e^{-\tau E(\boldsymbol{R}_{M-1})/\hbar} \cdots e^{-\tau E(\boldsymbol{R}_1)/\hbar} e^{-\tau E(\boldsymbol{R}_0)/2\hbar}
$$

$$
\times\, e^{-\tau V_g(\boldsymbol{R}_0)/\hbar} e^{-\tau V_g(\boldsymbol{R}_1)/\hbar} \cdots e^{-\tau V_g(\boldsymbol{R}_{M-1})/\hbar}
$$

$$
\times\, e^{-(\boldsymbol{R}_0-\boldsymbol{R}_{M-1})^T \lambda^{-1}(\boldsymbol{R}_0-\boldsymbol{R}_{M-1})/4\tau} e^{-(\boldsymbol{R}_{M-1}-\boldsymbol{R}_{M-2})^T \lambda^{-1}(\boldsymbol{R}_{M-1}-\boldsymbol{R}_{M-2})/4\tau}
$$

$$
\times \cdots \times e^{-(\boldsymbol{R}_1-\boldsymbol{R}_0)^T \lambda^{-1}(\boldsymbol{R}_1-\boldsymbol{R}_0)/4\tau}
$$

$$
= \int d\boldsymbol{R}_0 \int d\boldsymbol{R}_1 \cdots \int d\boldsymbol{R}_{M-1}
$$

$$
\times \underbrace{\frac{K}{Z(\beta)} e^{-\tau E(\boldsymbol{R}_0)/2\hbar} e^{-\tau E(\boldsymbol{R}_{M-1})/\hbar} \cdots e^{-\tau E(\boldsymbol{R}_1)/\hbar} e^{-\tau E(\boldsymbol{R}_0)/2\hbar}}_{\rho_{\mathrm{PIMC}}(\boldsymbol{R}_0,\cdots,\boldsymbol{R}_{M-1})}
$$

$$
\times \underbrace{\frac{1}{K} e^{-\beta V_{\mathrm{PIMC}}(\boldsymbol{R}_0,\boldsymbol{R}_1,\cdots,\boldsymbol{R}_{M-1})}}_{f_g(\boldsymbol{R}_0,\cdots,\boldsymbol{R}_{M-1})}, \tag{4.8}
$$

where,

$$
V_{\mathrm{PIMC}}(\boldsymbol{R}_0, \boldsymbol{R}_1, \cdots, \boldsymbol{R}_{M-1}) = \frac{1}{M} \sum_{i=0}^{M-1} V_g(\boldsymbol{R}_i)
$$

$$
+ \sum_{i=0}^{M-1} \frac{M}{2\beta^2\hbar^2} \{\boldsymbol{R}_i - \boldsymbol{R}_{\mathrm{mod}(i+1,M)}\}^T \mathcal{M} \{\boldsymbol{R}_i - \boldsymbol{R}_{\mathrm{mod}(i+1,M)}\}.
$$

$$
\tag{4.9}
$$

The expressions above show that the reduced thermal density matrix ρ_S can be evaluated as an expectation value of $\rho_{\mathrm{PIMC}}(\boldsymbol{R}_0,\cdots,\boldsymbol{R}_{M-1})$ where the joint probability density function of the M N-dimensional random variables $(\boldsymbol{R}_0,\cdots,\boldsymbol{R}_{M-1})$ is f_g. This type of multidimensional integral can be efficiently evaluated using Monte Carlo integration. Because $f_g(\boldsymbol{R}_0,\cdots,\boldsymbol{R}_{M-1})$ is invariant to cyclic permutation of the phonon coordinate, usually the averaged estimator ρ_{PIMC} over the cyclic permutation

is used in the actual Monte Carlo evaluation:

$$\rho_{\overline{\text{PIMC}}}(\boldsymbol{R}_0, \boldsymbol{R}_1, \cdots, \boldsymbol{R}_{M-1}) = \frac{1}{M} \sum_{i=0}^{M-1} \rho_{\text{PIMC}}(\boldsymbol{R}_i, \boldsymbol{R}_{\text{mod}(i+1,M)}, \cdots, \boldsymbol{R}_{\text{mod}(i+M-1,M)}).$$

(4.10)

4.2.2 Population-Normalized Estimator and Importance Sampling

In the previous approach described in Eq. 4.8, the phonon coordinates are sampled according the electronic ground state PES. The estimator should converge to the target quantity in the long time limit, taking into account the discretization error. As long as $f_g(\boldsymbol{R}_0, \cdots, \boldsymbol{R}_{M-1})$ is positive definite everywhere in the phonon space, the sampling efficiency depends on the selection of the probability density. Obviously, the actual distribution of the phonon coordinate depends heavily on the excited state PES. Therefore, the Monte Carlo points coordinates sampled according to the reduced dynamics of the bath by taking the partial trace with respect to the *exciton degrees of freedom*, as explored in multiple surface path integral Monte Carlo approaches, are expected to give the better estimates. This choice of the probability density reweights the estimator in the following way:

$$f_I(\boldsymbol{R}_0, \cdots, \boldsymbol{R}_{M-1}) = \text{Tr}_{\text{S}} \left[\rho_{\overline{\text{PIMC}}}(\boldsymbol{R}_0, \cdots, \boldsymbol{R}_{M-1})\right] f_g(\boldsymbol{R}_0, \cdots, \boldsymbol{R}_{M-1}),$$

$$\rho_I(\boldsymbol{R}_0, \cdots, \boldsymbol{R}_{M-1}) = \frac{\rho_{\overline{\text{PIMC}}}(\boldsymbol{R}_0, \cdots, \boldsymbol{R}_{M-1})}{\text{Tr}_{\text{S}} \left[\rho_{\overline{\text{PIMC}}}(\boldsymbol{R}_0, \cdots, \boldsymbol{R}_{M-1})\right]}.$$

(4.11)

In the expression above, we call $\rho_I(\boldsymbol{R}_0, \cdots, \boldsymbol{R}_{M-1})$ the population normalized estimator for the reduced density matrix because the sum of its populations is always constrained to be 1. The effective energy gap term of $-\frac{1}{\beta} \log \text{Tr} \rho_{\overline{\text{PIMC}}}(\boldsymbol{R}_0, \cdots, \boldsymbol{R}_{M-1})$

was added to the Eq. 4.9 to enable the phonons follow the excited state dynamics depending on the exciton state ρ_S. For the estimator of the reduced density matrix in Eq. 4.8, the normalization must obtained by the estimates of its diagonal elements, leading to more uncertainties in the coherence. However, the population-normalized estimator preserves the correct normalization by construction, and does not suffer from any additional uncertainty.

Local gradient information can improve the efficiency and scaling of the sampling procedure by means of a gradient-based approach such as the Metropolis-adjusted Langevin algorithm (MALA). [125, 126] However, the exact closed form of the gradient of the effective energy gap term, $\log \mathrm{Tr}_S \rho_{\overline{\mathrm{PIMC}}}(\boldsymbol{R}_0, \cdots, \boldsymbol{R}_{M-1})$ can only be expressed as a function of a power series of matrices. Nevertheless, with the following approximation:

$$\sum_{k=0}^{n} A^k B A^{n-k} \approx \sum_{k=0}^{n} \frac{1}{2^n} \binom{n}{k} A^k B A^{n-k}, \tag{4.12}$$

an accurate approximated of the gradient can be obtained and employed in the sam-

pling procedure,

$$
\begin{aligned}
\frac{\partial}{\partial R_{ij}} \log \mathrm{Tr_S}\left[\rho_{\overline{\mathrm{PIMC}}}(\boldsymbol{R}_0, \cdots, \boldsymbol{R}_{M-1})\right] &= \frac{\mathrm{Tr_S}\left[\frac{\partial}{\partial R_{ij}}\rho_{\overline{\mathrm{PIMC}}}(\boldsymbol{R}_0, \cdots, \boldsymbol{R}_{M-1})\right]}{\mathrm{Tr_S}\left[\rho_{\overline{\mathrm{PIMC}}}(\boldsymbol{R}_0, \cdots, \boldsymbol{R}_{M-1})\right]} \\
&\approx \frac{\mathrm{Tr_S}\left[-\frac{\tau}{2\hbar}\frac{\partial E(\boldsymbol{R}_i)}{\partial R_{ij}}\rho_{\overline{\mathrm{PIMC}}}(\boldsymbol{R}_0, \cdots, \boldsymbol{R}_{M-1})\right]}{\mathrm{Tr_S}\left[\rho_{\overline{\mathrm{PIMC}}}(\boldsymbol{R}_0, \cdots, \boldsymbol{R}_{M-1})\right]}, \\
\nabla_i \log f_g(\boldsymbol{R}_0, \cdots, \boldsymbol{R}_{M-1}) &= -\frac{\beta}{M}\nabla_i V_g(\boldsymbol{R}_i) \\
&\quad + \frac{M}{2\beta\hbar^2}\mathcal{M}(\boldsymbol{R}_{\mathrm{mod}(i+1,M)} + \boldsymbol{R}_{\mathrm{mod}(i-1,M)} - 2\boldsymbol{R}_i), \\
\mu_i(\boldsymbol{R}_0, \cdots, \boldsymbol{R}_{M-1}) &= \frac{\mathrm{Tr_S}\left[-\frac{\tau}{2\hbar}\frac{\partial E(\boldsymbol{R}_i)}{\partial R_{ij}}\rho_{\overline{\mathrm{PIMC}}}(\boldsymbol{R}_0, \cdots, \boldsymbol{R}_{M-1})\right]}{\mathrm{Tr_S}\left[\rho_{\overline{\mathrm{PIMC}}}(\boldsymbol{R}_0, \cdots, \boldsymbol{R}_{M-1})\right]} \\
&\quad + \nabla_i \log f_g(\boldsymbol{R}_0, \cdots, \boldsymbol{R}_{M-1}) \\
&\approx \nabla_i \log f_I(\boldsymbol{R}_0, \cdots, \boldsymbol{R}_{M-1}). \tag{4.13}
\end{aligned}
$$

Here, ∇_i is the gradient operator with respect to $\boldsymbol{R}_i$.

Note that if we choose an appropriate Metropolis criterion, no bias in the distribution is introduced even with the approximate gradient [127]. Firstly, a trial move $\boldsymbol{R}'_i$ obtained by

$$
\boldsymbol{R}'_i = \boldsymbol{R}_i + \mu_i(\boldsymbol{R}_0, \cdots, \boldsymbol{R}_{M-1})\Delta t + \xi_i\sqrt{\Delta t}, \tag{4.14}
$$

where Δt is the timestep for the Monte Carlo step and ξ_i is a N-dimensional vector of independent standard Gaussian random variables. Then, R'_i is probabilistically accepted according to the acceptance ratio,

$$
\frac{f_I(\boldsymbol{R}'_0, \cdots, \boldsymbol{R}'_{M-1})}{f_I(\boldsymbol{R}_0, \cdots, \boldsymbol{R}_{M-1})} \times \frac{\prod_{i=0}^{M-1}\exp\left[-\frac{|\boldsymbol{R}'_i - \{\boldsymbol{R}_i + \mu_i(\boldsymbol{R}_0, \cdots, \boldsymbol{R}_{M-1})\}|^2}{2\Delta t}\right]}{\prod_{i=0}^{M-1}\exp\left[-\frac{|\boldsymbol{R}_i - \{\boldsymbol{R}'_i + \mu_i(\boldsymbol{R}'_0, \cdots, \boldsymbol{R}'_{M-1})\}|^2}{2\Delta t}\right]}. \tag{4.15}
$$

The Monte Carlo timestep Δt is only a tunable parameter for the Monte Carlo sampling procedure and not related to the physics of the simulated system.

Parameters	Value
k_{11}	4×10^{-5}
k_{22}	3.2×10^{-5}
x_{11}	7
x_{22}	10.5
ε_{11}	0
ε_{22}	2.2782×10^{-5}
c	5×10^{-5}
α	0.4
x_{12}	8.75
m	3.6743×10^3

Table 4.1: Summary of the parameters for the model system by Alexander *et al* [128]. All values are given in atomic units.

4.3 Application

4.3.1 Alexander's 1D Test Model

Our formulation is equivalent to the multiple electronic state extension of matrix multiplication path integral (MMPI) method of Alexander [120, 128] when the population normalized estimator is chosen and only the vibrational degrees of freedom are considered. Therefore, the 1D model employed in Ref. [128] was calculated to test the validity of our method. The elements of the electronic Hamiltonian in this model are given by,

$$V_{11}(x) = \frac{1}{2}k_{11}(x - x_{11})^2 + \varepsilon_{11},$$

$$V_{22}(x) = \frac{1}{2}k_{22}(x - x_{22})^2 + \varepsilon_{22},$$

$$V_{12}(x) = c \exp\left[-\alpha(x - x_{12})^2\right], \tag{4.16}$$

The total nuclear probability density evaluated as histograms from the Metropolis random walk and MALA simulations are compared to the grid-based result from

93

Alexander *et al.* [128] in Fig. 4.1. The distributions converged to the exact probability density after 2×10^7 steps with 8 beads at both temperatures of 8K and 30K.

4.3.2 Model of a Chromophore Heterodimer with Displaced Harmonic Oscillators

To test the proposed method, a system of two chromophores in a photosynthetic complex was modeled using displaced harmonic oscillator model. In this model, the ground and excited electronic states of the monomer are modeled as harmonic oscillators with different displacement, but the same harmonic constant [67]. The thermal reduced density matrix was calculated within the single exciton manifold. The Hamiltonian for this model is then given as follows:

$$
V_g(x_1, x_2) = \frac{1}{2}(k_1 x_1^2 + k_2 x_2^2),
$$

$$
V_e(x_1, x_2) = \begin{pmatrix} \frac{1}{2}k_1\{(x_1 - d_1)^2 - x_1^2\} + \varepsilon_1 & J \\ J & \frac{1}{2}k_2\{(x_2 - d_2)^2 - x_2^2 + \varepsilon_2\} \end{pmatrix},
$$

$$
\mathcal{M} = \begin{pmatrix} m_1 & 0 \\ 0 & m_2 \end{pmatrix}. \tag{4.17}
$$

Some of the parameters were set according to our molecular dynamics/quantum chemistry calculation of the FMO complex [32]. The parameter values are listed in table 4.2.

The model system was simulated at seven different temperatures ranging from 30K to 300K with a number of beads (discretization number) of 4, 8, 16, 32 and 64. The number of timesteps propagated in each simulation was 4×10^7. The value of
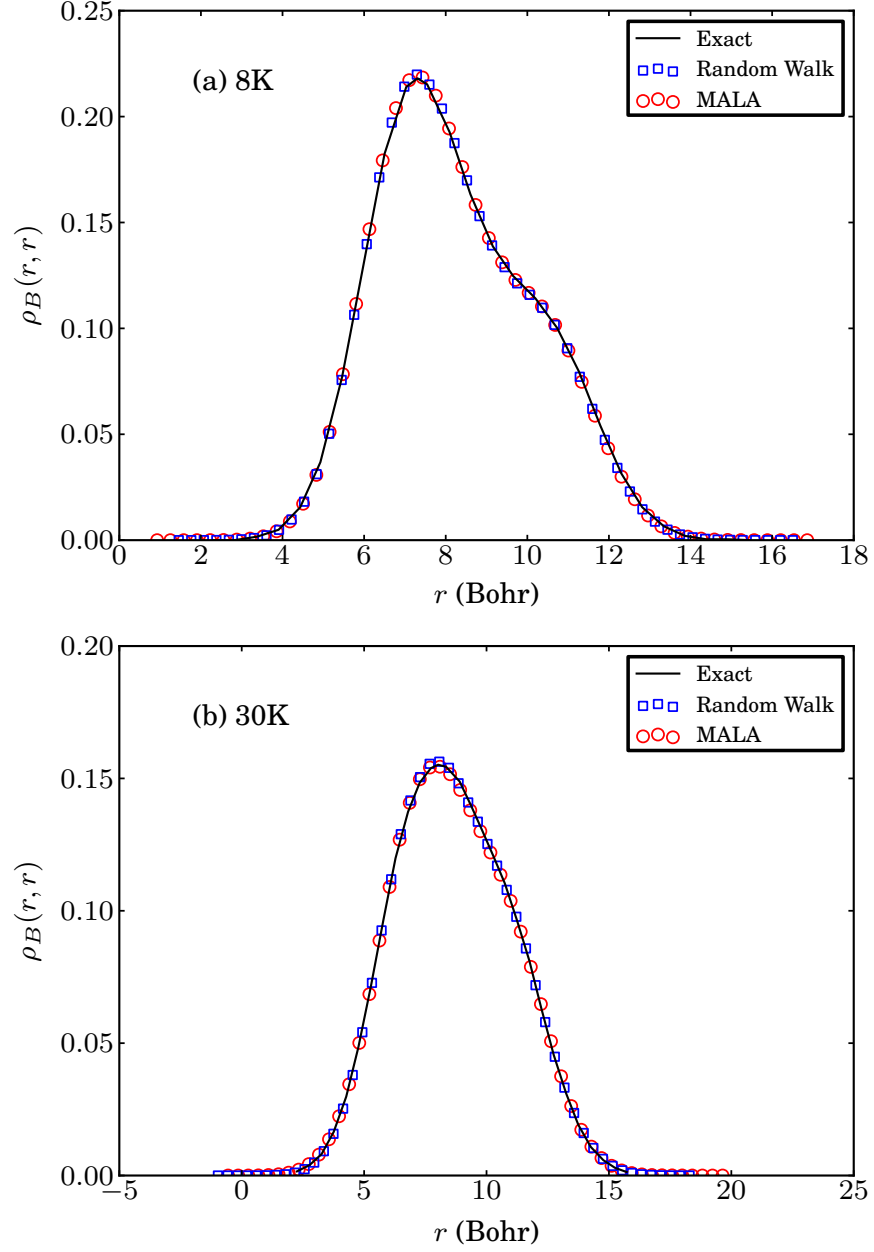
Figure 4.1: The estimated nuclear probability densities of Alexander's model [128] at (a) 8K and (b) 30K. For path integral Monte Carlo simulations, densities were obtained by histograms with 50 bins. The discretization number of 8 was enough to converge to the exact probability densitiies.

Parameter	Value
k_1	2.227817×10^{-3}
k_2	2.227817×10^{-3}
d_1	3.00000
d_2	2.00000
ε_1	8.064745×10^{-2}
ε_2	7.976238×10^{-2}
J	-4.738588×10^{-4}
m_1	3.418218×10^{6}
m_2	3.418218×10^{6}

Table 4.2: Summary of the parameters for the displaced harmonic oscillator model used in Sec. 4.3.2. All values are given in atomic units.

each timestep was tuned so that the acceptance ratio of the MALA run is close to 0.574, and 0.234 for the Metropolis random walk as maintaining these acceptance ratio is known to provide most efficient sampling [126]. We used non-overlapping batch means [129] with a batch size of 10^6 to estimate the standard error of the correlated samples. The batch size was adjusted so that the null hypothesis of uncorrelated batches was not rejected by using Ljung-Box test [130] at a significance level of 5%.

As shown in Fig. 4.2, the standard error of the simulation decreases modestly as the number of Monte Carlo steps increases. Fig. 4.3 shows the temperature dependence of the estimates of reduced density matrix elements as a function of various discretization numbers using MALA. Although the Metropolis random walk simulation gives a smaller confidence interval for the 4 bead case, MALA provides better estimates as the dimension of the sample space increases. The Metropolis random walk result is given in Fig. 4.4. While the population of the low energy site decreases as the temperature increases, the quantum coherence does not monotonically decrease. We believe that this pheonomenon is an artifact of an insufficient discretiza-
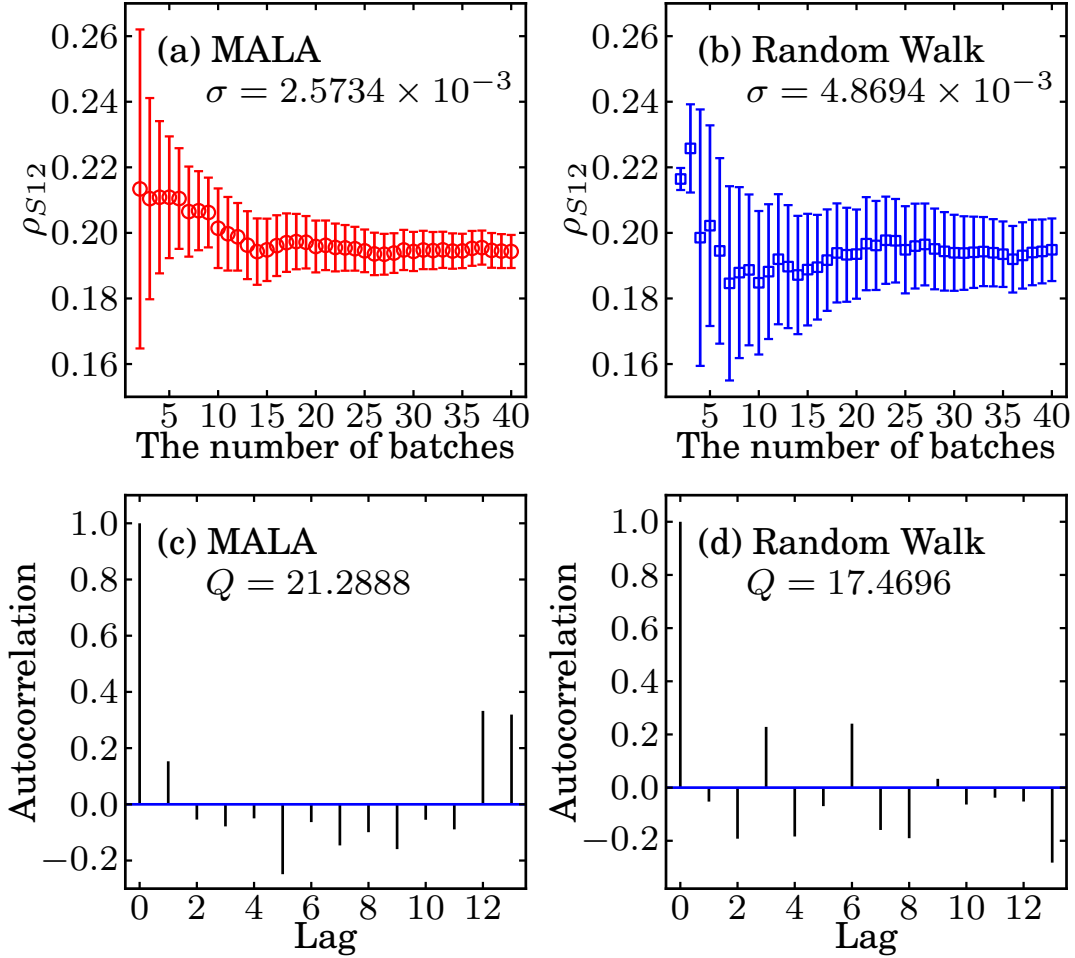
Figure 4.2: Estimates of (1,2) matrix elements of the thermal reduced density matrix evaluated using MALA and Metropolis random walk at 77K with 64 beads. MALA estimate has a smaller confidence interval thus a more accurate estimate than that of the Metropolis random walk. The error bar indicates the 95% confidence interval evaluated with the batch means. The 0.95 quantile of the χ^2 distribution with 13 degrees of freedom is 22.362 and both Ljung-Box statistics (Q) are smaller. Thus, the uncorrelation hypothesis is not rejected in both cases at the 5% significance level.

tion number at low temperatures. As can be seen in Fig. 4.3, 64 or more beads are needed for the coherence to converge at 77K, while 16 beads are enough at 300K with acceptable accuracy. This is a well known limition of imaginary time path integral Monte Carlo simulations. Figure 4.5 shows the probability density function of the phonon coordinate at 77K and 300K. The population difference in the reduced density matrix is reflected to the difference in the probability mass of the two diabatic potential energy minimum at $(3, 0)$ and $(0, 2)$.

4.4 Conclusion

We explore a method for obtaining the thermal reduced density matrix of an exciton system coupled to an arbitrary phonon bath for path integral Monte Carlo simulation. Note that our scheme is closely related to the path integral Monte Carlo simulation for nonadiabatic systems for vibrational coherence [128, 131, 132]. Although the phonon state can be obtained as a byproduct, we mainly focused on the evaluation of the reduced density matrix of the excitonic system to explore the asymptotic behavior of the populations and coherences in this paper. In addition, we implemented an importance sampling scheme for better spatial scaling and sampling efficiency. Although the path integral Monte Carlo cannot evaluate the real time evolution of density matrices, the method gives the exact asymptotic values with all quantum effects from both the system and bath environments if a sufficient number of beads are used. We believe that in some of the cases where the bath has a nontrivial coupling to the system, or the non-Markovianity of the bath manifests very strongly, treating the environment around the system of interest as a set of harmonic oscillators

Figure 4.3: Estimates of matrix elements of the thermal reduced density matrix evaluated at 30K, 50K, 77K, 140K, 225K and 300K with different discretization numbers of 4, 8 and 16 using MALA. (a) is the (1,1) element, (b), (c) and (d) are (1,2), (2,1) and (2,2) elements, respectively. The error bar indicates the 95% confidence interval evaluated with the batch means.
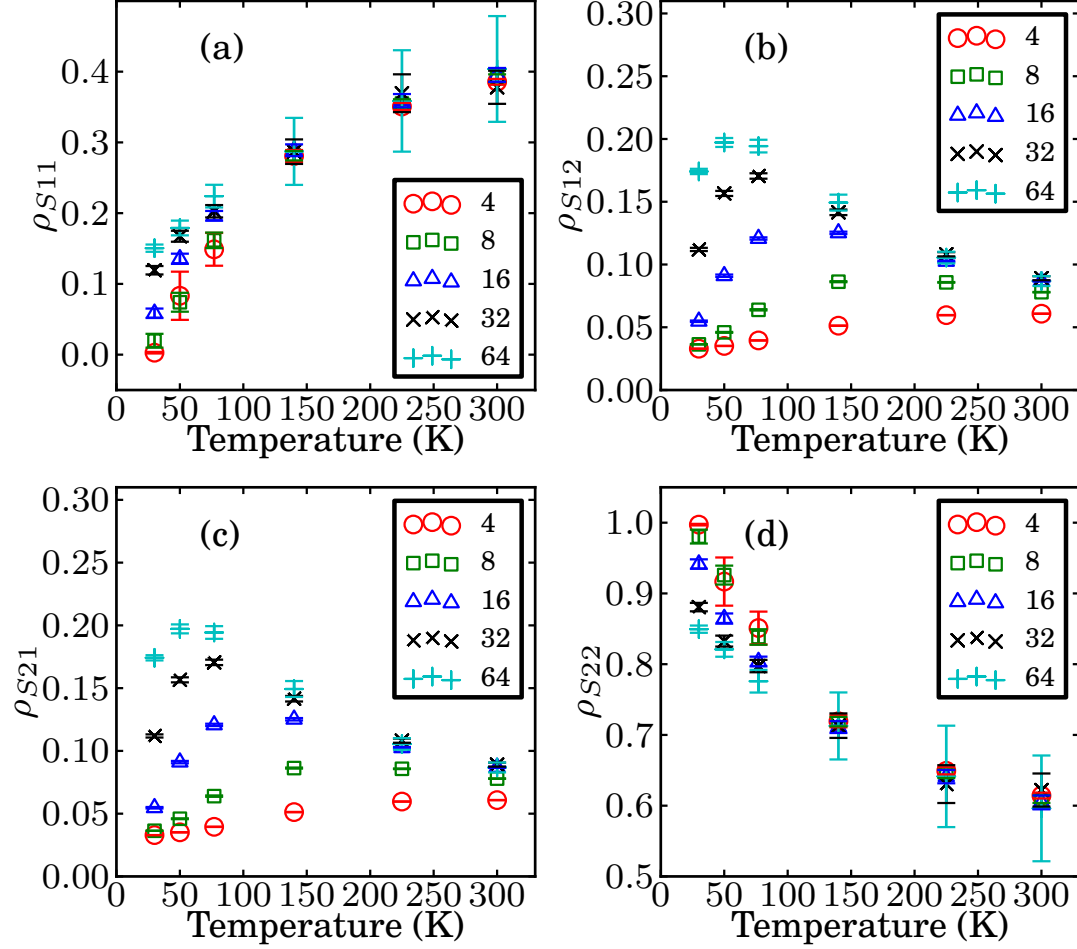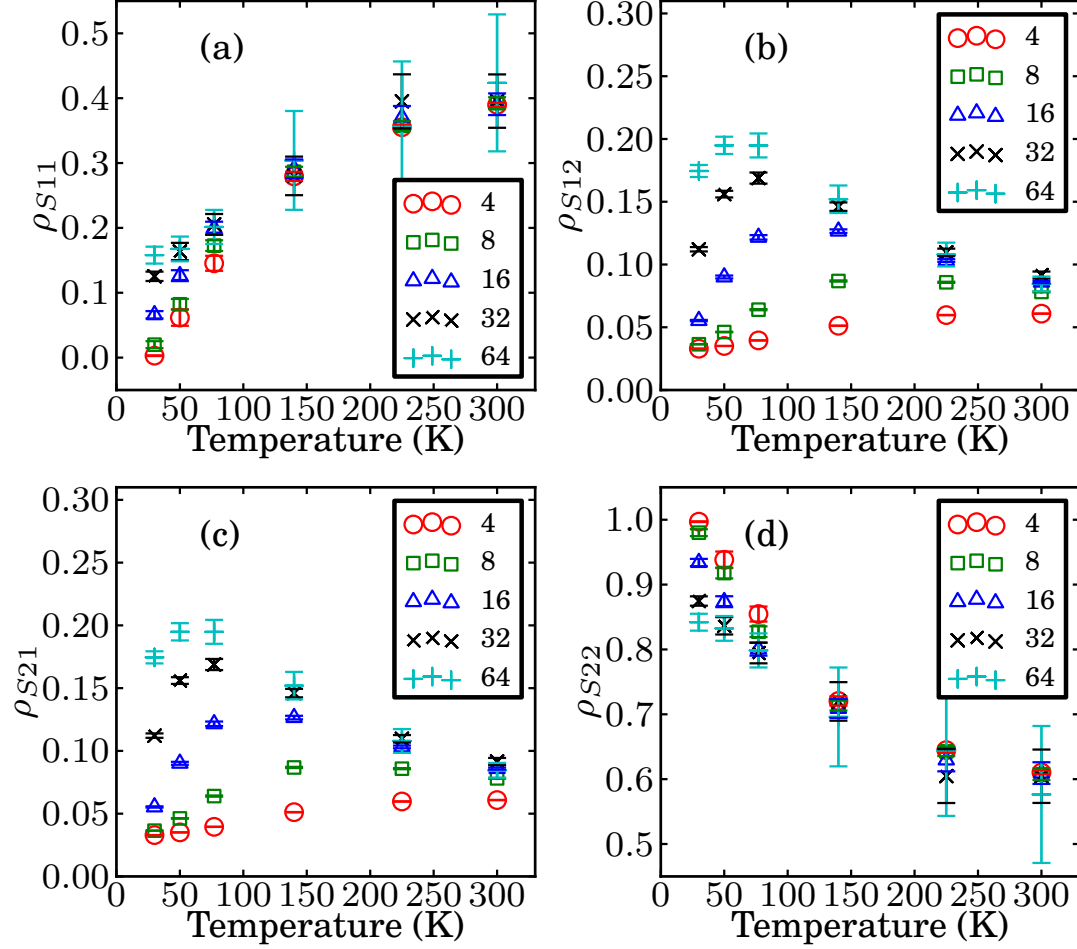
Figure 4.4: Estimates of matrix elements of the thermal reduced density matrix evaluated at 30K, 50K, 77K, 140K, 225K and 300K with different discretization numbers of 4, 8 and 16 using random walk Metropolis. (a) is the (1,1) element, (b), (c) and (d) are (1,2), (2,1) and (2,2) elements, respectively. The error bar indicates the 95% confidence interval evaluated with the batch means.
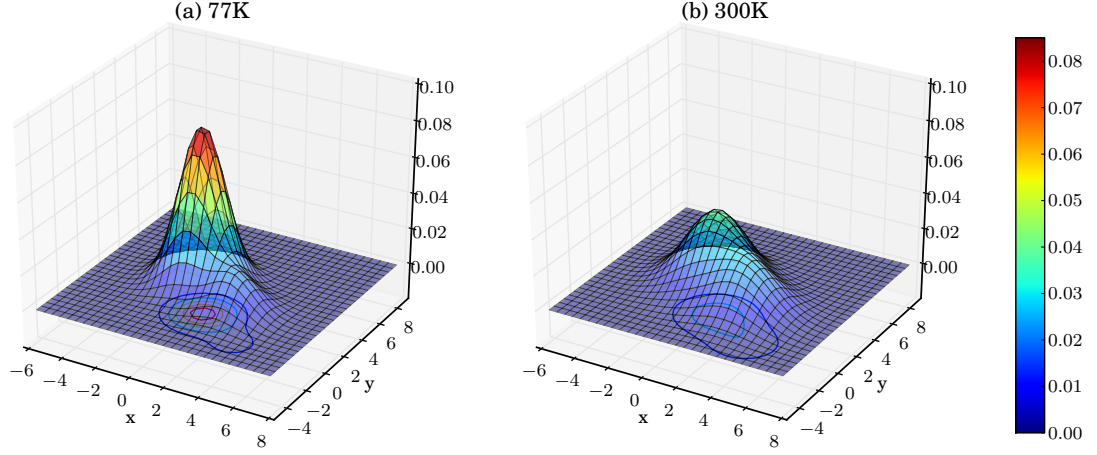
Figure 4.5: The phonon probability density function evaluated at (a) 77K and (b) 300K with 16 beads using MALA. At the lower temperature, the contribution of the exciton with lower energy at $(0, 2)$ becomes larger. Therefore, the population differenece becomes more distinct, as can be seen in the temperature dependence of the exciton population in Fig. 4.3.

is not sufficient. If this is the case, the system should be studied in its entirety. We

are trying to develop a real time propagation scheme to treat the system exactly, and

the bath semiclassically. The method studied in this paper offers a foundation for it

by providing the correct asymptotic behaviors.

Part II

Simulations of Molecular Systems

and Applications

Chapter 5

First-principles semiclassical initial value representation molecular dynamics

5.1 Introduction

Algorithms for the simulation of molecular dynamics belong to the fundamental toolset of modern theoretical chemical physics. Classical simulation methods are able to study systems with up to millions of particles but are unable to describe quantum effects such as tunelling and delocalization. Exact quantum mechanical methods are restricted to a few quantum particles, especially when pre-computed analytical potential energy surfaces (PES) are employed.

First-principles molecular dynamics (FPMD) algorithms have been introduced as an alternative to the pre-calculation of the PES. FPMD avoids any source of error

originated from the fitting of the PES. This is particularly true for many degrees of freedom, where the fitting procedure might not represent the many-dimensional surface accurately. In this family of methods, the potential and its derivatives are calculated *on-the-fly* as the dynamical simulation progresses and are directly obtained from electronic structure calculations. In the Born-Oppenheimer molecular dynamics (BOMD) approach, the electronic structure calculations for a given simulation step are converged based on previous step information. This approach can lead to systematic energy drifts and several methods have been proposed to avoid this effect [133]. Alternatively, extended Lagrangian molecular dynamics approaches (ELMD) [134–137] involve the propagation of nuclear and electronic degrees of freedom simultaneously. The electronic degrees of freedom are assigned to classical variables that are propagated using classical equations of motion and these can be expanded in terms of plane waves [134], Gaussian functions [136] or real-space grids [137]. Usually ELMD propagation is computationally more efficient, however questions have raised on whether the resultant energy surface remains close to the actual Born-Oppenheimer one and about disturbing dependencies on the fictitious electronic masses [136, 138].

While the evaluation of the potential *on-the-fly* can be easily integrated with classical simulations, the delocalized nature of quantum mechanical propagation has led to the development of many alternative approaches for the simulation of quantum dynamics. For example, the path-integral centroid molecular dynamics approach [139] includes quantum nuclear effects employing an extended Lagrangian. Alternatively, in the variational multi-configuration Gaussian wavepacket method (vMCG) [140] the quantum wavepackets are represented by fixed-width Gaussian functions for which the

potential is approximated to be locally harmonic. Other approaches introduce a mean field approximation and then update the dynamics in a time-dependent self-consistent fashion [141, 142].

Semiclassical molecular dynamics methods [143–152] are based on classical trajectories and therefore are amenable for carrying out *on-the-fly* calculation of the potential. The benefits of calculating the potential only when needed have been suggested by Heller and co-workers [152, 153]. In between formally exact quantum methods and classical dynamics, semi-classical methods include quantum effects approximately. Two representative semi-classical approaches are the coupled coherent states (CCS) technique [154] and the ab initio multiple spawing method (AIMS) algorithm [155]. In the CCS approach, several grids of coherent states are classically propagated and their trajectories can be derived from first principle dynamics. In AIMS, the nuclear wavefunction are spawned onto a multiple potential surface basis set. This set is made of adaptive time-dependent fixed-width Gaussian functions, which are generated by classical Newtonian dynamics.

5.2   First-Principles SC-IVR

In this work, we show how the semiclassical initial value representation (SC-IVR) method [144] can be coupled tightly and naturally, without any mayor change in formulation, with first principles electronic structure approaches to carry out classical molecular dynamics. We show how the method is able to reproduce approximately quantum effects such as the vibrational power spectra using a single, short classical trajectory using computational resources comparable to those employed in

first-principles molecular dynamics calculations. Calculations employing multiple trajectories can in principle be more accurate (and more computational intense as well), but here we focus on analyzing the predictive power of single trajectory runs. Finally, we describe how different approaches can be used in conjunction with this method for studying the symmetry of the vibrational states either by arranging the initial conditions of the classical trajectory or by employing the symmetry of the coherent state basis.

In the SC-IVR method, the propagator in F dimension is approximated by the phase space integral,

$$e^{-i\hat{H}t/\hbar} = \frac{1}{(2\pi\hbar)^F} \int d\mathbf{p}(0) \int d\mathbf{q}(0) \ C_t(\mathbf{p}(0), \mathbf{q}(0))$$

$$\times \ e^{iS_t(\mathbf{p}(0),\mathbf{q}(0))/\hbar} \ |\mathbf{p}(t), \mathbf{q}(t)\rangle\langle\mathbf{p}(0), \mathbf{q}(0)|, \qquad (5.1)$$

where $(\mathbf{p}(t), \mathbf{q}(t))$ are the set of classically-evolved phase space coordinates, S_t is the classical action and C_t is a pre-exponential factor. In the Heller-Herman-Kluk-Kay version of the SC-IVR [151, 156], the prefactor involves mixed phase space derivatives,

$$C_t(\mathbf{p}(0), \mathbf{q}(0)) = \sqrt{\frac{1}{2}\left|\frac{\partial\mathbf{q}(t)}{\partial\mathbf{q}(0)} + \frac{\partial\mathbf{p}(t)}{\partial\mathbf{p}(0)} - i\hbar\gamma\frac{\partial\mathbf{q}(t)}{\partial\mathbf{p}(0)} + \frac{i}{\gamma\hbar}\frac{\partial\mathbf{p}(t)}{\partial\mathbf{q}(0)}\right|}, \qquad (5.2)$$

as well as a set of reference states,

$$\langle\mathbf{q}\,|\,\mathbf{p}(t), \mathbf{q}(t)\rangle = \prod_i (\gamma_i/\pi)^{F/4} \exp\left[-\gamma_\mathbf{i}\cdot(q_i - q_i(t))/2 + ip_i(t)\cdot(q_i - q_i(t))/\hbar\right],$$

$$(5.3)$$

of fixed width γ_i. For bound systems, the widths are usually chosen to match the widths of the harmonic oscillator approximation to the wave function at the global minimum and no significant dependency has been found under width variation [145]. By introducing a $2F \times 2F$ symplectic monodromy matrix $\mathbf{M}(t) \equiv$

$\partial\left(\left(\mathbf{p}_t, \mathbf{q}_t\right) / \partial\left(\mathbf{p}_0, \mathbf{q}_0\right)\right)$, one can calculate the pre-factor of Eq. 5.2 from blocks of $F \times F$ size and monitor the accuracy of the classical approximate propagation by the deviation of its determinant from unity. Wang *et al.* suggested calculating the determinant of the positive-definite matrix $\mathbf{M}^T\mathbf{M}$ instead [157] and we monitored the same quantity for this work. The spectral density is obtained as a Fourier transform of the surviving probability[151]. The SC-IVR expression of the probability of survival for a phase-space reference state $|\chi\rangle = |p_N, q_N\rangle$ is,

$$\left\langle \chi \left| e^{-i\hat{H}t/\hbar} \right| \chi \right\rangle = \frac{1}{(2\pi\hbar)^F} \int d\mathbf{p}\,(0) \int d\mathbf{q}\,(0)\ C_t\left(\mathbf{p}\,(0), \mathbf{q}\,(0)\right)$$

$$\times\ e^{iS_t(\mathbf{p}(0),\mathbf{q}(0))/\hbar} \left\langle \chi \mid \mathbf{p}\,(t), \mathbf{q}\,(t)\right\rangle \left\langle \mathbf{p}\,(0), \mathbf{q}\,(0) \mid \chi\right\rangle. \qquad (5.4)$$

The phase-space integral of Eq. 5.4 is usually computed using Monte Carlo methods. If the simulation time is long enough, the phase space average can be well approximated by a time average integral. This idea has been suggested and implemented by Kaledin and Miller [158] to obtain the time averaging (TA-) SC-IVR approximation [159] for the spectral density,

$$I\,(E) = \frac{1}{(2\pi\hbar)^F} \int d\mathbf{p}\,(0) \int d\mathbf{q}\,(0)\ \frac{\mathrm{Re}}{\pi\hbar T} \int_0^T dt_1 \int_{t_1}^T dt_2\ C_{t_2}\left(\mathbf{p}\,(t_1), \mathbf{q}\,(t_1)\right)$$

$$\times \left\langle \chi \mid \mathbf{p}\,(t_2), \mathbf{q}\,(t_2)\right\rangle e^{i\left(S_{t_2}(\mathbf{p}(0),\mathbf{q}(0))+Et_2\right)/\hbar} \left[\left\langle \chi \mid \mathbf{p}\,(t_1), \mathbf{q}\,(t_1)\right\rangle e^{i\left(S_{t_1}(\mathbf{p}(0),\mathbf{q}(0))+Et_1\right)/\hbar}\right]^*,$$

$$(5.5)$$

where $\left(\mathbf{p}\,(t_1), \mathbf{q}\,(t_1)\right)$ and $\left(\mathbf{p}\,(t_2), \mathbf{q}\,(t_2)\right)$ are variables that evolve from the same initial conditions but to different times, and T is the total simulation time. The advantage of this approach is that the additional time integral can in principle replace the need for phase-space averaging in the large-time limit of a single trajectory. Calculations of the vibrational spectra of systems such as the water molecule have proved to be

very accurate using the TA-SC-IVR approach and its inexpensive single-trajectory variant showed significant improvements over the simple harmonic approximation for excited vibrational levels [158]. In order to make Eq. 5.5 less computationally demanding, one can employ the separable approximation [158], where the pre-factor of Eq. 5.5 is approximated as a phase, $C_{t_2}\left(\mathbf{p}\left(t_1\right),\mathbf{q}\left(t_1\right)\right)=\mathrm{Exp}\left[i\left(\phi\left(t_2\right)-\phi\left(t_1\right)\right)/\hbar\right]$, and $\phi\left(t\right)=\mathrm{phase}\left[C_t\left(\mathbf{p}\left(0\right),\mathbf{q}\left(0\right)\right)\right]$. Using this approximation, Eq. 5.5 becomes

$$
\begin{aligned}
I\left(E\right) = {} & \frac{1}{\left(2\pi\hbar\right)^F}\frac{1}{2\pi\hbar T} \\
& \times \int d\mathbf{p}\left(0\right)\int d\mathbf{q}\left(0\right)\left|\int_0^T dt\,\langle\chi\mid\mathbf{p}\left(t\right),\mathbf{q}\left(t\right)\rangle\,e^{i\left(S_t\left(\mathbf{p}(0),\mathbf{q}(0)\right)+Et+\phi_t\left(\mathbf{p}(0),\mathbf{q}(0)\right)/\hbar\right)}\right|^2
\end{aligned}
$$

(5.6)

leading to a simplification of the double-time integration to a single time integral. The resulting integral is positive definite, making more amenable for Monte Carlo integration. Our numerical tests show that the results of carrying out this approximation are essentially identical to the double time integral approach when using a single trajectory. In this paper results will be reported by use of this last approximation, since it is computationally cheaper and numerically more stable than Eq. 5.5.

For this work, we compute the potential energy surface at each nuclear configuration directly from the Kohn-Sham orbitals expanded on a non-orthogonal Gaussian basis. Gradients and Hessians at each nuclear configuration are obtained analytically from electronic orbitals. The evaluation of the potential represents most of the computational effort of our approach, which is roughly a few hours of computer time using standard desktop machines for a $1\ \mathrm{cm}^{-1}$ spectrum resolution. The nuclear equations

of motion are,

$$M_I \ddot{\mathbf{R}}_I = -\nabla_I \min_{\mathbf{C}} E_{DFT} \left[\mathbf{C}, \mathbf{R}_I \right], \tag{5.7}$$

where $\mathbf{C}$ is the rectangular matrix of the lowest occupied orbitals and the classical propagation is performed according to the velocity-Verlet algorithm, as implemented in the Q-Chem package [160]. At each time step, the potential, nuclear gradient and Hessian are used to calculate the action, pre-factor and coherent state overlaps necessary for the TA-SC-IVR method (Eq. 5.5 and 5.6). A schematic representation of an implementation of the algorithm for a multithreaded machine is shown in Fig. (5.1). At each time step, results are accumulated for time-average integration. The results presented on this work were carried out on a single thread. For each classical trajectory, the procedure is repeated and the final integration gives the spectrum intensity $I(E)$ for a given parametric value of E. The same procedure is repeated for next $E + \Delta E$, where in our calculation $\Delta E = 1 \text{cm}^{-1}$. As previously mentioned, the trajectory is monitored by calculating at each time step the deviation of the determinant of the monodromy matrix from unity. The difference in the determinants was always smaller than 10^{-6} during the course of the calculations. A time step of 10 a.u. has been always found to satisfy the strict monodromy matrix restrictions even for the lightest atoms.

The calculation of the full dimensional vibrational power spectrum of the CO_2 molecule is a challenging test for FP-SC-IVR method: A successful method should reproduce spectral features such as degenerate bending modes, strong intermodal couplings and Fermi resonances. To evaluate the FP-SC-IVR method, we compare vibrational spectrum of CO_2 molecule from FP-SC-IVR method to numerically-exact
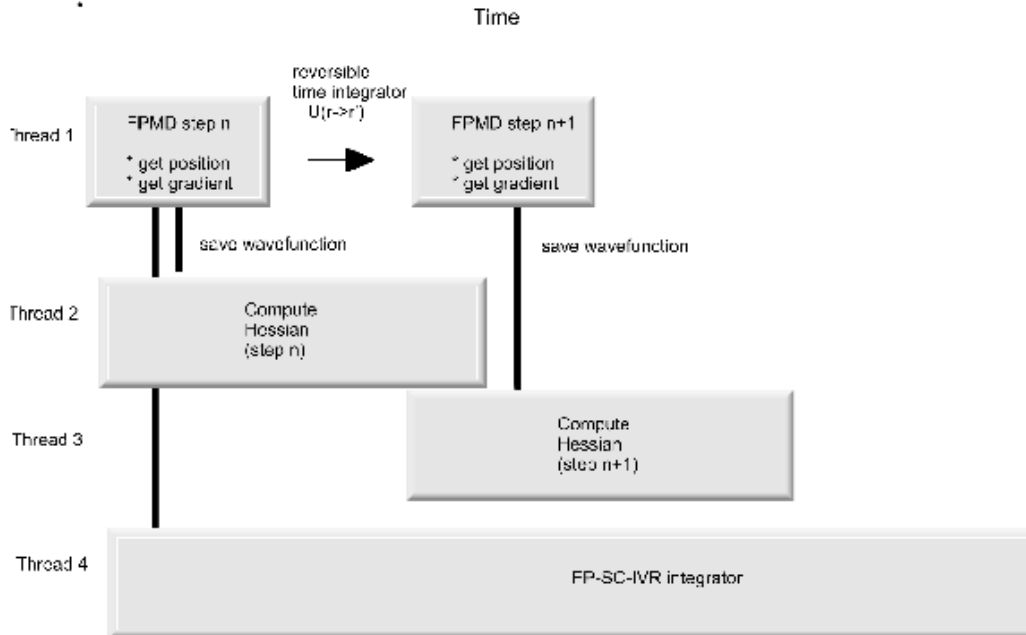
Figure 5.1: First-principles SC-IVR algorithm: At each time step electronic wavefunction are saved to calculated nuclear Hessian. Nuclear positions, gradients and Hessian are accumulated for the spectral time-average integral.

discrete variable representation (DVR) eigenvalue calculations on a potential fitted to a set of first-principles points obtained at the same level of theory. The next section describes the details of the potential fitting and DVR calculation. Following, we continue on the discussion of the FP-SC-IVR method.

5.3 Potential Fitting and Grid Calculations

The CO_2 molecule is a linear molecule with four vibrational normal modes: a symmetric stretching mode (ν_1), degenerate bending modes (ν_2 and $\bar{\nu}_2$) , and an antisymmetric stretching mode (ν_3). A $3d$ potential energy grid in internal coordinates is calculated using the B3LYP density functional [161] with the cc-pVDZ

basis set [162]. The grid points are then fitted to a potential energy surface [163] represented by a fourth-order Morse-cosine expansion,

$$V\left(r_1, r_2, \theta\right) = \sum_{i,j,k=0}^{4} K_{ijk} \left(1 - e^{-a_1(r_1 - r_e)}\right)^i \times (cos\theta - cos\theta_e)^j \left(1 - e^{-a_2(r_2 - r_e)}\right)^k, \quad (5.8)$$

where the parameter $r_e = 2.206119$ a.u. and $\theta_e = 180$ specify the equilibrium coordinates of the CO_2 molecule. The Morse parameters $a_1 = a_2 = 1.2489$ a.u. were determined so as to minimize the standard deviation of the differences of the fitted potential from the ab initio result using the Levenberg-Marquardt non-linear least square algorithm [164] . Instead, r_e was obtained by geometry optimization within the Q-Chem *ab initio* package [160].

The 35 K_{ijk} coefficients were subject to the non-linear least square fitting procedure to the DFT energies. Since these coefficients must be the same once r_1 and r_2 are swapped, 13 linear constraints of the type $K_{ijk} = K_{kji}$ were imposed during the fitting procedure. Additionally, to ensure that the equilibrium geometry was fitted to the predetermined equilibrium parametric distance, the coefficients K_{100} and K_{001} were constrained to be zero. Consequently, we employed a total number of 14 fitting constraints (K_{000} term is always constant). A total of 2500 *ab initio* grid points were chosen for the fitting process. These grid points range from 1.42 a.u. to 7.09 a.u. for r_1 and r_2, and from 113.6 to 180 for the angle variable. The calculated expansion coefficients K_{ijk} are reported in Table 5.1.

As far as the numerically exact eigenvalues calculations is concerned, we used an exact DVR (Discrete Variable Representation) matrix diagonalization procedure. The CO_2 molecule was described for grid calculations in internal coordinates, while *on-the-fly* classical trajectories and the SC-IVR calculations described previously were

coeff.	attoJ	coeff.	attoJ
K_{001}	+0.000000	K_{100}	$= K_{001}$
K_{002}	+1.442886	K_{200}	$= K_{002}$
K_{003}	-0.032125	K_{300}	$= K_{003}$
K_{004}	+0.003630	K_{400}	$= K_{004}$
K_{010}	+0.726891	K_{111}	+0.392310
K_{011}	-0.443422	K_{110}	$= K_{011}$
K_{012}	-0.162970	K_{210}	$= K_{012}$
K_{013}	-0.101077	K_{310}	$= K_{013}$
K_{020}	+0.488451	K_{121}	+0.606572
K_{021}	-0.358126	K_{120}	$= K_{021}$
K_{022}	-0.210888	K_{220}	$= K_{022}$
K_{030}	+0.175981	K_{202}	+0.097300
K_{031}	-0.184503	K_{130}	$= K_{031}$
K_{112}	+0.103205	K_{211}	$= K_{112}$
K_{101}	+0.210532	K_{040}	+0.155374
K_{102}	+0.067998	K_{201}	$= K_{102}$
K_{103}	+0.068693	K_{301}	$= K_{103}$

Table 5.1: Expansion coefficients K_{ijk} for the CO_2 B3LYP/cc-pVDZ fitted potential energy surface in attoJoule units.

performed in Cartesian coordinates. No significant contamination between the rotational (set to zero kinetic energy) and vibrational motion was found within the simulation time. To this end, the deviation from simplecticity of the monodromy matrix in the vibrational sub-space were never more than 10^{-6} as previously mentioned.

The coordinates r_1 and r_2 are CO distances, and θ is the angle between the CO bonds. In these coordinates the kinetic part of the Hamiltonian for $J = 0$ is,

$$T = \frac{p_1^2}{2\mu_{CO}} + \frac{p_2^2}{2\mu_{CO}} + \frac{j^2}{2\mu_{CO}r_1^2} + \frac{j^2}{2\mu_{CO}r_2^2}$$
$$+ \frac{p_1 p_2 cos\theta}{m_C} - \frac{p_1 p_\theta}{m_C r_2} - \frac{p_2 p_\theta}{m_C r_2} - \frac{cos\theta j^2 + j^2 cos\theta}{2 m_C r_1 r_2}, \tag{5.9}$$

where $p_k = -i\frac{\partial}{\partial r_k}$, $p_\theta = -i\frac{\partial}{\partial \theta}sin\theta$, and $j^2 = -\frac{1}{sin\theta}\frac{\partial}{\partial \theta}sin\theta\frac{\partial}{\partial \theta}$. The carbon mass were taken to be $m_C = 12.0$ a.m.u., while the oxygen mass $m_O = 15.9949$ a.m.u. and the

reduced mass is as usual $1/\mu_{CO} = 1/m_C + 1/m_O$.

As previosuly mentioned, in order to calculate exact eigenvalues, a sine-DVR basis for the coordinates r_1 and r_2 and a Legendre-DVR basis for θ has been used [165]. For each degree of freedom 50 DVR functions were used and eigenvalues were converged to at least 10^{-3}cm^{-1}. The sine-DVR ranged from 1.51 a.u. to 3.78 a.u. and the magnetic quantum number m of the Legendre-DVR was zero.

Because of the restriction of total angular momentum $J = 0$, we couldn't observe all degenerate bending excitations. However, ZPE and several vibrational energy levels were obtained and compared with that ones coming from a single *on-the-fly* semiclassical trajectory.

5.4   First-Principles SC-IVR Calculations

The full power spectrum obtained using Eq. (5.5) after 3000 BOMD steps of 10 a.u. each is shown on the bottom of Fig. 5.2. For longer simulations, the monodromy matrix symplectic properties as well as the resolution of the spectrum started to deteriorate. The calculated vibrational zero-point energy (ZPE) value was 2518 cm^{-1} versus the exact value of 2514.27 cm^{-1} and both are in good agreement with the experimental value of $2508 \, \text{cm}^{-1}$. In contrast, harmonic normal-mode analysis (whose frequencies are 656.62, 1363.46, 2423.47 wavenumbers) predicts a frequency of $2550.08 \, \text{cm}^{-1}$. Thus, the TA-SC-IVR method successfully reproduces the ZPE anharmonic effects with the use of a single classical trajectory. Some representative frequencies of the power spectrum are presented in Table 5.2. The ZPE was shifted to zero for comparison with reported classical ELMD simulations on the same system
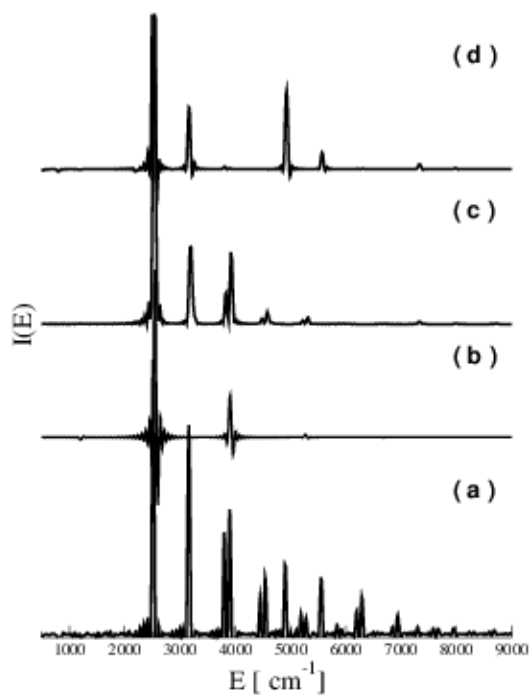
Figure 5.2: CO_2 Vibrational Power Spectrum: Initial kinetic energy on: (a) all modes; (b) symmetric mode; (c) one bending and symmetric modes; (d) bending and asymmetric modes.

that cannot reproduce the ZPE or higher vibrational states [166, 167] but only single modes frequencies. For these studies of Refs. 166 and 167, the vibrational data were obtained from the Fourier transform of correlation functions of classical trajectories in plane-wave DFT calculations. The ELMD approach predicts the following fundamental frequencies 648, 1368, 1428 and 2353 for Ref. 166 and 663, 1379, 1456 and 2355 for Ref. 167. These classical results are similar but limited to a normal mode analysis.

Table 5.2 compares our TA-SC-IVR results with the exact ones and to those obtained by Filho [168] with the same density functional and a basis set of comparable quality (6-31+G*) [169], using a perturbative approximation of the eigenvalue expansion. One can see how a different basis set results a significant deviation of vibrational levels spacing, once the comparison is performed in units of wavenumbers.

A major difficulty on the CO_2 power spectrum simulations is the calculation of the Fermi resonance splittings. These are the result of anharmonic couplings, and they represent a stringent test for a semi-classical method that relies on a single short trajectory. The Fermi resonances occur when an accidental degeneracy between two excited vibrational levels of the same symmetry exists and it results in a repulsion between the corresponding energy levels. The sources of these resonances are purely anharmonic and are only present in polyatomic potentials. For the CO_2 molecule, the unperturbed frequencies for the symmetric stretching are roughly equal to the first bending overtone ($\nu_1 \cong 2\nu_2$). For these modes, the wavefunctions are transformed as the irreducible representation of $D_{\infty h}$, *i.e.* $\nu_1(10^00)$ as Σ_g^+, at the experimental frequency of $1388 \, \mathrm{cm}^{-1}$, and $\nu_2^2(02^00)$ as $\Sigma_g^+ + \Delta_g$, at an experimental frequency of

Exp.[a]	mode[b]	Harmonic[c]	FP-SCIVR-SA[d]	DVR	Ref. 168
667.4	$0, 1^1, 0$	656.62	644		657.2
1285.4$^\wedge$	$0, 2^0, 0$	1313.24	1288	1252.91	1283.4
1388.2$^\wedge$	$1, 0^0, 0$	1363.46	1381	1372.29	1408.8
1932.5†	$0, 3^1, 0$	1969.86	1932		1930.2
2003.2	$0, 3^3, 0$	1969.86	2024		2004.9
2076.9†	$1, 1^1, 0$	2020.08	2106		2098.5
2349.1	$0, 0^0, 1$	2423.47	2388	2359.51	2411.5
2548.4‡	$0, 4^0, 0$	2626.48	2515	2482.95	2553.3
2585.0*	$0, 4^2, 0$	2626.48	2578		2591.2
2671.7‡	$0, 4^4, 0$	2626.48	2669	2640.15	2716.5
2760.7*	$1, 2^2, 0$	2676.70	2759		2796.3
2797.2‡	$2, 0^0, 0$	2726.92	2793	2757.14	2845.2
4673.3	$0, 0^0, 2$	4846.94	4690$^+$	4693.24	4797.8
6972.6	$0, 0^0, 3$	7270.41	6803$^+$	6821.35	7152.9

Table 5.2: (*a*) Experimental frequencies in cm^{-1} from Ref. 173. (*b*) First number is the symmetric stretch quantum, second are the degenerate bendings, and third one is the asymmetric stretch. The exponent of the second number is the l_i degeneracy index. (*c*) Vibrational levels according to a normal modes harmonic model. (*d*) Using the Separable approximation of Eq. 5.6. Some of the calculated vibrational energy eigenvalues are tabulated. All data are in wavenumbers. Fermi Resonances group of frequencies are indicated by the same superscript symbols. Uncertain peaks are marked with (+). The first column represents the experimental vibrational frequencies associated with the modes listed on the second column. The third column shows the harmonic DFT results. In the fourth and fifth columns, we show our FP-SCIVR and exact numerical DVR calculations in the B3LYP/cc-PVDZ model chemistry used for the FP-SCIVR calculations. The fifth column shows perturbative DFT calculations carried out using a similar functional and basis set.

$1285 \, \mathrm{cm}^{-1}$. Another Fermi doublet results from the addition of a quantum of bending mode to the previous Fermi doublet to yield the following states: $\nu_1\nu_2(11^10)$, at an experimental frequency of $2077 \, \mathrm{cm}^{-1}$ and the $\nu_2^3(03^10)$ state, at an experimental frequency of $1932 \, \mathrm{cm}^{-1}$. Higher-energy Fermi resonances are indicated in Table 5.2 by using the same superscript symbols. The first Fermi terms are located at 1313 and 1363 in a harmonic approximation and corrected to 1288 and 1381 wavenumbers for FP-TA-SC-IVR. Thus, the original levels have been repelled by Fermi couplings. One mode is located at a higher frequency than the harmonic prediction, while the other is at a lower frequency. The latter effect could be explained also by simple anharmonicity, but the former is evidence of the ability of the single trajectory FP-TA-SC-IVR method even when the separable approximation is used to capture Fermi resonance effects partially. The same reasoning can explain the second Fermi doublet located at 1932 and 2106 for FP-TA-SC-IVR, while the harmonic estimate at 1970 and 2020 wavenumbers.

With the FP-TA-SC-IVR method, one can also identify the couplings between vibrational modes and the appearance of Fermi resonance splittings by carrying out simulations with different initial conditions. This can be achieved by selectively setting the initial velocity of some vibrational modes to zero. The anharmonic coupling between levels leads to a consistent reproduction of the ZPE peak in the spectrum for all simulations. However the excited vibrational peaks related to the modes with zero initial kinetic energy show a very small signal in the power spectrum. Vibrational energy redistribution processes can be studied as well, by carrying out simulations at different timescales. In Fig. 5.2, we show the resulting power spectra for different

117

initial conditions. If the initial state contains only purely symmetric motion, the lowest Fermi resonance peaks in Fig. 5.2(b) are absent as well as for a bending (without symmetric stretching) motion in Fig. 5.2(d). These results and the intensity of their peaks respect to that ones located at the same frequencies in Fig. 5.2(a) suggest that the Fermi resonance is indeed originated from the coupling between bending and the symmetric modes. One can reach the same conclusions by inspecting the lower Fermi doublet peaks intensity: by adding a bending mode (from Fig. 5.2(b) to Fig. 5.2(c)) and a second one (from Fig. 5.2(c) to Fig. 5.2(a)) the intensity of both peaks is gradually raised. This is called "intensity borrowing" and it arises from the strong mixing of the zero order states. These observations reinstate that "repulsion and mixing are the hallmarks of Fermi resonances" [170]. Also, for a distinct set of initial conditions, an additional peak at 5500 cm^{-1} related to the asymmetric stretch was observed. Using the proposed approach, one can carefully detect the characteristics of each peak even for complicated power spectra.

An attractive method for obtaining the symmetry properties of the eigenstates involves arranging the initial basis vectors [158, 171]. The basis for this method is the direct product of coherent states $|\chi\rangle = \prod_{k=1}^{4} |p_i^{(k)}, q_i^{(k)}\rangle^{\epsilon_k}$. These states can be chosen to have an initial symmetry by employing linear combinations of the form $|p_i^{(k)}, q_i^{(k)}\rangle^{\epsilon_k} = \left(|p_i^{(k)}, q_i^{(k)}\rangle + \epsilon_k |-p, -q_i^{(k)}\rangle \right) / \sqrt{2}$. The k-th mode can be made symmetric ($\epsilon_k = 1$), antisymmetric ($\epsilon_k = -1$) or have no symmetry restrictions ($\epsilon_k = 0$). In order to assign the proper symmetry to each peak on Fig. 5.3 , the reduced D_{2h} symmetry group was adopted. All irreducible representations were reproduced and peaks were grouped by symmetry as reported in Fig. 5.3. Note that (d) and (e)
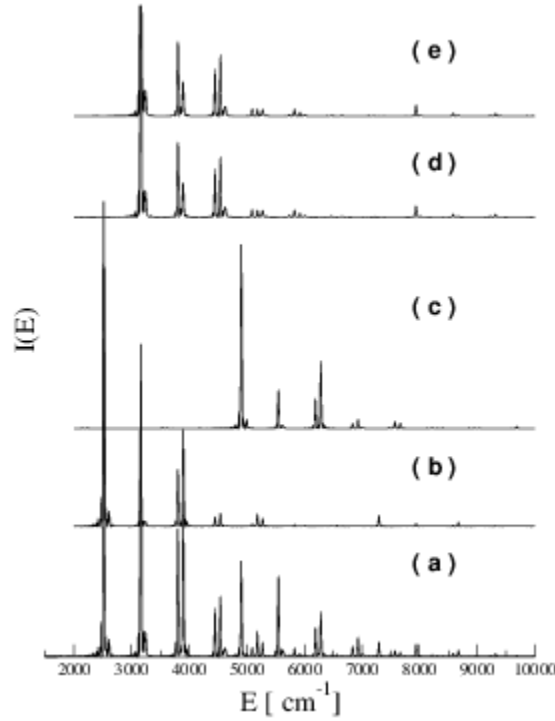
Figure 5.3: CO_2 Vibrational Power Spectrum (Separable approximation): Different basis set symmetries for ν_1(symmetric stretching mode), ν_2 and $\bar{\nu}_2$ (bending modes) and ν_3(asymmetric mode) and the corresponding D_{2h} irreducible representation; (a) all ϵs are zero; (b) (B_{1u}): $\epsilon(v_1) = 0, \epsilon(v_2) = 1, \epsilon(\bar{\nu}_2) = 0, \epsilon(v_3) = -1$; (c) (A_g): $\epsilon(v_1) = 1, \epsilon(v_2) = 0, \epsilon(\bar{\nu}_2) = 0, \epsilon(v_3) = 1$; (d) (B_{2u}): $\epsilon(v_1) = 0, \epsilon(v_2) = -1, \epsilon(\bar{\nu}_2) = 0, \epsilon(v_3) = 1$, (e) (B_{3u}) $\epsilon(v_1) = 0, \epsilon(v_2) = 0, \epsilon(\bar{\nu}_2) = -1, \epsilon(v_3) = 1$. B_{2u} and B_{3u} representations are degenerated in the $D_{\infty h}$ subspace as shown.
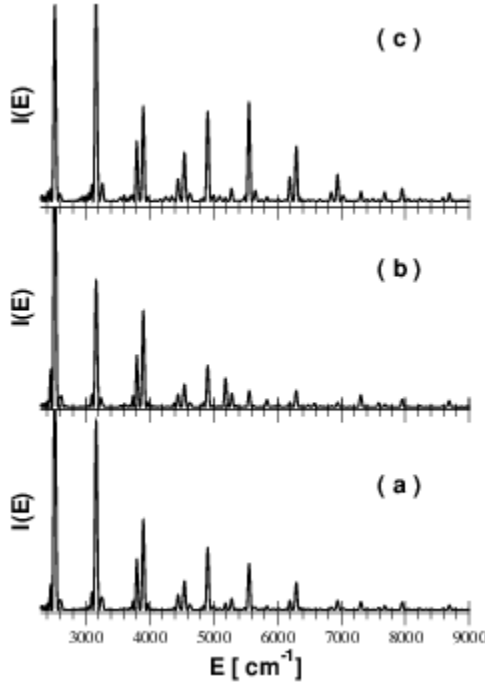
Figure 5.4: Gaussian width variations and related power spectra: a) $\gamma_i = \omega_i$; b)$\gamma_i = 2\omega_i$; c)$\gamma_i = \omega_i/2$, where ω_i are the $i-esime$ normal mode frequency. The FP-SCIVR power spectra are fairly insensitive to variations in the value of the coherent state width.

plots are identical since they only differ trivially by swapping coefficients between the degenerate bending modes in the original $D_{\infty h}$ symmetry group.

Finally we have investigated the stability of the propagator versus variations of the coherent states gaussian width parameters γ_i. Previous calculations [156] have shown that there is no significant depedency on energy and norm conservation for the semiclassical propagator if suitable values of γ_i are chosen. For power spectra calculation we have chosen to look at vibrational levels variations under different values of coeherent states width. Since a single trajectory was used in the FP-TA-SC-IVR approach, no Monte Carlo integration is performed in phase space coordinates and the changes of γ_i are confined to the coherent states overlap and to the prefactor in

Eq. 5.2. As reported in Fig. 5.4 and checked on a finer scale, no significant variation was observed beyond $1\,\mathrm{cm}^{-1}$. These findings are in agreements with previous calculations on the same propagator [156]. Interestingly, a different distribution in peaks intensity were found in each panel. Since the peaks magnitude is proportional to the overlap between the reference state and the actual eigenfunction, the anharmonic choice ($\gamma_i = \omega_i/2$) is a more suitable solution as clearly showed on panel (c) of Fig. 5.4.

5.5   Conclusions

In conclusion, we have shown that SC-IVR can be implemented easily and efficiently using first principles molecular dynamics. With the modest computational cost of a single classical trajectory, the vibrational density of states of the CO_2 molecule was calculated. On Fig. 5.5 we report a graphical comparison between the harmonic and the FP-TA-SC-IVR approximations, versus the exact vibrational value for the Fermi resonance multiplets. One can notice how the single trajectory FP-TA-SC-IVR goes far beyond the harmonic approximation by removing the harmonic degenerancy and including part of anharmonicity. Fermi splittings are well mimiced not only for the first doublet, but also for the higher ones. The numerically exact DVR vibrational energy levels constrained by $J = 0$ are represented on the last column. The FP-TA-SC-IVR values are similar to the DVR results, when comparison is possible. However, a closer look at Table 5.2 shows how these single trajectory FP-TA-SC-IVR calculations can include only part of the anharmonicity and that their precision gets worse for higher vibrational levels. In particular, the spacing of the higher-energy states is
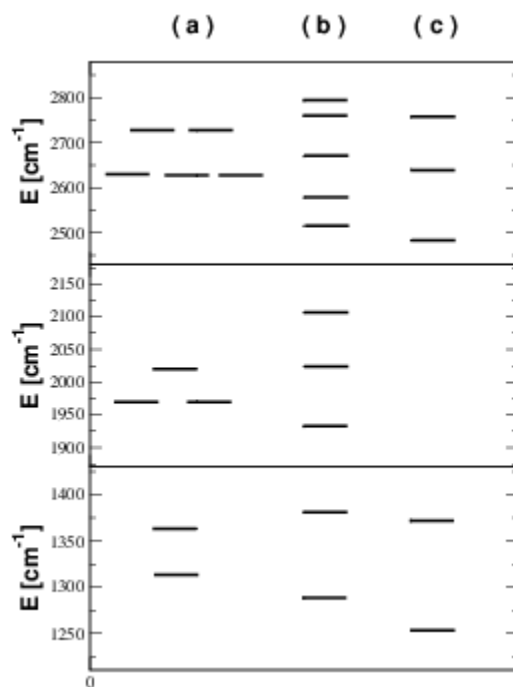
Figure 5.5: Fermi Resonance states vibrational energy level: (a) in harmonic approximation; (b) single FP-SC-IVR trajectory calculation; (c) exact grid calculation on splined potential.

harmonic-like and thisis the mayor limitation of using a single classical trajectory.

These and previous calculations on model potentials [158] has shown how the single trajectory TA-SC-IVR gives reasonable results and performs better for higher frequencies modes. The computational cost of the method is essentially the same as classical propagation, and therefore, if broadly implemented in electronic structure codes, it can provide a description of quantum effects at a comparable computational cost to that of classical approaches. Possible applications of this method or related ones are the study of excited electronic states and Franck-Condon transitions, such as vibrational absorption spectra [174]. Although this single trajectory approach may be a practical tool for the simulation of more complex systems, the use of more trajectories is probably required to remove any harmonic "ghost states". We are currently exploring the use of a small number of a set of systematically determined trajectories for further improvement of the results. If the number of required trajectories grows as a low polynomial of the system size, semi-classical methods could be competitive with currently-employed numerical approximations to obtain anharmonic vibrational effects. Finally, we expect that the representation of the potential energy in terms of normal coordinates will become less suitable when large amplitude motions or non adiabatic effects come into play.

Chapter 6

Simplified Sum-Over-States Approach for Predicting Resonance Raman Spectra

6.1 Introduction

Resonance enhancement of Raman scattering, which occurs whenever the frequency of the incident radiation approaches molecular excitation frequencies, was reported some 20 years after the initial experimental observation of the Raman effect [175, 176]. The large degree of enhancement spanning several orders of magnitude is useful for detection of the inherently inefficient spontaneous Raman scattering. Moreover, the shapes of Raman spectra change considerably at resonance with molecular excitations and provide information on structures and properties of electronic excited states. Resonance Raman spectroscopy is a sensitive spectroscopic

technique for strongly absorbing chemical constituents such as nucleic acid bases, aromatic aminoacids, and heme chromophores [177–179].

Another important manifestation of resonance enhancement emerges in surface-enhanced Raman scattering (SERS) [180–182]. The surface enhancement of Raman scattering is observed in molecules adsorbed on rough or nanostructured noble-metal surfaces and comprises an electromagnetic and a chemical contribution [182, 183]. The chemical contribution to the SERS intensities, while generally smaller in magnitude than the electromagnetic enhancement, is sensitive to the electronic structure of the adsorbate. The chemical effect leads to characteristic changes in the relative intensities of Raman bands and alters the overall shape of the Raman spectra compared to neat substance. Chemical effects are satisfactorily described by cluster models and can be attributed to resonance enhancement due to interface states [184, 185]. The combination of surface enhancement with intramolecular excitations gives rise to surface-enhanced resonance Raman scattering (SERRS) which provides an extraordinary sensitivity, even to the level of single-molecule detection [186–188].

While theoretical descriptions of resonance Raman scattering has been developed early on by Shorygin and co-workers [176, 189] and by Albrecht [190, 191], calculations of resonance Raman scattering from medium-size and large molecules are not often routinely performed. Raman scattering is a second-order process and its cross sections are given by the Kramers–Heisenberg–Dirac (KHD) dispersion relation [192, 193]. The classical expression for Raman cross sections involving derivatives of electronic polarizabilities with respect to vibrational normal modes can be obtained via closure of the sum over intermediate *vibronic* states in the KHD expression [194, 195].

The description of Shorygin and co-workers [189, 196] represents the polarizability derivatives as a sum over *electronic* states and introduces parameters for the resulting derivatives of excitation energies and oscillator strengths of the lowest excited state with respect to vibrational normal modes.

On the other hand, Albrecht's approach is rooted in the vibronic coupling theory [197, 198] and introduces the Herzberg–Teller expansion into the sum over *vibronic* states of the KHD dispersion relation. Each vibronic state contributes four different terms denoted A, B, C, and D by Albrecht. The A term is due to vibrational wavefunction overlap of the initial and the intermediate state and of the intermediate and the final state. The B and C terms arise from the dependence of transition dipole moments on vibrational coordinates and are analogous to the intensity borrowing terms of vibronic coupling theory [197, 198]. The B term is derived from the coupling between the intermediate electronic excited state to other excited states, while the C term is due to the coupling between the ground electronic state to excited states and is customarily assumed to be small. The D term is of higher order in the coupling between electronic states and is often neglected. Albrecht's treatment involves a full sum over all vibronic states of the molecule and is thus rarely computationally tractable for larger systems. Nevertheless, it constituted a major breakthrough in the understanding of Raman scattering in that it provided a unified picture for both non-resonant and resonant Raman spectra. Sums over vibronic states can be evaluated in the displaced harmonic oscillator approximation [199].

A different approach to resonance Raman scattering was proposed by Heller and co-workers [200]. It amounts to a transformation of the KHD dispersion relation into

the time domain, which represents the resonance Raman process as a propagation of vibrational wavepackets (multiplied with transition dipole moments) on the excited-state potential energy surface. Often, the short-time approximation to propagation dynamics is introduced [201], which has proven remarkably useful in interpreting resonance Raman spectra [201–203].

Finally, resonance Raman cross section can be expressed in a fashion analogous to the non-resonant case by introducing finite lifetimes for the intermediate states, or in other words, by computing Raman cross sections from derivatives of electronic polarizabilities evaluated at complex frequencies $\tilde{\omega} = \omega + i\gamma$ [204, 205]. Here ω is the excitation frequency and γ corresponds to an averaged lifetime of excited states, which is usually treated as an empirical parameter.

The purpose of the present work is to provide a simple and computationally tractable approximation for resonance Raman cross sections. To this end, we reduce the summation over vibronic states of the KHD dispersion relation to a summation of *electronic* states, similar to the parametric method of Shorygin and co-workers, and apply the double harmonic approximation, which is commonly used in calculations of vibrational spectra. This approximation requires only excitation energies, transition dipole moments, and their respective geometric derivatives to be computed for the electronic excited states included in the sum-over-states expression. In contrast to Shorygin's work, all parameters in the sum-over-states expression are provided from *ab initio* calculations, while the summation runs over all electronic excitations in a given energy range. Analytical gradient techniques make computation of geometric derivatives particularly efficient in the framework of time-dependent density

functional theory (TDDFT) [206]. In addition, the sum-over-states approach may be used to identify major contributions to resonance Raman intensities. We apply the present approach to assign and interpret resonance Raman scattering in nucleic acid bases.

6.2 Theory

The polarizability theory of Raman scattering due to Placzek relates the Raman scattering cross section to frequency-dependent electronic polarizabilities at the frequency of the incident radiation [191, 195],

$$\alpha^{mn}(\omega) = \sum_k \left[\frac{\mu_{0k}^m \mu_{0k}^n}{\Omega_k - \omega} + \frac{\mu_{0k}^n \mu_{0k}^m}{\Omega_k + \omega} \right]. \tag{6.1}$$

m and n are Cartesian directions. We use atomic units throughout. The summation is over all electronic excited states $k > 0$ with excitation energies Ω_k and transition dipole moments μ_{0k}^m. The polarizability theory of Raman scattering is based on the separability of the electronic and nuclear wavefunctions (Born–Oppenheimer approximation) and the assumption that the incident radiation is sufficiently far from resonance such that energy differences between vibronic levels of the KHD expression may be approximated by electronic excitation energies Ω_k. In the double harmonic approximation, the Raman scattering cross sections are proportional to derivatives of $\alpha^{mn}(\omega)$ with respect to vibrational normal modes [191, 195]. Straightforward differentiation of the sum-over-states expansion for $\alpha(\omega)$ with respect to the vibrational normal mode Q yields the following expression for the Raman scattering cross section

of the vibration Q,

$$\left(\frac{\partial \sigma}{\partial \Omega}\right)_Q = \frac{(\omega - \omega_Q)^4}{2\omega_Q c^4} \left|\langle \boldsymbol{\sigma}_Q(\omega)\rangle\right|^2 , \tag{6.2}$$

where the components of the Raman scattering tensor $\sigma_Q^{mn}(\omega)$ are given by

$$
\begin{aligned}
\sigma_Q^{mn}(\omega) = \sum_k \Bigg[&-\mu_{0k}^m \mu_{0k}^n \left[\frac{(\Omega_k - \omega)^2 - \gamma_k^2}{((\Omega_k - \omega)^2 + \gamma_k^2)^2} + \frac{i\, 2(\Omega_k - \omega)\gamma_k}{((\Omega_k - \omega)^2 + \gamma_k^2)^2}\right] \frac{\partial \Omega_k}{\partial Q} \\
&+ \left[\mu_{0k}^m \frac{\partial \mu_{0k}^n}{\partial Q} + \frac{\partial \mu_{0k}^m}{\partial Q} \mu_{0k}^n\right]\left[\frac{\Omega_k - \omega}{(\Omega_k - \omega)^2 + \gamma_k^2} + \frac{i\,\gamma_k}{(\Omega_k - \omega)^2 + \gamma_k^2}\right]\Bigg] .
\end{aligned}
\tag{6.3}
$$

Here, ω_Q is the vibrational frequency, c is the speed of light. Angle brackets denote the appropriate orientational average over components of the Raman scattering tensor $\boldsymbol{\sigma}_Q(\omega)$. The excited states $k > 0$ have linewidths γ_k associated with them, which are chosen as empirical parameters independent of k in most studies. We will follow this practice here. The analogous expression for $\sigma_Q^{mn}(\omega)$ with uniform linewidths $\gamma_k = \gamma$ for all excited states may be obtained by differentiation of the polarizability evaluated at the complex frequency $\tilde{\omega} = \omega + i\gamma$ [204, 205]. In contrast, in the present approach different linewidths γ_k may be chosen for individual excited states to reflect differences in their lifetimes. Ultimately, the excited-state linewidths may be rigorously derived from a open-system formulation, e. g., in the framework of TDDFT [207–209].

In practice, the sum over electronic excited states has to be truncated. The number of excited states contributing significantly to the Raman cross sections in Eq. 6.3 will be small in the vicinity of a resonance ($|\omega - \Omega_k| \approx \gamma_k$) but might increase significantly in the non-resonant case. While truncation of the sum-over-states is a potential source of error not present in the finite-lifetime approach [204, 205], we find that convergence is sufficiently fast even in the non-resonant regime for nucleic acid bases considered here.

Differentiation of the frequency-dependent electronic polarizabilities (Eq. 6.1) with respect to the vibrational normal mode Q gives rise to two kinds of terms for each excited state. The first term in Eq. 6.3 is proportional to the Cartesian derivative (gradient) of the excitation energy $\frac{\partial \Omega_k}{\partial Q}$. It may be compared to the A term in Albrecht's approach, which arises from the energy differences between vibronic states in the energy denominator [190, 191]. By analogy, we will refer to these contributions as the A terms in the following. Only totally symmetric vibrational modes Q yield non-zero energy derivatives $\frac{\partial \Omega_k}{\partial Q}$, therefore A terms are only present for totally symmetric vibrations. The second term in Eq. 6.3 results from the dependence of transition moments μ_{0k}^m on the vibrational normal modes. In the language of Herzberg–Teller coupling [190, 197, 198], this dependence results from the interaction of the ground state or the electronic excited state k with other electronic states induced by nuclear displacements along the vibrational mode Q. The corresponding contributions are denoted B and C terms, respectively, in Albrecht's approach. The terms in Eq. 6.3 that are proportional to derivatives of transition dipole moments $\frac{\partial \mu_{0k}^m}{\partial Q}$ have the same origin and hence will be referred to as B terms. B terms are non-zero for vibrational modes that transform like components of the polarizability tensor; the selection rules for the B term are equivalent to those for non-resonant Raman scattering [190, 191].

The frequency dependence of Raman spectra is defined by the molecular electronic excitation spectrum. In the strictly resonant case ($\omega = \Omega_k$) the excited electronic state k dominates the sum in Eq. 6.3. In this limit, the shape of the resonance Raman spectrum reflects the structure of the potential energy surface of the excited state k. Since the A term is quadratic in the resonance denominator $((\Omega_k - \omega)^2 + \gamma_k^2)^{-1}$, while

the B term is linear in it, the A term contribution can be expected to be predominant at resonance. In the opposite limiting case the excitation frequency is far from any electronic excitations (non-resonant Raman scattering), and a considerable number of electronic excited states contributes to the sum-over-states expression (Eq. 6.3.) The B term contributions become dominant in Raman cross sections, while the A terms are scaled down by their large energy denominators. Smooth interpolation between both limiting cases (non-resonant and strictly resonant) requires that both A and B terms be treated on equal footing.

Analytical derivative techniques allow to compute excitation energy gradients and non-resonant polarizability derivatives in an efficient fashion using TDDFT [206, 210]. In this work, derivatives of transition dipole moments are computed by numerical differentiation. However, an analytical implementation is possible starting from a Lagrangian formulation [211], similar to that for gradients of excitation energies [212, 213] and frequency-dependent polarizabilities [210].

6.3   Resonance Raman Spectra of nucleic acid bases

In the following, we explore the characteristic changes in resonance Raman spectra of guanosine for excitations in the range between 200–266 nm, which contains a number of electronic excitations. In addition, we consider Raman excitation profiles of ring-breathing modes of nucleosides. Raman excitation profiles describe the dependence of Raman cross sections on the energy of the incident radiation. Finally, we determine the relative contributions of the A and B terms to Raman cross sections of guanosine both at resonance and in the non-resonant case.

All calculations have been performed using the PBE0 functional [214] and triple-zeta valence basis sets with two sets of polarization functions (TZVPP) [215]. The PBE0 functional has been chosen because it has proven quite accurate both for polarizabilities [216, 217] and Raman intensities [210, 218]. However, vibrational frequencies [219] and electronic excitation energies [220] are often overestimated with PBE0. 20 excited electronic states were included in the sum-over-states expressions. Linewidth parameters were assumed to be 0.1 eV for all electronic states. All calculations were performed using the program package TURBOMOLE [221].

In Fig. 6.1(a)–(c), we compare experimental and computed resonance Raman spectra of guanosine at excitation wavelengths of 266 nm, 218 nm, and 200 nm. In addition, we show experimental and computed non-resonant Raman spectra of guanosine at 514.5 nm in Fig. 6.1(d). The experimental spectra are from Refs. 222 and 223. The considered range of excitation energies includes the two overlapping electronic absorption bands of guanosine observed experimentally at 4.4–4.6 eV and 4.8–5.1 eV [224–226]. Deconvolution of the UV absorption spectrum of guanosine in water yields 4.56 eV and 5.04 eV for the positions of the absorption maxima [224]. PBE0 predicts the two lowest electronic excited states of guanosine at 4.97 eV and 5.39 eV to be strongly allowed. At still higher excitation energies, a second pair of strongly allowed electronic absorption bands is observed experimentally [224, 226], with maxima at 6.17 eV and 6.67 eV, respectively. The computed excitation energies for these transitions are 6.79 eV and 6.99 eV. We refer to supplementary information for a full overview of computed and experimental excitation energies of guanosine. The overestimation of excitation energies observed here is quite typical for the PBE0
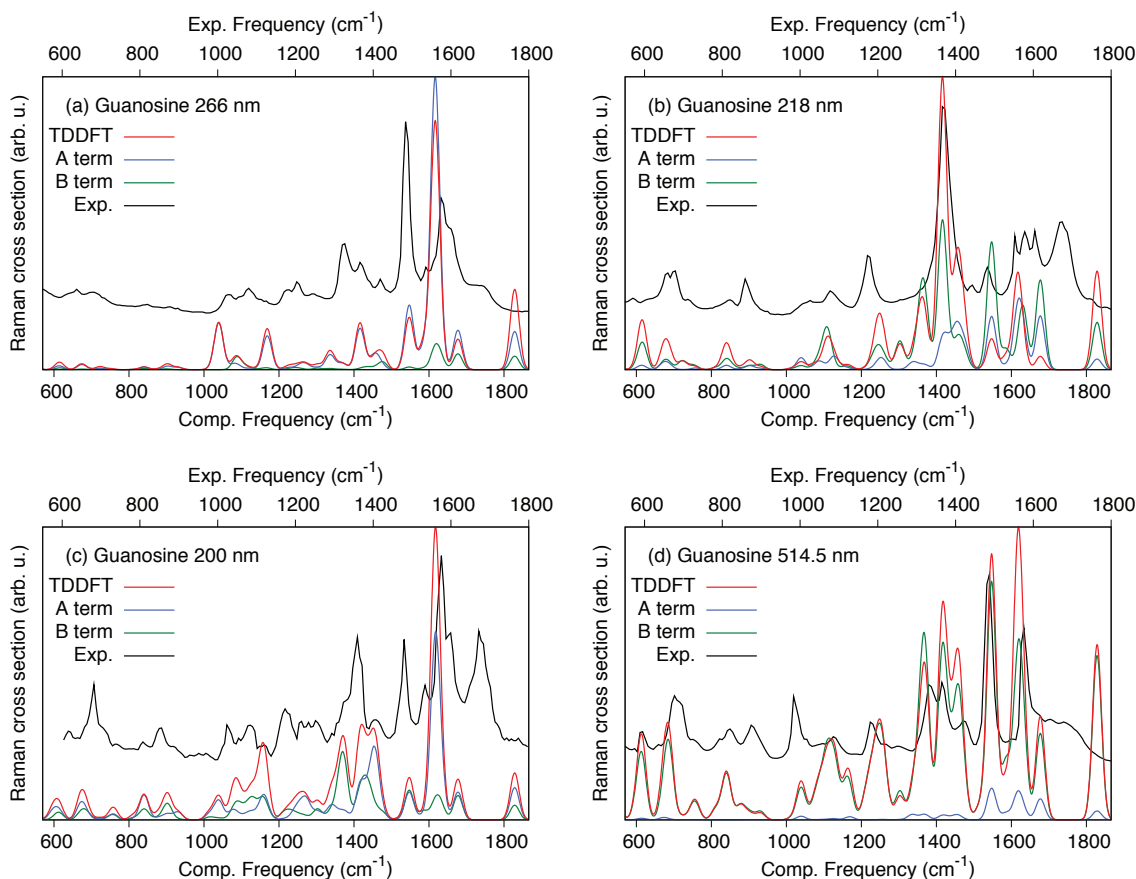
Figure 6.1: Experimental and computed Raman spectra of guanosine at 266, 218, 200, and 514.5 nm excitations. Experimental spectra of guanosine-5′-monophosphate (GMP) are from Refs. 222 and 223. Note that different frequency scales are applied to experimental and computed Raman spectra. See text for computational details.

functional [220] and is in part due to the lack of solvation effects in the calculations. Since the shape of resonance Raman spectra is sensitive to the relative position of the frequency of the incident light in the electronic excitation spectrum, we correct for the systematic error in excitation energies with PBE0. To this end, we first introduce a linear regression between the computed and experimental excitation energies based on the four strongly allowed electronic transitions of guanosine. The slope of the linear regression is 1.02, the offset is 0.35 eV. In addition, frequency scales in experimental and computed Raman spectra are adjusted in Fig. 6.1(a)–(d) to reflect the systematic overestimation of vibrational frequencies with PBE0 functional [219]. This corresponds to an effective scaling factor of 0.96.

The experimental resonance Raman spectrum at 266 nm excitation (Fig. 6.1(a)) is characterized by a strong 1492 cm^{-1} Raman peak and a slightly less intense 1581 cm^{-1} band. The former vibrational band was attributed to an imidazole ring vibration while the latter was assigned to a pyrimidine ring stretch mode [227]. A complete assignment of intensive Raman bands of guanosine is given in the supplementary information. To facilitate comparison between experimental and theoretical results, we compute the resonance Raman spectra at an excitation frequency shifted according to the linear regression results, see above. The experimental results obtained using 266 nm (4.66 eV) excitation are thus compared to computed Raman spectra at the 245 nm (5.07 eV) excitation. The computed Raman spectrum at 245 nm is dominated by contributions from the S_1 excited state. The strongest vibrational band is found at 1631 cm^{-1} and stems from the $\nu(\mathrm{N_7-C_8})$ bond stretch. The pyrimidine ring stretch is observed as a weaker band at 1547 cm^{-1}. Comparison with the resonance Raman

spectrum computed for the S_2 electronic excitation shows the opposite pattern, with a strong band at 1547 cm^{-1} and a somewhat less intense one at 1631 cm^{-1}. The predicted spectrum at resonance with the S_2 state seems to be in a better overall agreement with the experimental resonance Raman spectrum at 266 nm than the computed spectrum at resonance with the S_1 state, see supplementary information for more details. This findings underscore the importance of an accurate determination of the relative position of the frequency of the incident radiation relative to the electronic excitation spectrum of the molecule. The linear regression between experimental and computed excitations used here is perhaps the simplest possible correction scheme, while more rigorous approaches would contributions from the A terms, as is expected for an excitation close to resonance.

The experimental resonance Raman spectrum for the 218 nm excitation is characterized by a strong vibrational band at 1367 cm^{-1} assigned to an in-plane purine ring vibration. The $\nu(C_6{=}O)$ Raman band is observed at 1685 cm^{-1}. The corresponding computed spectrum is obtained for the 203 nm (6.11 eV) excitation. The intermediate $\pi \rightarrow \pi^*$ excited state S_{10} of guanosine of low intensity (computed excitation energy 6.25 eV) has the largest contribution to the computed resonance Raman spectrum. It might be associated with the electronic transition observed at 215 nm (5.77 eV) in circular dichroism (CD) spectra of guanosine [228]. Due to the low oscillator strength of the S_{10} transition (0.05), the resonance Raman intensity is derived from both the A and the B terms. The strongest vibrational band in the computed resonance Raman spectrum at 203 nm excitation purine ring stretch mode predicted at 1416 cm^{-1}.

The experimental resonance Raman spectrum at 200 nm shows a strong pyrimidine

ring stretching band at 1578 cm^{-1} vibrational band as well as three Raman peaks of nearly equal intensity at 1679 cm^{-1}, 1489 cm^{-1}, and 1364 cm^{-1}, which are assigned to the ν(C$_6$=O) stretch, a pyrimidine ring stretch, and an imidazole ring stretch, respectively. The low-frequency part of the resonance Raman spectrum is dominated by the ring breathing mode. The computed resonance Raman spectrum at 187 nm (6.63 eV) is close in energy to the strongly allowed $\pi \to \pi^*$ state (S_{13}) at 6.79 eV. The pyrimidine ring stretch vibration at 1631 cm^{-1} is predicted as the strongest vibrational band. The intensities of the the ν(C$_6$=O) vibration at 1829 cm^{-1}, the imidazole ring vibration at 1547 cm^{-1}, and the ring deformation mode at 1416 cm^{-1}, which correspond to the three intense Raman bands observed experimentally, are underestimated relative to the strongest Raman peak. Since the excitation at 200 nm is close to strict resonance, the A terms are dominant in the resonance Raman spectrum.

The non-resonant Raman spectrum of guanosine at 514.5 nm is shown in Fig. 6.1(d). Assignments of the non-resonant Raman spectra of guanine and its derivatives have been published previously [229–231]. As expected for Raman spectra far from resonance, the B terms are dominant, while the A terms are comparatively small. The non-resonant case is characterized by a significant number of excited electronic states, each contributing only a small amount to Raman cross sections. Under these circumstances, the closure of the sum over states is applicable, and the resulting Raman cross sections are represented as a ground state response property [191, 195]. The sum-over-states results for guanosine Raman spectra at 514.5 nm including 20 excited electronic states is in very good agreement with the conventional result obtained from

derivatives of frequency-dependent electronic polarizabilities, see supplementary information.

The changes observed in the experimental resonance Raman spectra can be well described within the sum-over-states formalism. A comprehensive assignment of Raman peaks can be achieved. The relative changes in resonance Raman spectra depend on a the relative position of the frequency of the incident radiation within the electronic excitation spectrum. Thus a balanced description of a large number of electronic excitations is required, which represents a considerable challenge for the existing DFT methodology. Generally, the sum-over-states approach reproduces the characteristic changes in the overall shape of resonance Raman spectra reasonably well. This suggests that the main source of error in these calculations is due to electronic excitation energies, while the local properties of excited states, such as energy gradients and derivatives of transition dipole moments, are better reproduced. Similar results have been found for relaxed structures of excited states [206, 212, 213]. However, we note that all comparisons include relative Raman cross sections only. Accurate determination of absolute Raman cross sections is a challenging taks both for experiments and computation and is not considered here.

Raman excitation profiles (REPs) describe the dependence of Raman scattering cross sections on excitation frequency. In Fig. 6.2 we show the REPs for the ring breathing modes of adenosine, guanosine, cytidine, and uridine. These low-frequency totally symmetric vibrational modes correspond to an in-phase expansion or contraction of the entire heteroaromatic ring system. Experimental spectra are from Ref. 232. For consistency, the correction for systematic errors in excitation energies derived for
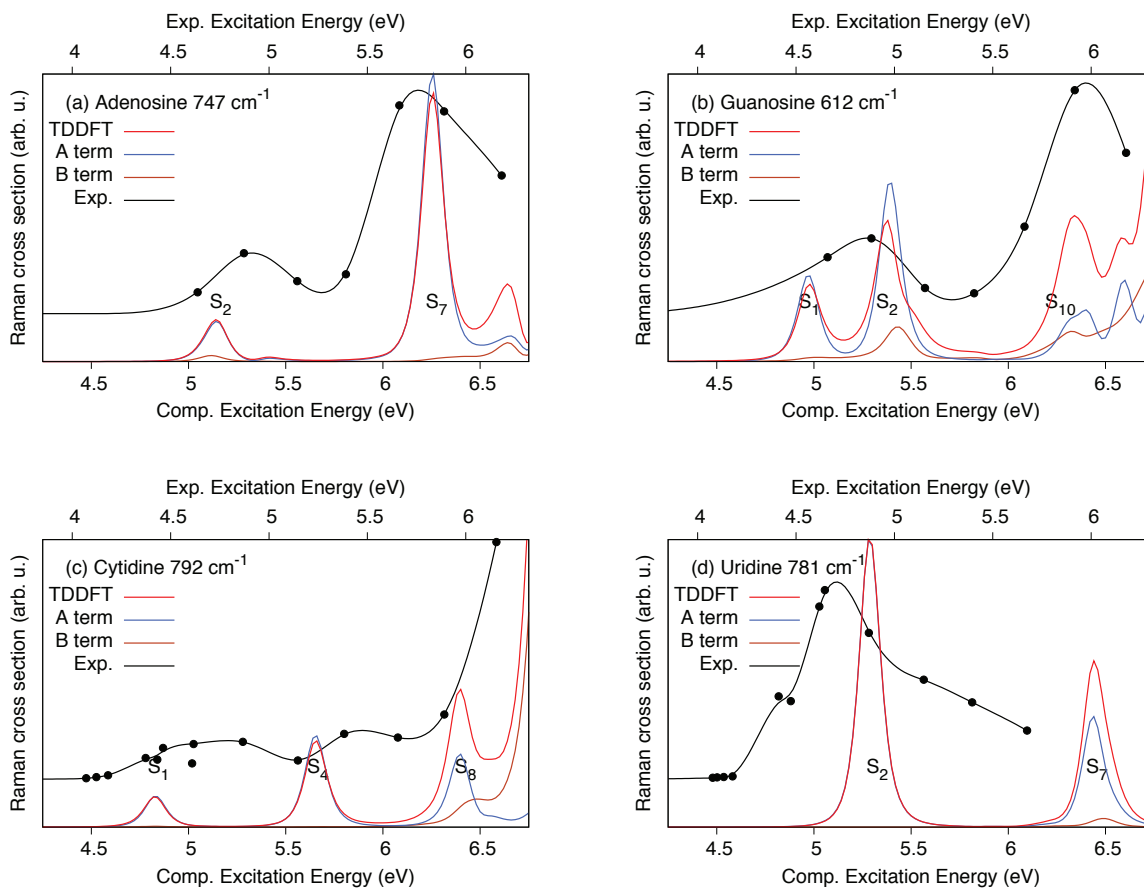
Figure 6.2: Experimental and computed Raman excitation profiles of ring breathing modes of nucleosides. Experimental data for nucleoside 5′-monophosphates are from Ref. 232. Solid lines in experimental data are obtained by interpolation and serve solely to guide the eye. Note that different energy scales are applied to experimental and computed Raman excitation profiles. See text for computational details.

guanosine (see above for details) is used for all nucleosides.

The ring breathing mode of adenosine (Fig. 6.2(a)) is observed at 729 cm^{-1} in experimental spectra, while the computed vibrational frequency is 747 cm^{-1}. The experimental REP shows two maxima at the positions of the electronic absorption bands of adenosine. They are assigned to the strongly allowed $\pi \rightarrow \pi^*$ excited states S_2 and S_7, respectively. The Raman cross section of the ring breathing mode is larger at resonance with the higher-energy absorption band, in line with experimental data. Since the ring breathing vibration is totally symmetric, its intensity is almost entirely due to A term contributions.

The ring breathing mode of guanosine (Fig. 6.2(b)) is observed at 670 cm^{-1}; the computed vibrational frequency is 612 cm^{-1}. Two broad maxima are observed in the experimental REP at the positions of the two electronic absorption bands. The first REP maximum at 4.5–5.0 eV covers the two closely lying dipole-allowed states S_1 and S_2, while the second REP maximum peaked at ca. 6 eV includes the weakly allowed S_{10} state as well as the strongly absorbing S_{13} and S_{17} states. The larger Raman cross section at the second maximum is reproduced by theoretical results. The significant contribution from B terms, which grows with increasing excitation energy, suggests that the ring breathing modes is strongly coupled to non-totally symmetric vibrations.

Experimental and computed REPs of the ring breathing mode of cytidine are shown in Fig. 6.2(c). Experimental vibrational frequency is 782 cm^{-1}, the computed frequency is 792 cm^{-1}. Two moderately strong maxima are present in the experimental REP, followed by a significant increase at the high-energy edge of the REP. The two maxima are attributed to the two $\pi \rightarrow \pi^*$ transitions of cytidine (S_1 and

S_4). The increase at above 6.2 eV is due to the S_8 and higher-lying excited states. While the Raman cross sections are almost exclusively due to A terms at the first maxima, the contribution of B terms increases at higher excitation energies. The ring breathing mode of uridine shows a single broad peak at about 4.7 eV (Fig. 6.2(d)), which is assigned to the strongly allowed S_2 excited state. Experimental vibrational frequency of the ring breathing mode is 783 cm^{-1}, computed value is 781 cm^{-1}.

The two limiting cases of the sum-over-states expression are the strictly resonant situation, in which one resonant electronic state dominates the sum, with the A terms outweighing the corresponding B terms. In this case, the sum reduces to the short-time approximation [233]. The other limiting case, far from resonance, is usually well described by the polarizability theory of Placzek [195], in which polarizability derivatives are often even approximated by their static limits. As was pointed out by Albrecht, B terms are dominant in the non-resonant case [190], while A terms are all but negligible. The polarizability approximation is usually adequate for the range of excitation frequencies below the lowest electronic excitation. In the intermediate regime, e. g., above the first electronic excitation, both A and B terms from different electronic excited states contribute to Raman cross section, and a smooth interpolation, such as the one offered by the present approach, becomes necessary.

The presented sum-over-states approach ignores the details of vibronic structure and includes the contributions from a given electronic excited state in an aggregate manner only. Thus, it is likely to be problematic for molecules with well-resolved vibronic transitions such as small gas-phase species. However, vibronic structure is typically "washed out" in most medium-size and large molecules or in the presence

of a solvent so that the averaged description appears appropriate in these cases. The contributions of different electronic excited states to the Raman scattering tensor $\boldsymbol{\sigma}_Q(\omega)$ are additive, cf. Eq. 6.2. Therefore, the quality of the description of the strictly resonant case may be improved upon by treating the contribution of the resonant electronic state in a more accurate way such as explicit time propagation [200, 201] or summation over vibronic states [199].

The computed resonance Raman cross sections include excitation energies, transition moments and their geometric derivatives. As a consequence, they offer a sensitive test of the TDDFT methodology. Our results indicate that largest source of error for relative resonance Raman cross sections are excitation energies, and the results are found to improve if the excitation energies are corrected for errors intrinsic to the method. Corrections using experimental excitation energies might be used for this purpose if available. Alternatively, corrections for excitation energies might be obtained from more accurate theoretical methods such as coupled-cluster response approaches.

6.4   Conclusion

In this work, we presented a simple approximation to resonance Raman cross section based on the sum-over-states expression for frequency-dependent electronic polarizabilities. Each electronic excited state contributes two types of terms to the Raman cross section, which we term A and B terms, in analogy to Albrecht's treatment. The A terms are dominant in the strictly resonant case, while the B terms determine the Raman cross sections in the non-resonant limit. By using both terms,

the present method can treat the resonant and non-resonant cases on equal footing. Resonance Raman spectra and Raman excitation profiles of nucleosides can be predicted with reasonable accuracy using the sum-over-states approach. The major source of error seem to be electronic excitation energies, which are can be off by up to 0.5 eV with TDDFT. Improved description of resonance Raman spectra and Raman excitation profiles is expected from a combination of the present sum-over-states formulation with more accurate approaches for the few strictly resonant electronic states as well as an first-principles framework for computing electronic state linewidths from the open-system formulation of TDDFT [209].

Chapter 7

Summary and Future Directions

In this dissertation, quantum effects in biological systems were investigated by simulations at the molecular level. To study the effect of the protein environment on long-lived quantum coherences observed during the energy transfer process in the FMO complex, the protein complex embedding the chromophores were simulated in atomistic detail using molecular dynamics and TD-DFT. SC-IVR and DFT calculations were combined to give an accurate quantum dynamics. A formula for the resonance Raman spectra was developed using TD-DFT and analytic gradients and applied to the nucleic acid bases.

Our exciton propagation method with molecular dynamics and TD-DFT is a phenomological model like the Haken-Strobl-Reineker method. The effect of the bath is included as classical stochastic terms in the system Hamiltonian, and the reduced density matrix is evaluated by averaging over the realization of quantum trajectories. Although very convenient in carrying out the propagation using stochastic simulation, this type of stochastic Liouville eqaution cannot reproduce the correct asymptotic

behavior at a finite temperature. Several propagation methods based on trajectories generated by stochastic generators [59, 99, 234–237] or real time path integral Monte Carlo [238–241] are known to produce exact dynamics. We expect that these stochastic methods are more appropriate than master equation based approaches for atomistic simulations. However, most of these stochastic approaches are obtained by mathematical unraveling of the master equation or influence functional rather than contemplating the physical system. Therefore, further investigations are needed to combine these methods with atomistic simulations.

Simulation of the protein environment is currently limited to classical mechanics due to the large degrees of freedom. As explored in Chapter 5, very accurate quantum dynamics can be obtained on top of classical mechanics using SC-IVR. Another possibility is to use mixed quantum-classical dynamics [242–245]. This formalism was developed to treat the dynamics of a quantum subsystem interacting with a classical bath by propagating the classical bath and the quantum reduced density matrix in phase space using the Wigner representation. However, both of these methods are not scalable enough to directly simulate the entire photosynthetic system. Other promising approaches would be to introduce the quantum correction factors to the classical bath correlation. These factors have been studied in the context of vibrational energy relaxation [69, 70, 246] and are expected to be straightforwardly applicable to the energy transfer dynamics.

Bibliography

[1] P. A. M. Dirac, *P. R. Soc. Lond. A-Conta.* **123**, pp. 714 (1929).

[2] J. A. McCammon, B. R. Gelin, and M. Karplus, *Nature* **267**, 585 (1977).

[3] M. Karplus and J. A. McCammon, *Nat. Struct. Biol.* **9**, 646 (2002).

[4] W. Wang, O. Donini, C. M. Reyes, and P. A. Kollman, *Annu. Rev. Bioph. Biom.* **30**, 211 (2001).

[5] T. Hansson, C. Oostenbrink, and W. van Gunsteren, *Curr. Opin. Struc. Biol.* **12**, 190 (2002).

[6] M. Karplus and J. Kuriyan, *Proc. Natl Acad. Sci. USA* **102**, 6679 (2005).

[7] E. Villa, A. Balaeff, L. Mahadevan, and K. Schulten, *Multiscale Model. Sim.* **2**, 527 (2004).

[8] R. Phillips, M. Dittrich, and K. Schulten, *Ann. Rev. Mater. Res.* **32**, 219 (2002).

[9] G. Ayton, S. G. Bardenhagen, P. McMurtry, D. Sulsky, and G. A. Voth, *J. Chem. Phys.* **114**, 6913 (2001).

[10] B. Matthews, R. Fenna, M. Bolognesi, M. Schmid, and J. Olson, *J. Mol. Biol.* **131**, 259 (1979).

[11] Y.-F. Li, W. Zhou, R. E. Blankenship, and J. P. Allen, *J. Mol. Biol.* **271**, 456 (1997).

[12] J. Olson, *Photosynth. Res.* **80**, 181 (2004).

[13] S. I. E. Vulto et al., *J. Phys. Chem. B* **102**, 10630 (1998).

[14] J. Adolphs and T. Renger, *Biophys. J.* **91**, 2778 (2006).

[15] A. Freiberg, S. Lin, K. Timpmann, and R. E. Blankenship, *J. Phys. Chem. B* **101**, 7211 (1997).

[16] S. Savikhin, D. R. Buck, and W. S. Struve, *J. Phys. Chem. B* **102**, 5556 (1998).

[17] M. Wendling et al., *J. Phys. Chem. B* **104**, 5825 (2000).

[18] D. Tronrud, J. Wen, L. Gay, and R. Blankenship, *Photosynth. Res.* **100**, 79 (2009).

[19] T. Föster, *Ann. Phys.* **437**, 55 (1948).

[20] M. Wendling et al., *Photosynth. Res.* **71**, 99 (2002).

[21] M. Cho, H. M. Vaswani, T. Brixner, J. Stenger, and G. R. Fleming, *J. Phys. Chem. B* **109**, 10542 (2005).

[22] F. Müh et al., *Proc. Natl Acad. Sci. USA* **104**, 16862 (2007).

[23] G. S. Engel et al., *Nature* **446**, 782 (2007).

[24] H. Lee, Y.-C. Cheng, and G. R. Fleming, *Science* **316**, 1462 (2007).

[25] G. Panitchayangkoon et al., *Proc. Natl Acad. Sci. USA* **107**, 12766 (2010).

[26] P. Rebentrost, M. Mohseni, and A. Aspuru-Guzik, *J. Phys. Chem. B* **113**, 9942 (2009).

[27] P. Rebentrost, M. Mohseni, I. Kassal, S. Lloyd, and A. Aspuru-Guzik, *New J. Phys.* **11**, 033003 (2009).

[28] A. Ishizaki and G. R. Fleming, *J. Chem. Phys.* **130**, 234110 (2009).

[29] A. Ishizaki and G. R. Fleming, *Proc. Natl Acad. Sci. USA* **106**, 17255 (2009).

[30] G. Tao and W. H. Miller, *J. Phys. Chem. Lett.* **1**, 891 (2010).

[31] P. Nalbach, A. Ishizaki, G. R. Fleming, and M. Thorwart, *New J. Phys.* **13**, 063040 (2011).

[32] S. Shim, P. Rebentrost, S. Valleau, and A. Aspuru-Guzik, *Biophys. J.* **102**, 649 (2012).

[33] T. C. Berkelbach, T. E. Markland, and D. R. Reichman, *J. Chem. Phys.* **136**, 084104 (2012).

[34] H.-P. Breuer and F. Petruccione, *The Theory of Open Quantum Systems*, Oxford University Press, New York, 2002.

[35] A. Croy and U. Saalmann, *Phys. Rev. B* **80**, 073102 (2009).

[36] J. Xu, R.-X. Xu, M. Luo, and Y. Yan, *Chem. Phys.* **370**, 109 (2010).

[37] J. Hu, R.-X. Xu, and Y. Yan, *J. Chem. Phys.* **133**, 101106 (2010).

[38] R. Kubo, *J. Phys. Soc. Jpn* **17**, 1100 (1962).

[39] H. Haken and G. Strobl, *Z. Phys.* **262**, 135 (1973).

[40] H. Haken and P. Reineker, *Z. Phys.* **249**, 253 (1972).

[41] P. Reineker and R. Kuhne, *Z. Phys. B Con. Mat.* **22**, 193 (1975).

[42] M. A. Palenberg, R. J. Silbey, C. Warns, and P. Reineker, *J. Chem. Phys.* **114**, 4386 (2001).

[43] X. Chen and R. J. Silbey, *J. Chem. Phys.* **132**, 204503 (2010).

[44] C. Aslangul and P. Kottis, *Phys. Rev. B* **10**, 4364 (1974).

[45] R. E. Blankenship, *Molecular Mechanisms of Photosynthesis*, Wiley-Blackwell, 1st edition, 2002.

[46] Y.-C. Cheng and G. R. Fleming, *Ann. Rev. Phys. Chem.* **60**, 241 (2009).

[47] E. Collini et al., *Nature* **463**, 644 (2010).

[48] M. B. Plenio and S. F. Huelga, *New J. Phys.* **10**, 113019 (2008).

[49] M. Mohseni, P. Rebentrost, S. Lloyd, and A. Aspuru-Guzik, *J. Chem. Phys.* **129**, 174106 (2008).

[50] S. Jang, Y.-C. Cheng, D. R. Reichman, and J. D. Eaves, *J. Chem. Phys.* **129**, 101104 (2008).

[51] J. Wu, F. Liu, Y. Shen, J. Cao, and R. J. Silbey, *New J. Phys.* **12**, 105012 (2010).

[52] M. Sarovar, A. Ishizaki, G. R. Fleming, and K. B. Whaley, *Nat. Phys.* **6**, 462 (2010).

[53] F. Caruso, A. W. Chin, A. Datta, S. F. Huelga, and M. B. Plenio, *Phys. Rev. A* **81**, 062346 (2010).

[54] F. Fassioli and A. Olaya-Castro, *New J. Phys.* **12**, 085006 (2010).

[55] J. Cai, G. G. Guerreschi, and H. J. Briegel, *Phys. Rev. Lett.* **104**, 1 (2010).

[56] A. Olaya-Castro, C. Lee, F. Olsen, and N. Johnson, *Phys. Rev. B* **78**, 7 (2008).

[57] Q. Shi, L. Chen, G. Nan, R.-X. Xu, and Y. Yan, *J. Chem. Phys.* **130**, 084105 (2009).

[58] J. Zhu, S. Kais, P. Rebentrost, and A. Aspuru-Guzik, *J. Phys. Chem. B* **115**, 1531 (2011).

[59] J. Piilo, S. Maniscalco, K. Härkönen, and K.-A. Suominen, *Phys. Rev. Lett.* **100**, 180402 (2008).

[60] P. Rebentrost, M. Mohseni, and A. Aspuru-Guzik, *J. Phys. Chem. B* **113**, 9942 (2009).

[61] M. Tamoi et al., *J. Biol. Chem.* **285**, 15399 (2010).

[62] P. Jahns, M. Graf, Y. Munekage, and T. Shikanai, *FEBS lett.* **519**, 99 (2002).

[63] P. Pesaresi, D. Sandon, E. Giuffra, and R. Bassi, *FEBS Lett.* **402**, 151 (1997).

[64] W. D. Cornell et al., *J. Am. Chem. Soc.* **117**, 5179 (1995).

[65] M. Ceccarelli, P. Procacci, and M. Marchi, *J. Comp. Chem.* **24**, 129 (2003).

[66] Y. Shao et al., *Phys. Chem. Chem. Phys.* **8**, 3172 (2006).

[67] V. May and O. Kühn, *Charge and Energy Transfer Dynamics in Molecular Systems*, Wiley-VCH Verlag, Weinheim, 2004.

[68] S. A. Egorov, K. F. Everitt, and J. L. Skinner, *J. Phys. Chem. A* **103**, 9494 (1999).

[69] J. L. Skinner and K. Park, *J. Phys. Chem. B* **105**, 6716 (2001).

[70] G. Stock, *Phys. Rev. Lett.* **102**, 118301 (2009).

[71] J. C. Tully, *J. Chem. Phys.* **93**, 1061 (1990).

[72] M. Ben-Nun, J. Quenneville, and T. J. Martínez, *J. Phys. Chem. A* **104**, 5161 (2000).

[73] Y. Wu and M. F. Herman, *J. Chem. Phys.* **123**, 144106 (2005).

[74] Y. C. Cheng and G. R. Fleming, *J. Phys. Chem. A* **112**, 4254 (2008).

[75] S. Mukamel, *Principles of Nonlinear Optical Spectroscopy*, Oxford University Press, 1995.

[76] I. L. Chuang and M. A. Nielsen, *J. Mod. Opt.* **44**, 2455 (1997).

[77] J. F. Poyatos, J. I. Cirac, and P. Zoller, *Phys. Rev. Lett.* **78**, 390 (1997).

[78] J. Yuen-Zhou, M. Mohseni, and A. Aspuru-Guzik, arXiv:1006.4866v3 (2010).

[79] J. Yuen-Zhou and A. Aspuru-Guzik, arXiv:1101.2716v1 (2011).

[80] E. C. G. Sudarshan, P. M. Mathews, and J. Rau, *Phys. Rev.* **121**, 920 (1961).

[81] M. Cho, *Two Dimensional Optical Spectroscopy*, CRC Press, 2009.

[82] M. Goldman, *Quantum Description of High-Resolution NMR in Liquids*, Oxford University Press, 1991.

[83] N. S. Ginsberg, Y.-C. Cheng, and G. R. Fleming, *Acc. Chem. Res.* **42**, 1352 (2009).

[84] D. M. Jonas, *Ann. Rev. Phys. Chem.* **54**, 425 (2003).

[85] M. Cho, *Chem. Rev.* **108**, 1331 (2008).

[86] B. Palmieri, D. Abramavicius, and S. Mukamel, *J. Chem. Phys.* **130**, 204512 (2009).

[87] A. Ishizaki and G. R. Fleming, *J. Chem. Phys.* **130**, 234111 (2009).

[88] J. Strumpfer and K. Schulten, *J. Chem. Phys.* **131**, 225101 (2009).

[89] A. M. Virshup et al., *J. Phys. Chem. B* **113**, 3280 (2009).

[90] F. Caruso, A. W. Chin, A. Datta, S. F. Huelga, and M. B. Plenio, *J. Chem. Phys.* **131**, 105106 (2009).

[91] A. G. Dijkstra and Y. Tanimura, *New J. Phys.* **12**, 055005 (2010).

[92] P. Rebentrost and A. Aspuru-Guzik, *J. Chem. Phys.* **134**, 101103 (2011).

[93] M. Schmidt am Busch, F. Muh, M. El-Amine Madjet, and T. Renger, *J. Phys. Chem. Lett.* **2**, 93 (2011).

[94] J. Gilmore and R. H. McKenzie, *J. Phys. Chem. A* **112**, 2162 (2008).

[95] G. Ritschel, J. Roden, W. T. Strunz, A. Aspuru-Guzik, and A. Eisfeld, *J. Phys. Chem. Lett.* **2**, 2912 (2011).

[96] J. Moix, J. Wu, P. Huo, D. Coker, and J. Cao, arXiv:1109.3416v1 (2011).

[97] B. P. Krueger, G. D. Scholes, and G. R. Fleming, *J. Phys. Chem. B* **102**, 5378 (1998).

[98] C.-P. Hsu, Z.-Q. You, and H.-C. Chen, *J. Phys. Chem. C* **112**, 1204 (2008).

[99] J. Dalibard, Y. Castin, and K. Mølmer, *Phys. Rev. Lett.* **68**, 580 (1992).

[100] Z. Vokcov and J. V. Burda, *J. Phys. Chem. A* **111**, 5864 (2007).

[101] A. J. Leggett et al., *Rev. Mod. Phys.* **59**, 1 (1987).

[102] R. M. Peralstein, *Theoretical Interpretation of Antenna Spectra*, CRC Press, New York, 1991.

[103] A. Damjanović, I. Kosztin, U. Kleinekathöfer, and K. Schulten, *Phys. Rev. E* **65**, 031919 (2002).

[104] C. Olbrich and U. Kleinekathofer, *J. Phys. Chem. B* **114**, 12427 (2010).

[105] P. Huo and D. F. Coker, *J. Chem. Phys.* **133**, 184108 (2010).

[106] D. B. Percival and A. T. Walden, *Spectral Analysis for Physical Application*, Cambridge University Press, 1993.

[107] A. Nazir, *Phys. Rev. Lett.* **103**, 146404 (2009).

[108] D. Abramavicius and S. Mukamel, *J. Chem. Phys.* **134**, 174504 (2011).

[109] C. Olbrich, J. Strumpfer, K. Schulten, and U. Kleinekathofer, *J. Phys. Chem. B* **115**, 758 (2011).

[110] C. Olbrich et al., *J. Phys. Chem. B* **115**, 8609 (2011).

[111] G. S. Schlau-Cohen et al., *Nat. Chem.* **advance online publication.** (2012).

[112] C. Y. Wong et al., *Nat. Chem.* **advance online publication.** (2012).

[113] A. Kolli, E. J. O'Reilly, G. D. Scholes, and A. Olaya-Castro, arXiv:1203.5056v1 (2012).

[114] A. G. Redfield, *IBM J. Res. Dev.* **1**, 19 (1957).

[115] A. Ishizaki and Y. Tanimura, *J. Phys. Soc. Jpn* **74**, 3131 (2005).

[116] M. Topaler and N. Makri, *J. Chem. Phys.* **97**, 9001 (1992).

[117] N. Makri, *Chem. Phys. Lett.* **193**, 435 (1992).

[118] R. Feynman and F. Vernon, *Ann. Phys.* **24**, 118 (1963).

[119] C. Olbrich, J. Strümpfer, K. Schulten, and U. Kleinekathöfer, *J. Phys. Chem. B* **115**, 758 (2011).

[120] D. Thirumalai, E. J. Bruskin, and B. J. Berne, *J. Chem. Phys.* **79**, 5063 (1983).

[121] K. Allinger, B. Carmeli, and D. Chandler, *J. Chem. Phys.* **84**, 1724 (1986).

[122] E. C. Behrman, G. a. Jongeward, and P. G. Wolynes, *J. Chem. Phys.* **83**, 668 (1985).

[123] J. Cao and B. J. Berne, *J. Chem. Phys.* **99**, 2902 (1993).

[124] J. M. Moix, Y. Zhao, and J. Cao, *Phys. Rev. B* **85**, 115412 (2012).

[125] C. P. Robert and G. Casella, *Monte Carlo statistical methods.*, Springer Verlag, New York, 2004.

[126] N. S. Pillai, A. M. Stuart, and A. H. Thiery, arXiv:1103.0542v2 (2011).

[127] A. Aspuru-Guzik and W. A. Lester Jr., Quantum monte carlo methods for the solution of the schrdinger equation for molecular systems, in *Special Volume, Computational Chemistry*, edited by C. L. Bris, volume 10 of *Handbook of Numerical Analysis*, pages 485 – 535, Elsevier, 2003.

[128] M. H. Alexander, *Chem. Phys. Lett.* **347**, 436 (2001).

[129] J. M. Flegal and G. L. Jones, *Ann. Stat.* **38**, 1034 (2010).

[130] G. M. Ljung and G. E. P. Box, *Biometrika* **65**, 297 (1978).

[131] C. D. Schwieters and G. a. Voth, *J. Chem. Phys.* **111**, 2869 (1999).

[132] J. R. Schmidt and J. C. Tully, *J. Chem. Phys.* **127**, 094103 (2007).

[133] J. M. Herbert and M. Head-Gordon, *Phys. Chem. Chem. Phys.* **7**, 3269 (2005).

[134] R. Car and M. Parrinello, *Phys. Rev. Lett.* **55**, 2471 (1985).

[135] H. B. Schlegel, J. M. Millam, S. S. Iyengar, G. A. Voth, A. D. Daniels, G. E. Scuseria, and M. J. Frisch, *J. Chem. Phys.* **114**, 9758 (2001).

[136] J. M. Herbert and M. Head-Gordon, *J. Chem. Phys.* **121**, 11542 (2004).

[137] Y. Liu, D. Yarne, M. E. Tuckerman, *Phys. Rev. B* **68**, 125110 (2003).

[138] P. Tangney, *J. Chem. Phys.* **124**, 044111 (2006)

[139] M. Pavese, D. R. Berard, and G. A. Voth, *Chem. Phys. Lett.* **300**, 93 (1999)

[140] G. A. Worth, M. A. Robb, and I. Burghardt, *Faraday Discuss.* **127**, 307 (2004).

[141] S. Iyengar and J. Jakowski, *J. Chem. Phys.* **122**, 114105 (2005).

[142] O. Knospe and P. Jungwirth, *Chem. Phys. Lett.* **317**, 529 (2000).

[143] W. H. Miller, *Adv. Chem. Phys.* **25**, 69 (1974); W. H. Miller, *Faraday Discuss.* **110**, 1 (1998)

[144] W. H. Miller, *J. Chem. Phys.* **53**, 3578 (1970); *ibid.* **53**, 1949 (1970); W. H. Miller, *J. Phys. Chem. A* **105**, 2942 (2001); M. Thoss and H. Wang, *Annu. Rev. Phys. Chem.* **55**, 299 (2004); K. G. Kay, *Annu. Rev. Phys. Chem.* **56**, 255 (2005).

[145] H. Wang, X. Sun, and W. H. Miller, *J. Chem. Phys.* **108**, 9726 (1998); X. Sun and W. H. Miller, *J. Chem. Phys.* **110**, 6635 (1999); M. Thoss, H. Wang, and W. H. Miller, *J. Chem. Phys.* **114**, 9220 (2001); T. Yamamoto, H. Wang, and

W. H. Miller, *J. Chem. Phys.* **116**, 7335 (2002); T. Yamamoto W. H. Miller, *J. Chem. Phys.* **118**, 2135 (2003).

[146] J. Ankerhold, M. Saltzer, and E. Pollak, *J. Chem. Phys.* **116**, 5925 (2002); S. Zhang and E. Pollak, *Phys. Rev. Lett.* **91**, 190201 (2003); S. S. Zhang and E. Pollak, *J. Chem. Phys.* **121**, 3384 (2004).

[147] A. R. Walton, D. E. Manolopoulos, *Mol. Phys.* **87**, 961 (1996); A. R. Walton and D. E. Manolopoulos, *Chem. Phys. Lett.* **244**, 448 (1995); M. L. Brewer, J. S. Hulme, and D. E. Manolopoulos, *J. Chem. Phys.* **106**, 4832 (1997).

[148] S. Bonella, D. Montemayor, and D. F. Coker, *Proc. Natl. Am. Soc.* **102**, 6715 (2005); S. Bonella and D. F. Coker, *J. Chem. Phys.* **118**, 4370 (2003).

[149] Y. Wu , M. Herman, V. S. Batista, *J. Chem. Phys.* **122**, 114114 (2005); Y. Wu and V. S. Batista, *J. Chem. Phys.* **118**, 6720 (2003).

[150] F. Grossmann, *Comment. At. Mol. Phys.* **34**, 243 (1999).

[151] E. J. Heller, *J. Chem. Phys.* **62**, 1544 (1975); E. J. Heller, *J. Chem. Phys.* **75**, 2923 (1981).

[152] E. J. Heller, *Acc. Chem. Res.* **14**, 368 (1981); E. J. Heller, *Acc. Chem. Res.* **39**, 127 (2006).

[153] T. Van Voorhis and E. J. Heller, *J. Chem. Phys.* **119**, 12153 (2003).

[154] D. V. Shalashilin and M. S. Child, *Chem. Phys.* **304**, 103 (2004); D. V. Shalashilin and M. S. Child, *J. Chem Phys.* **115**, 5367 (2001).

[155] M. Ben-Nun and T. J. Martinez, *Adv. Chem. Phys.* **121**, 439 (2002).

[156] M. F. Herman and E. Kluk, *Chem. Phys.* **91**, 27 (1984); K. G. Kay, *J. Chem. Phys.* **100**, 4377 (1994); K. G. Kay, *J. Chem. Phys.* **100**, 4432 (1994).

[157] H. Wang, D. E. Manolopoulos, and W. H. Miller, *J. Chem. Phys.* **115**, 6317 (2001).

[158] A. L. Kaledin and W. H. Miller, *J. Chem. Phys.* **118**, 7174 (2003); M. Ceotto, *PhD Dissertation*, University of California, Berkeley (2005); A. L. Kaledin and W. H. Miller, *J. Chem. Phys.* **119**, 3078 (2003).

[159] Y. Elran and K. G. Kay, *J. Chem. Phys.* **110**, 3653 (1999); *ibid.* **110**, 8912 (1999).

[160] Y. Shao, *et al. Phys. Chem. Chem. Phys.* **8,** 3172 (2006).

[161] A.D. Becke, *J. Chem. Phys.* **98,** 5648 (1993); P. J. Stephens, F. J. Devlin, C. F. Chabalowski, and M. J. Frisch, *J. Phys. Chem.* **98,** 11623 (1994).

[162] T. Dunning Jr. *J. Chem. Phys.* **90**, 1007 (1989).

[163] J. Zuniga, M. Alacid, A. Bastida, F. J. Carvajal, and A. Requena, *J. Mol. Spectr.* **195**, 137 (1999).

[164] K. Levenberg, *Quart. Appl. Math.* **2**, 164 (1944); D. Marquardt, *Siam J. Appl. Math.* **11**, 431 (1965); M. I. A. Lourakis, Levenberg-Marquardt nonlinear least squares algorithms in C/C++, 2004.

Available from `http://www.ics.forth.gr/~lourakis/levmar/`.

[165] M. H. Beck and H.-D. Meyer, *J. Chem. Phys.* **114**, 2036 (2001); G. A. Worth, M. H. Beck, A. Jäckle, and H.-D. Meyer, The MCTDH Package, Version 8.3, University of Heidelberg, Heidelberg, Germany, 2002.

Available from `http://www.pci.uni-heidelberg.de/tc/usr/mctdh/`.

[166] F. Gygi, *Phys. Rev. B* **51**, 11190 (1995).

[167] J. R. Chelikowsky, X. Jing, K. Wu, and Y. Saad, *Phys. Rev. B* **53**, 12071 (1994).

[168] H. P. M. Filho, *Spectr. Acta Part A* **58**, 2621 (2002).

[169] W. J. Hehre, R. Ditchfield, and J. A. Pople, *J. Chem. Phys.* **56**, 2257 (1972).

[170] E. J. Heller, E. B. Stechel, and M. J. Davis, *J. Chem. Phys.* **73**, 4720 (1980).

[171] X. Sun and W. H. Miller, *J. Chem. Phys.*, 1998, **108**, 8870.

[172] A. M. N. Niklasson, C. J. Tymczak, and M. Challacombe, *Phys. Rev. Lett.* **97**, 123001 (2006); A. M. N. Niklasson, C. J. Tymczak, and M. Challacombe, *J. Chem. Phys.* **126**, 144103 (2007).

[173] L. R. Brown and C. B. Farmer, *Appl. Opt.* **26**, 5154 (1987).

[174] J. Tatchen and E. Pollak, *J. Chem. Phys.* **130**, 041103 (2009).

[175] P. P. Shorygin, *Zh. Fiz. Khim.* **21**, 1125 (1947).

[176] P. P. Shorygin and L. L. Krushinskij, *J. Raman Spectrosc.* **28**, 383 (1997).

[177] F. S. Parker, *Applications of Infrared, Raman, and Resonance Raman Spectroscopy in Biochemistry*, Springer, New York, 1983.

[178] T. G. Spiro, editor, *Biological Applications of Raman Spectroscopy*, volume 1–3, Wiley, New York, 1987.

[179] J. M. Benevides, S. A. Overman, and G. J. Thomas, *J. Raman Spectrosc.* **36**, 279 (2005).

[180] M. Moskovits, *Rev. Mod. Phys.* **57**, 783 (1985).

[181] K. Kneipp, M. Moskovits, and H. Kneipp, editors, *Surface-Enhanced Raman Scattering: Physics and Applications*, Springer, Berlin, 2006.

[182] L. Jensen, C. M. Aikens, and G. C. Schatz, *Chem. Soc. Rev.* **37**, 1061 (2008).

[183] G. Schatz, M. Young, and R. Van Duyne, Electromagnetic mechanism of SERS, in *Surface-Enhanced Raman Scattering*, edited by K. Kneipp, M. Moskovits, and H. Kneipp, volume 103, pages 19–45, Springer, Berlin, 2006.

[184] S. K. Saikin, R. Olivares-Amaya, D. Rappoport, M. Stopa, and A. Aspuru-Guzik, *Phys. Chem. Chem. Phys.* **11**, 9401 (2009).

[185] S. K. Saikin, Y. Chu, D. Rappoport, K. B. Crozier, and A. Aspuru-Guzik, *J. Phys. Chem. Lett.* , 2740 (2010).

[186] S. Nie and S. R. Emory, *Science* **275**, 1102 (1997).

[187] K. Kneipp et al., *Phys. Rev. Lett.* **78**, 1667 (1997).

[188] J. A. Dieringer et al., *J. Am. Chem. Soc.* **131**, 849 (2009).

[189] P. Schorygin, L. Kuzina, and L. Ositjanskaja, *Microchim. Acta* **43**, 630 (1955).

[190] A. C. Albrecht, *J. Chem. Phys.* **34**, 1476 (1961).

[191] D. A. Long, *The Raman Effect*, Wiley, Chichester, 2nd edition, 2002.

[192] H. A. Kramers and W. Heisenberg, *Z. Phys.* **31**, 681 (1925).

[193] P. A. M. Dirac, *Proc. Roy. Soc. A* **114**, 710 (1927).

[194] J. H. van Vleck, *Proc. Nat. Acad. Sci.* **15**, 754 (1929).

[195] G. Placzek, Rayleigh-streuung und raman-effekt, in *Handbuch der Radiologie*, edited by E. Marx, volume VI/2, pages 209–374, Akademische Verlagsgesellschaft, Leipzig, 1934.

[196] J. Behringer and J. Brandmüller, *Z. Elektrochem.* **60**, 643 (1956).

[197] A. C. Albrecht, *J. Chem. Phys.* **33**, 156 (1960).

[198] G. Fischer, *Vibronic Coupling: the Interaction between the Electronic and Nuclear Motions*, Academic Press, London, 1984.

[199] K. A. Kane and L. Jensen, *J. Phys. Chem. C* **114**, 5540 (2010).

[200] S.-Y. Lee and E. J. Heller, *J. Chem. Phys.* **71**, 4777 (1979).

[201] D. J. Tannor, *J. Chem. Phys.* **77**, 202 (1982).

[202] J. Neugebauer and B. A. Hess, *J. Chem. Phys.* **120**, 11564 (2004).

[203] F. Neese, T. Petrenko, D. Ganyushin, and G. Olbrich, *Coord. Chem. Rev.* **251**, 288 (2007).

[204] L. Jensen, J. Autschbach, and G. C. Schatz, *J. Chem. Phys.* **122**, 224115 (2005).

[205] L. Jensen, L. L. Zhao, J. Autschbach, and G. C. Schatz, *J. Chem. Phys.* **123**, 174110 (2005).

[206] F. Furche and D. Rappoport, Density functional methods for excited states: Equilibrium structure and electronic spectra, in *Computational Photochemistry*, edited by M. Olivucci, Theoretical and Computational Chemistry, pages 93–128, Elsevier, Amsterdam, 2005.

[207] J. Yuen-Zhou, D. G. Tempel, C. A. Rodríguez-Rosario, and A. Aspuru-Guzik, *Phys. Rev. Lett.* **104**, 043001 (2010).

[208] J. Yuen-Zhou, C. A. Rodríguez-Rosario, and A. Aspuru-Guzik, *Phys. Chem. Chem. Phys.* **11**, 4509 (2009).

[209] D. G. Tempel, M. A. Watson, R. Olivares-Amaya, and A. Aspuru-Guzik, *J. Chem. Phys.* **134**, 074116 (2011).

[210] D. Rappoport and F. Furche, *J. Chem. Phys.* **126**, 201104 (2007).

[211] S. Coriani et al., *J. Chem. Theory Comput.* **6**, 1028 (2010).

[212] F. Furche and R. Ahlrichs, *J. Chem. Phys.* **117**, 7433 (2002).

[213] D. Rappoport and F. Furche, Excited states and photochemistry, in *Time-Dependent Density Functional Theory*, edited by M. A. L. Marques et al., chapter 23, pages 337–354, Springer, Berlin, 2006.

[214] J. P. Perdew, M. Ernzerhof, and K. Burke, *J. Chem. Phys.* **105**, 9982 (1996).

[215] A. Schäfer, C. Huber, and R. Ahlrichs, *J. Chem. Phys.* **100**, 5829 (1994).

[216] C. Adamo, M. Cossi, G. Scalmani, and V. Barone, *Chem. Phys. Lett.* **307**, 265 (1999).

[217] C. Van Caillie and R. D. Amos, *Chem. Phys. Lett.* **328**, 446 (2000).

[218] C. Van Caillie and R. D. Amos, *Phys. Chem. Chem. Phys.* **2**, 2123 (2000).

[219] J. P. Merrick, D. Moran, and L. Radom, *J. Phys. Chem. A* **111**, 11683 (2007).

[220] C. Adamo, G. E. Scuseria, and V. Barone, *J. Chem. Phys.* **111**, 2889 (1999).

[221] TURBOMOLE V6.2 2010, University of Karlsruhe and Forschungszentrum Karlsruhe GmbH, 1989-2007, TURBOMOLE GmbH, 2007-.
Available from `http://www.turbomole.com/`.

[222] S. P. A. Fodor, R. P. Rava, T. R. Hays, and T. G. Spiro, *J. Am. Chem. Soc.* **107**, 1520 (1985).

[223] Y. Nishimura, M. Tsuboi, W. L. Kubasek, K. Bajdor, and W. L. Peticolas, *J. Raman Spectrosc.* **18**, 221 (1987).

[224] L. B. Clark, *J. Am. Chem. Soc.* **116**, 5265 (1994).

[225] M. K. Shukla and J. Leszczynski, *J. Comput. Chem.* **25**, 768 (2004).

[226] M. Shukla and J. Leszczynski, *J. Biomol. Struct. Dyn.* **25**, 93 (2007).

[227] A. Toyama, N. Hanada, J. Ono, E. Yoshimitsu, and H. Takeuchi, *J. Raman Spectros.* **30**, 623 (1999).

[228] W. Voelter, R. Records, E. Bunnenberg, and C. Djerassi, *J. Am. Chem. Soc.* **90**, 6163 (1968).

[229] M. Mathlouthi, A. M. Seuvre, and J. L. Koenig, *Carbohyd. Res.* **146**, 15 (1986).

[230] J. Florián, *J. Phys. Chem.* **97**, 10649 (1993).

[231] B. Giese and D. McNaughton, *Phys. Chem. Chem. Phys.* **4**, 5161 (2002).

[232] M. Tsuboi, Y. Nishimura, and A. Y. Hirakawa, Resonance raman spectroscopy and normal modes of nucleic acid bases, in *Biological Applications of Raman Spectroscopy*, edited by T. G. Spiro, volume 2, pages 109–179, Wiley, New York, 1987.

[233] D. J. Tannor, E. J. Heller, and R. Sundberg, *J. Phys. Chem.* **86**, 1822 (1982).

[234] H.-P. Breuer, B. Kappler, and F. Petruccione, *Phys. Rev. A* **59**, 1633 (1999).

[235] J. T. Stockburger and H. Grabert, *Chem. Phys.* **268**, 249 (2001).

[236] J. Stockburger and H. Grabert, *Phys. Rev. Lett.* **88**, 2 (2002).

[237] J. T. Stockburger, *Chem. Phys.* **296**, 159 (2004).

[238] L. Mühlbacher, J. Ankerhold, and C. Escher, *J. Chem. Phys.* **121**, 12696 (2004).

[239] L. Mühlbacher and J. Ankerhold, *J. Chem. Phys.* **122**, 184715 (2005).

[240] L. Mühlbacher and E. Rabani, *Phys. Rev. Lett.* **100**, 1 (2008).

[241] O. Mülken, L. Mühlbacher, T. Schmid, and A. Blumen, *Phys. Rev. E* **81**, 1 (2010).

[242] R. Kapral and G. Ciccotti, *J. Chem. Phys.* **110**, 8919 (1999).

[243] R. Kapral, *J. Phys. Chem. A* **105**, 2885 (2001).

[244] M. Toutounji and R. Kapral, *Chem. Phys.* **268**, 79 (2001).

[245] M. Toutounji, *J. Chem. Phys.* **123**, 244102 (2005).

[246] J. L. Skinner and D. Hsu, *J. Phys. Chem.* **90**, 4931 (1986).